

Springer Theses

Recognizing Outstanding Ph.D. Research

Rui Wang

Single Piles in Liquefiable Ground

Seismic Response and Numerical
Analysis Methods

 Springer

Springer Theses

Recognizing Outstanding Ph.D. Research

Aims and Scope

The series “Springer Theses” brings together a selection of the very best Ph.D. theses from around the world and across the physical sciences. Nominated and endorsed by two recognized specialists, each published volume has been selected for its scientific excellence and the high impact of its contents for the pertinent field of research. For greater accessibility to non-specialists, the published versions include an extended introduction, as well as a foreword by the student’s supervisor explaining the special relevance of the work for the field. As a whole, the series will provide a valuable resource both for newcomers to the research fields described, and for other scientists seeking detailed background information on special questions. Finally, it provides an accredited documentation of the valuable contributions made by today’s younger generation of scientists.

Theses are accepted into the series by invited nomination only and must fulfill all of the following criteria

- They must be written in good English.
- The topic should fall within the confines of Chemistry, Physics, Earth Sciences, Engineering and related interdisciplinary fields such as Materials, Nanoscience, Chemical Engineering, Complex Systems and Biophysics.
- The work reported in the thesis must represent a significant scientific advance.
- If the thesis includes previously published material, permission to reproduce this must be gained from the respective copyright holder.
- They must have been examined and passed during the 12 months prior to nomination.
- Each thesis should include a foreword by the supervisor outlining the significance of its content.
- The theses should have a clearly defined structure including an introduction accessible to scientists not expert in that particular field.

More information about this series at <http://www.springer.com/series/8790>

Rui Wang

Single Piles in Liquefiable Ground

Seismic Response and Numerical Analysis
Methods

Doctoral Thesis accepted by
the Tsinghua University Beijing, China

 Springer

Author

Dr. Rui Wang
Department of Hydraulic Engineering
Tsinghua University
Beijing
China

Supervisor

Prof. Jian-Min Zhang
Department of Hydraulic Engineering,
School of Civil Engineering
Tsinghua University
Beijing
China

ISSN 2190-5053

Springer Theses

ISBN 978-3-662-49661-9

DOI 10.1007/978-3-662-49663-3

ISSN 2190-5061 (electronic)

ISBN 978-3-662-49663-3 (eBook)

Library of Congress Control Number: 2016934015

© Springer-Verlag Berlin Heidelberg 2016

This work is subject to copyright. All rights are reserved by the Publisher, whether the whole or part of the material is concerned, specifically the rights of translation, reprinting, reuse of illustrations, recitation, broadcasting, reproduction on microfilms or in any other physical way, and transmission or information storage and retrieval, electronic adaptation, computer software, or by similar or dissimilar methodology now known or hereafter developed.

The use of general descriptive names, registered names, trademarks, service marks, etc. in this publication does not imply, even in the absence of a specific statement, that such names are exempt from the relevant protective laws and regulations and therefore free for general use.

The publisher, the authors and the editors are safe to assume that the advice and information in this book are believed to be true and accurate at the date of publication. Neither the publisher nor the authors or the editors give a warranty, express or implied, with respect to the material contained herein or for any errors or omissions that may have been made.

Printed on acid-free paper

This Springer imprint is published by Springer Nature
The registered company is Springer-Verlag GmbH Berlin Heidelberg

Parts of this thesis have been published in the following articles:

1. Wang R, Brandenburg SJ. Beam on nonlinear Winkler foundation and modified neutral plane solution for calculating downdrag settlement. *ASCE Journal of Geotechnical and Geoenvironmental Engineering*, 2013, 139(9): 1433–1442.
2. Wang R, Zhang JM, Wang G. A unified plasticity model for large post-liquefaction shear deformation of sand. *Computers and Geotechnics*, 2014 59: 54–66.
3. Wang R, Fu P, Zhang JM. Finite Element Model for Piles in Liquefiable Ground. *Computers and Geotechnics*, 2016, 72, 1–14.
4. Wang R, Liu X, Zhang JM. Analysis of seismic pile response in liquefiable ground using a constitutive model for large post-liquefaction deformation. *Proceedings of the 6th International Conference on Earthquake Geotechnical Engineering (6ICEGE)*. November 1~4, 2015, Christchurch, New Zealand.
5. Wang R, Zhang JM. Three Dimensional Numerical Simulation of Piles in Liquefiable Ground. *Proceedings of the Fifteenth Asian Regional Conference on Soil Mechanics and Geotechnical Engineering (15ARC)*, November 9–13, 2015, Fukuoka, Japan.
6. Wang R, Zhang JM, Zhang G. Analysis on the Failure of Piles Due to Lateral Spreading. *Rock and Soil Mechanics*, 2011, S1: 501–506. (In Chinese)
7. Wang R, Zhang JM, Zhang G. Centrifuge Shaking Table Test on Single Pile in Lateral Spreading Soil. *Engineering Mechanics*, 2012, 29(10): 98–105. (In Chinese)
8. Wang R, Cao W, Brandenburg SJ, Zhang JM. Beam on nonlinear Winkler foundation solution for calculating downdrag settlement in consolidating and reconsolidating ground. *Chinese Journal of Geotechnical Engineering*, 2015, 37 (3): 512–518. (In Chinese)

Supervisor's Foreword

As Rui Wang's advisor during his Ph.D. program, it is my privilege to write this foreword for his dissertation, accepted for publication within the Springer Theses book series.

Dr. Rui Wang started his Ph.D. program in August 2009 at the Department of Hydraulic Engineering, School of Civil Engineering in Tsinghua University. During his Ph.D. program, he exhibited his tremendous work ethic, high self-motivation and outstanding ingenuity. He received numerous scholarships and awards over the course of the 5-year Ph.D. program, including the Best Paper Award in Geoshanghai 2010 International Conference and the Award for Excellent Doctoral Student from the Chinese Ministry of Education. He has also been actively participating in international collaborations, presenting his work at several international conferences, visiting UCLA for 6 months, and serving the local organizing committee for the IS-model 2012 conference. In July 2014, he graduated with top honours from Tsinghua University. It has been my pleasure to work with him during the past 5 years.

New methods and models have been developed in this dissertation for the numerical analysis of the piles in liquefiable ground. These new methods have provided new grounds for understanding the behaviour of piles in liquefiable ground. Critical conditions for both lateral and axial design conditions were investigated, revealing new evidence and data for the coupling of lateral structure–pile inertial interaction and soil–pile kinematic interaction, and showing the importance of post-liquefaction on the downdrag settlement of piles.

For those interested in soil liquefaction, constitutive modelling, dynamic soil–structure interaction, and seismic pile design, this dissertation will provide new insights and understandings.

Beijing, China
December 2015

Prof. Jian-Min Zhang

Abstract

The seismic response of piles in liquefiable ground is an important and challenging topic in the field of geotechnical earthquake engineering. Through a combination of case analysis, centrifuge shaking table experiments and numerical simulations, the seismic response patterns of single piles in liquefiable ground are revealed, and the axial pile force and settlement during post-earthquake reconsolidation is studied. A complete set of numerical method for the analysis of single piles in liquefiable soils is established, consisting of constitutive formulations, numerical algorithms and modelling techniques. The main achievements are as follows:

1. A three-dimensional unified plasticity model for large post-liquefaction shear deformation of sand is formulated and implemented for finite element analysis, based on which a three-dimensional dynamic finite element analysis method for piles in liquefiable ground is developed. The constitutive model is able to achieve a unified description of the behaviour of sand at different states under monotonic and cyclic loading during both pre- and post-liquefaction regimes. Appropriate stress integration algorithm, three-dimensional stress projection algorithm and parallel computation techniques are applied in the OpenSees implementation of the model. The potential of the model and its numerical implementation are explored via simulations of classical element and centrifuge experiments. The finite element analysis method is validated against centrifuge shaking table experiments.
2. Methods for the analysis of consolidation and reconsolidation-induced pile axial force and settlement with a consideration for consolidation process are proposed. A beam on nonlinear Winkler foundation (BNWF) solution and a modified neutral plane solution are developed and validated against centrifuge experiments for piles in consolidating and reconsolidating ground.
3. The seismic response of single piles in liquefiable ground is studied, including basic force-resistance mode, kinematic and inertial interaction coupling mechanism and major influence factors. The roles of kinematic and inertial effects could differ due to the difference in rotational constraint at the pile head. Moment caused by kinematic and inertial interaction is opposite for single piles

with pile cap, while being of the same direction for single piles without pile cap. The total moment caused by dynamic interaction is affected by both the amplitude and the phasing of the two types of interactions. The dominating forces for piles with and without caps are kinematic and inertial forces, respectively. Pile residual moment increases with increasing lateral spreading in sloping ground. The existence of a non-liquefiable layer over the underlying liquefiable layer may cause the maximum moment to occur at the layer interface.

4. The axial forces and settlement of piles during post-earthquake reconsolidation were analysed. The maximum pile axial force caused by post-earthquake induced negative friction is irrelevant to the reconsolidation process, and is only determined by the final state of the ground. However, pile settlement is dependent on the soil settlement at the neutral plane during reconsolidation, while the neutral plane position changes during the reconsolidation process.

Keywords Liquefaction · Pile foundation · Constitutive model · Seismic response pattern · Numerical analysis method

Acknowledgements

I would like to express my most sincere gratitude to Prof. Jian-Min Zhang of Tsinghua University. As my advisor, Prof. Jian-Min Zhang provided me with great guidance over the 5 years of my Ph.D. program. His tutelage and encouragement opened the doors to research in the field of geotechnical earthquake engineering for me.

Professor Ga Zhang helped immensely by offering his expertise not only for the work in this dissertation, but also for research as a whole. Professor Scott Brandenburg devoted a lot of time and effort in our work on downdrag calculation of piles, and also provided invaluable advice on the numerical implementation of constitutive models. Discussions with Prof. Yannis Dafalias were extremely helpful in the development of the constitutive model in this dissertation. Kunting Yin, Ruihua Zheng and Jizeng Dong assisted in conducting the centrifuge tests. Dr. Gang Wang, Dr. Pengcheng Fu, Dr. Fuqiang Wang and current Tsinghua Ph.D. candidate Wei Cao also helped with various aspects of the dissertation.

Funding for the work in this dissertation was provided by the National Natural Science Foundation of China (No. 51079074 and No. 51038007). I would also like to acknowledge the Chinese Scholarship Council for providing the funding that enabled me to visit UCLA during my Ph.D. program.

Finally, I would also like to dedicate this dissertation to my wife, Huijuan Cui, and my parents, Yucai Wang and Jianying Dong, for their love and support, and for being there for me throughout my Ph.D.

Contents

1	Introduction	1
1.1	Background	1
1.2	Case Histories of Pile Failures in Liquefiable Ground	3
1.2.1	Failure Cases Due to Lateral Effects	3
1.2.2	Failure Cases Due to Vertical Effects	8
1.3	Soil Liquefaction	10
1.3.1	Post-liquefaction Shear Deformation Mechanism	10
1.3.2	Constitutive Modelling of Soil Liquefaction	11
1.4	Seismic Response of Piles in Liquefiable Ground	13
1.4.1	Soil-Pile Kinematic Interaction	13
1.4.2	Structure-Pile Inertial Interaction	14
1.4.3	Coupling of Kinematic and Inertial Interactions	15
1.5	Downdrag of Piles in Consolidating Ground	16
1.5.1	Consolidation Induced Dragload and Downdrag Settlement	16
1.5.2	Post-liquefaction Reconsolidation Induced Dragload and Downdrag Settlement	18
1.6	Scope of Dissertation	19
	References	20
2	A Unified Plasticity Model for Large Post-liquefaction Shear Deformation of Sand and Its Numerical Implementation	25
2.1	Model Formulation in Triaxial Stress Space	26
2.1.1	Basic Equations	26
2.1.2	Elastic Moduli	27
2.1.3	State Parameter	27
2.1.4	Plastic Loading and Load Reversal	28
2.1.5	Plastic Modulus	28
2.1.6	Dilatancy	29
2.1.7	Post-liquefaction Shear Deformation	30

- 2.2 Multiaxial Generalization 31
- 2.3 Determination of Model Parameters 34
- 2.4 Model Implementation 35
 - 2.4.1 Numerical Treatment for Zero Effective Stress State 35
 - 2.4.2 Stress Integration Scheme 36
 - 2.4.3 Determination of Projection Point on Maximum Stress Ratio Surface 38
 - 2.4.4 Symmetrisation of the Elastic-Plastic Tangent 39
- 2.5 Validation of Model Formulation and Implementation 40
 - 2.5.1 Undrained and Drained Triaxial Experiment Simulation 40
 - 2.5.2 Undrained Cyclic Torsional Experiment Simulation 41
 - 2.5.3 VELACS Centrifuge Experiment Simulation 43
- 2.6 Summary 51
- References 51
- 3 Analysis of Seismic Single Pile Response in Liquefiable Ground 55**
 - 3.1 Centrifuge Test on Single Piles in Liquefiable Ground 55
 - 3.2 3D FEM Method for Simulation of Piles in Liquefiable Ground 57
 - 3.3 Test and Simulation Results 62
 - 3.3.1 LCS, Level Ground with Cap and Superstructure 62
 - 3.3.2 ICS, Inclined Ground with Cap and Superstructure 64
 - 3.3.3 LNN and LNS, Level Ground without Cap, without and with Superstructure 67
 - 3.4 Seismic Response of Single Piles in Liquefiable Ground 69
 - 3.4.1 Major Factors Influencing Pile Responses 69
 - 3.4.2 Role of Inertial and Kinematic Effects 75
 - 3.4.3 Coupling of Inertial and Kinematic Effects 78
 - 3.5 Summary 87
 - References 88
- 4 Dragload and Downdrag Settlement of Single Piles due to Post-liquefaction Reconsolidation 91**
 - 4.1 Calculation Method for Dragload and Downdrag Settlement 91
 - 4.1.1 Fundamental Error in Traditional Neutral Plane Solution 91
 - 4.1.2 Beam on Nonlinear Winkler Foundation Solution 92
 - 4.1.3 Modified Neutral Plane Solution 99
 - 4.1.4 Calculation Method for Post-liquefaction Reconsolidation Process 102

- 4.2 Method Validation 103
 - 4.2.1 Simulation of Single Pile in Consolidating Soil 103
 - 4.2.2 Simulation of Single Pile in Post-liquefaction
Reconsolidating Soil 106
- 4.3 Dragload and Downdrag Settlement During Reconsolidation 109
 - 4.3.1 Liquefiable Ground Without Non-liquefiable Crust 110
 - 4.3.2 Liquefiable Ground with a Non-liquefiable Crust 113
- 4.4 Summary 114
- References 115
- 5 Conclusions and Future Work 117**
 - 5.1 Conclusions 117
 - 5.2 Future Work 118

About the Author



Dr. Rui Wang was born in Xi'an, China, in 1987. He received his B.Sc. from Tsinghua University, China, in 2009. From August 2009 to July 2014, he worked on the topics of soil liquefaction and dynamic pile foundation analysis at Tsinghua University. In 2011, he worked on the downdrag of piles and constitutive modelling for liquefiable soil at UCLA for 6 months as a visiting student. In July 2014, he received his Ph.D. degree, graduating *summa cum laude*.

Chapter 1

Introduction

1.1 Background

Pile foundations are one of the most widely used types of foundations in civil engineering, and has often been used in liquefiable grounds. Along with China's booming infrastructure construction, demand for piles has soared over the past few decades in the fields of building, highway, bridge, railway, and offshore windmill construction. It was estimated that a total of 0.3 billion meters of precast piles were manufactured in 2009, worth more than 30 billion RMB.

Traditionally, pile foundations have been considered as an excellent choice for ground improvement in liquefaction susceptible areas due to its advantages in stability and displacement control. However, since the mass occurrences of pile foundation failures in the 1964 Alaska and the 1964 Niigata earthquakes (Ross et al. 1973; Hamada 1992), damage to pile foundations in liquefiable ground have been observed in numerous strong earthquakes, most notably including the 1968 Tokachi-Oki, 1976 Tangshan, 1978 Off-Miyagi, 1989 Loma Prieta, 1995 Hyogoken-Nanbu, 2010 Haiti, 2010 Chile, 2011 Tohoku earthquakes (e.g. Ishihara 1997; Tokimatsu et al. 1998, 2012; Stewart and Brandenberg 2010; Yen et al. 2011). Ross et al. (1973) pointed out in their report that during the 1964 Alaska earthquake, piles in liquefiable ground almost all experienced different levels of damage, while those in gravelly soil which did not liquefy generally performed well. After the 1964 Niigata earthquake, Hamada (1992) investigated the permanent soil deformation through aerial photography and photomapping, showing that many cases of pile foundation failures were strongly related to the ground deformation due to liquefaction.

Over the past 30 years, more and more infrastructure have been constructed in seismically active areas. However, design and analysis methods for the seismic response and demand of piles, especially in liquefiable ground has lagged behind practice. Currently, design codes such as the code for seismic design of buildings (2010), technical code for building pile foundations (2008), code for harbour pile

engineering (1999) generally do not have enough emphasis on the seismic design of piles, and do not take into consideration the dynamic effects of earthquake soil-pile-structure interactions. In terms of soil-pile interaction, the technical code for building pile foundations adopts the “m method” for calculating pile subgrade reaction, while the code for harbour pile engineering suggests using the API (2000) p-y methods for structures of significant importance, and the code for seismic design of buildings simply states that the dynamic capacity of piles should be increased by 25 % compared with the static value and that the lateral resistance and skin friction should be reduced accordingly if liquefaction is expected. In terms of soil-structure interaction (SSI), the code for seismic design of buildings indicates that SSI is beneficial and thus does not need to be taken into account in design. The technical code for building pile foundations directly superimposes the peak structure inertial with soil deformation to calculate the demand of piles. This pseudo-static design methods generally over-simplifies the structure-pile inertial interactions and soil-pile kinematic interactions and cannot reflect the actual properties of the dynamic system, which could lead to over-conservative or over-optimistic design under different conditions.

As more and more attention becomes focused on structure and geotechnical earthquake engineering, many experiment technologies and apparatuses have been developed around the world, for example, Japan developed the 12MN shaking table E-Defense after the 1995 Hyogoken-Nanbu earthquake. These technologies have allowed researchers to conduct model experiments on piles in liquefiable ground to investigate the seismic demand and capacity of pile foundations (Boulanger et al. 1999; Dobry et al. 2003; Tokimatsu et al. 2005; Brandenberg et al. 2005). These efforts have greatly enhanced our understanding of the seismic response of piles in liquefiable ground, however, there is still much to be studied in this field.

Most design and analysis methods for piles in liquefiable ground adopts the approach of decomposing the pile response into response caused by soil-pile kinematic interaction and structure-pile inertial interaction, and evaluates each separately. For soil-pile interaction, pseudo-static and dynamic nonlinear Winkler foundation models (p-y) have been widely applied due to its relative simplicity. In regards to liquefied soil, Goh and O’Rourke (1999), Rollins et al. (2005) and Brandenberg et al. (2005) have developed different p-y models, each producing rather different responses. As a means to provide better understanding of the soil-pile-structure system’s seismic response, dynamic continuum based analysis methods have attracted increasing attention, for example Finn and Fujita (2002) and Cheng and Jeremic (2009) developed several finite element simulation methods for piles in liquefiable ground. Since the seismic response of piles is strongly influenced by the behaviour of the soil it is in, appropriate constitutive description for the behaviour of saturated sand is essential for the analysis of piles in liquefiable ground. The work by Zhang and Wang (2012) revealed the physics of large post-liquefaction deformation of sand and proposed a plasticity model for the liquefaction of sand, providing a key basis for numerical simulation of piles in liquefiable ground.

1.2 Case Histories of Pile Failures in Liquefiable Ground

Based on investigations of pile failure case histories, causes of pile failures in liquefiable ground can be categorized using Fig. 1.1. Spatially, the failure modes of piles include lateral failures (i.e. shear or bending failure) and vertical failures (i.e. settlement and possible buckling). In the time domain, pile failure may occur during earthquakes in pre- and post-liquefaction regimes due to dynamic lateral forces and deformation, and due to settlement caused by loss of vertical resistance after liquefaction. Failure may also occur after the earthquake motion ceases in liquefiable ground due to lateral spreading and reconsolidation of the soil. Table 1.1 lists some case histories related with these typical pile failure modes during past earthquakes.

1.2.1 Failure Cases Due to Lateral Effects

Many failures of piles due to lateral effects have been observed to be caused by lateral soil-pile kinematic interaction, such as in the case of 605A Bridge, where the superstructure was not yet constructed when the earthquake struck (Fig. 1.2); soil-pile interaction has also been observed to be a major cause of pile failure, a famous example of which is the failure of the Showa Bridge after the 1964 Niigata earthquake (Figs. 1.3 and 1.4). When the structure inertia is large and the deformation of the ground is relatively small, inertial interaction could become an important cause of pile failure, such as the failure of a 3 story building in the 1995 Kobe earthquake (Fig. 1.5). In many other cases, the lateral failure of piles in liquefiable ground is caused by the combined effects of soil-pile kinematic interaction and structure-pile inertial interaction, a typical case of which is the failure of the piles of the NHK and NHFC Buildings (Fig. 1.6).

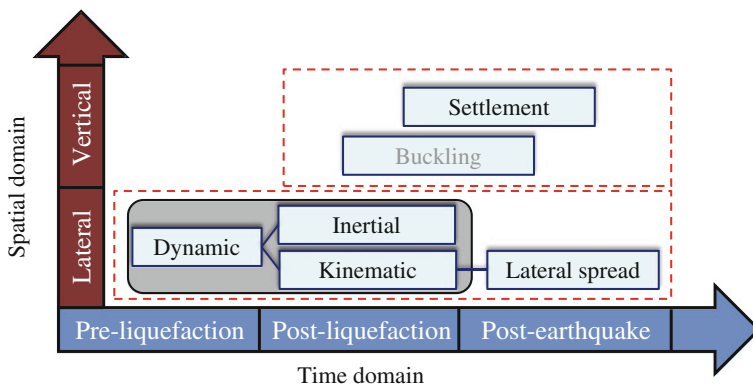


Fig. 1.1 Causes of pile failures in liquefiable ground

Table 1.1 Typical case histories of pile failures in liquefiable ground

Case name	Earthquake event	Failure mode	Reference
605A bridge	1964 Alaska	Lateral (no superstructure)	Ross et al. (1973)
Tianjin Ocean Petroleum Institute Factory	1976 Tangshan	Lateral (no superstructure)	Liu et al. (2010)
Showa bridge	1964 Niigata	Lateral	Iwasaki (1986)
NHK building	1964 Niigata	Lateral	Hamada (1992)
NFCH building	1964 Niigata	Lateral	Hamada (1992)
Railway bridge	1995 Kobe	Lateral	Soga (1997)
Varreux terminal wharf	2010 Haiti	Lateral	Eberhard et al. (2010)
Puerto de Coronel Muelle bridge	2010 Chile	Lateral	Yen et al. (2011)
LPG oil tank	1995 Kobe	Lateral (no lateral spread)	Ishihara (1997)
3 story building	1995 Kobe	Lateral (no lateral spread)	Tokimatsu et al. (1998)
2 story building	1995 Kobe	Lateral (no lateral spread)	Liu (1999)
Yachiyo bridge	1964 Niigata	Lateral, vertical settlement	Fukuoka (1966)
Harbour master's building	2001 Bhuj	Lateral, buckling	Madabhushi et al. (2005)
Juan Pablo II bridge	2010 Chile	Vertical settlement	Yen et al. (2011)
Highway bridge	2010 Baja California	Vertical settlement	Stewart and Brandenburg (2010)
14 story building	2011 Tohoku	Vertical settlement	Tokimatsu et al. (2012)

Note Lateral (no superstructure) means there was no superstructure on the piles at failure, lateral (no lateral spread) means that there was no observable lateral spreading at the site

**Fig. 1.2** Failure of the pile foundation of 605A bridge (Ross et al. 1973)



Fig. 1.3 Photo of the Showa bridge after the 1964 Niigata earthquake (Hamada 1992)

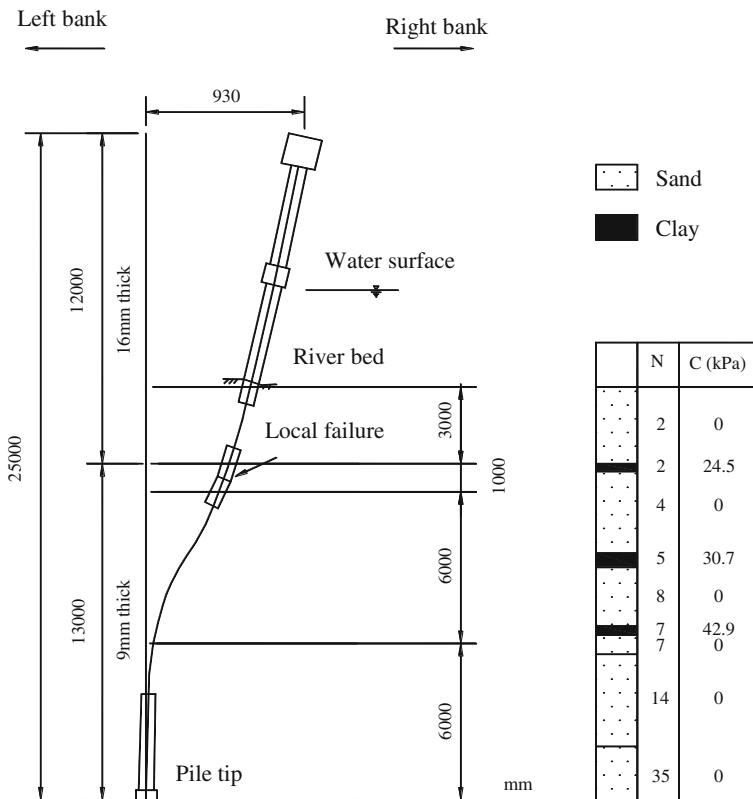


Fig. 1.4 Deformation of P4 and ground characteristics of the Showa bridge



Fig. 1.5 The pile foundation of the NHK building after excavation (Hamada 1992)

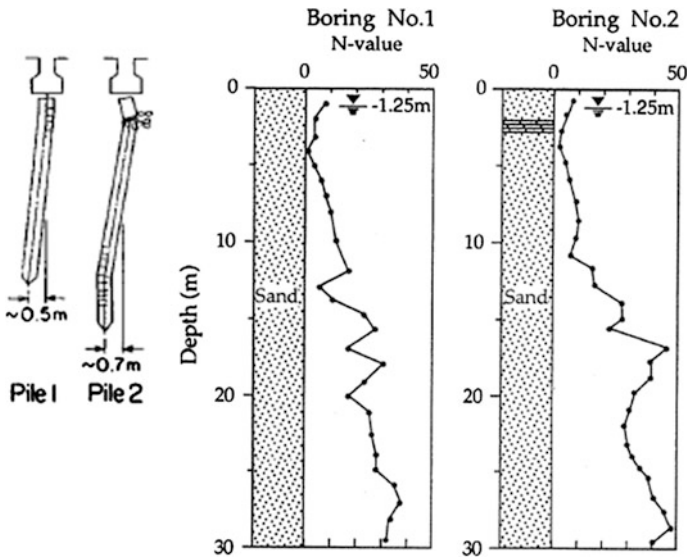


Fig. 1.6 Pile failure and soil characteristics of the NFCH building (Hamada 1992)

The failures of the piles of 605A Bridge in the 1964 Alaska earthquake and the piles of the Tianjin Ocean Petroleum Institute Factory in the 1976 Tangshan earthquake represent two interesting pile failure case histories where the superstructure was not yet in existence at the time of the earthquake, indicating that the pile failures were almost purely caused by soil-pile kinematic interaction. The 27 m long piles of the 605A Bridge experienced a pile head inclination of 15° (Fig. 1.2).

The bridge was located on the Snow River where the ground consisted of 12–18 m of loose sand with SPT resistance of only 5–10, beneath which lay a fine sand layer with blow count over 30 (Ross et al. 1973). The foundation of the Tianjin Ocean Petroleum Institute Factory mainly consisted of 26.5 m long 50 cm × 50 cm² precast piles. The ground had 2 m of sand fill at the top, beneath which lay layers of clay, clay, silt, etc. Large amounts of cracks were found in the piles at 4 m depth after post-earthquake excavation (Liu et al. 2010).

A most famous case of lateral spreading induced pile failure up till now is probably the failure of the Showa Bridge (Fig. 1.3). The Showa Bridge was 303.9 m long, and 24.0 m wide, and consisted of 12 spans. A row of nine 609 mm diameter steel pipe piles supported the bridge between every two spans. Iwasaki (1986) pointed out that 7–8 m of soil in the river bed liquefied during the earthquake, causing 1–2 m of lateral spreading towards the river centre on the left bank. Based on interviews of numerous witnesses, Yoshida et al. (2007) concluded that the collapse of the pile occurred approximately 70s after the seismic motion had stopped. Girder 6 was first to collapse, and then caused girders 3–7 to collapse consecutively (Fig. 1.3). Figure 1.4 shows the deformation of the P4 pile, which was 25 m long, with the top 12 m being 16 mm thick and the bottom 13 m being 6 mm thick. The P4 pile was severely bent towards the river centre at 10 m depth, and a local failure occurred at 3 m depth. The displacement towards the river centre at the top of the pile reached 930 mm. The sand within 10 m depth in the river bed had a blow count of 2–7, with three thin clay layers embedded, the blow count of the sand at the pile tip reached about 35. There have been debate regarding to the cause of the failure of the Showa Bridge piles, possible explanations include lateral spreading, dynamic forces, buckling, etc. However, the most widely accepted theory is that lateral spreading after the earthquake motion had ceased caused the failure.

During the 1995 Kobe earthquake, there were also reports of pile failures in areas where little or no lateral deformation of the ground was observed, e.g. Ishihara (1997) and Tokimatsu (2003). These findings indicate that apart from strong soil-pile interaction due to liquefaction, the inertial force from the superstructure could also be very detrimental to the piles in liquefiable ground.

Apart from the special cases where the pile failures were dominantly caused by one particular phenomenon, most failures were probably due to the combined effects of kinematic soil-pile interaction and inertial structure-pile interaction. The failures of the foundations of the NHK and NFCH buildings are two classic cases where both inertial and kinematic effects contributed to the failures of the piles, with Fig. 1.5 showing the failed piles after extensive excavation investigation 20 years from the Niigata earthquake (Hamada 1992).

The piles of the NFCH Building was 10–14 m long, with radii of 0.35 m. The blow count of the top 12 m at the site was below 10, as typical of liquefiable ground. The precast concrete piles of both NHK and NFCH Buildings endured severe damage at both the pile head and the interface between loose and dense sand 12 m deep (Fig. 1.6).

1.2.2 Failure Cases Due to Vertical Effects

The failure of piles in the vertical direction is mostly due to the excessive or uneven settlement of pile foundations. When the vertical resistance of the pile mostly relies upon liquefiable soil, liquefaction during earthquakes could cause piles to lose its bearing capacity and settle significantly. Figure 1.7 shows the settlement of Yachiyo Bridge during the 1964 Niigata earthquake (Fukuoka et al. 1966), which is an example of this type of failure.

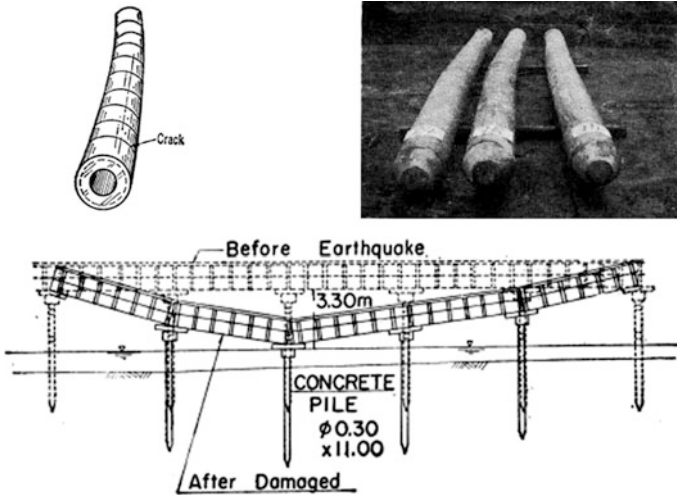


Fig. 1.7 Failure of the Yachiyo bridge due to loss of resistance in liquefied soil (Fukuoka et al. 1966)



Fig. 1.8 Downdrag induced settlement of road bridge piles in the 2010 Baja California earthquake (Stewart and Brandenberg 2010)

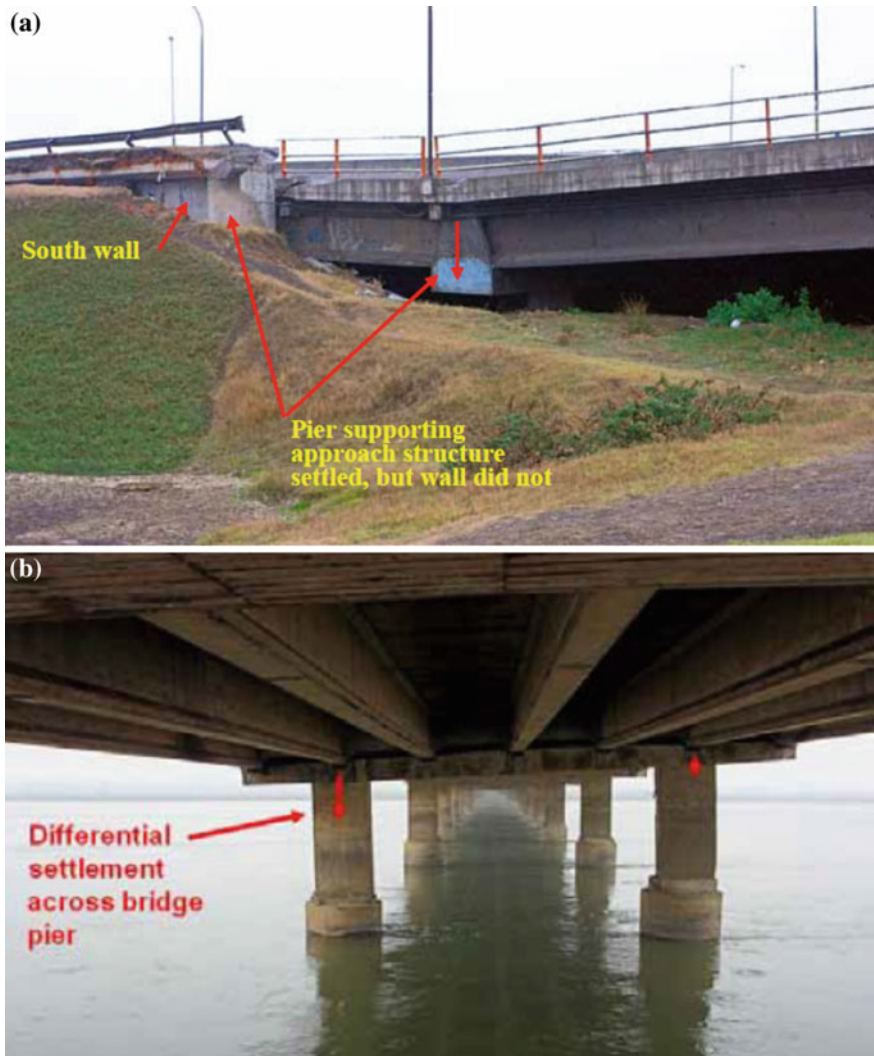


Fig. 1.9 Post-liquefaction downdrag induced settlement of the Juan Pablo II bridge after the 2010 Chile earthquake (Yen et al. 2011). **a** Settlement of pier, **b** differential settlement

Apart from the loss of bearing capacity due to liquefaction, many settlement related failures have been caused by the downdrag of piles during the post-liquefaction reconsolidation process. AASHTO suggests that liquefaction induced dragload and downdrag settlement usually occurs after the earthquake event, when the excess pore pressure begins to dissipate. On one hand, the dragload would increase the axial load on the piles and cause structure failure of the piles, on the other hand, the downdrag settlement could impede the serviceability of the pile foundation.

Figure 1.8 is a photograph of the downdrag induced settlement of road bridge piles in the 2010 Baja California earthquake (Stewart and Brandenburg 2010). Similar but more catastrophic cases were also observed in the 2011 Chile earthquake, where the Juan Pablo II Bridge suffered severe damages due to downdrag settlement (Fig. 1.9).

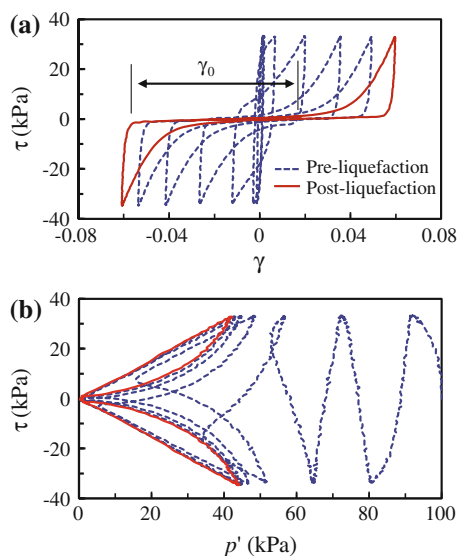
1.3 Soil Liquefaction

Large post-liquefaction deformation is a major cause for seismic liquefaction induced hazards, and has been a subject of extensive research since its observations in several well documented earthquakes (e.g. Seed 1979; Hamada 1992; Yoshida et al. 1992; Eberhard et al. 2010). Understanding the liquefaction related behaviour of sand is an extremely important step the analysis of piles in liquefiable ground.

1.3.1 Post-liquefaction Shear Deformation Mechanism

The accumulation of large but limited shear strains after sand reaches “initial liquefaction” (Seed and Lee 1966) has been observed in numerous laboratory experiments (e.g. Arulmoli et al. 1992; Kutter et al. 1994; Zhang et al. 1997), and is referred to as large post-liquefaction shear deformation (Fig. 1.10).

Fig. 1.10 Stress-strain relation and stress path of undrained cyclic torsional test for Toyoura sand at $D_r = 70\%$ (data from Zhang et al. 1997)



Through observations from a number of cyclic undrained torsional shear tests conducted on hollow cylinder specimens of Toyoura sand, Zhang (1997) noted that after initial liquefaction, while the stress path of each cycle was very much similar (Fig. 1.10b), large but finite shear strain was generated near zero effective stress state during each cycle (Fig. 1.10a), which was referred to as large post-liquefaction deformation. The shear strain generated at liquefaction state was observed to increase with the number of loading cycles, and was defined as a “fluid-like shear strain” γ_0 (Zhang and Wang 2006, 2012).

To explain the physics of post-liquefaction deformation, based on observations on drained cyclic experiments, Shamoto and Zhang (1997) and Zhang (1997) proposed that the volumetric strain of sand consisted of two basic components: mean effective stress change induced ε_{vc} , and dilatancy induced ε_{vd} . The dilatancy induced ε_{vd} was further decomposed into a reversible and an irreversible component, namely $\varepsilon_{vd,re}$ and $\varepsilon_{vd,ir}$. Irreversible dilatancy is the shear induced contraction of sand, which is generally caused by packing and crushing of particles. Reversible dilatancy refers to shear induced expansion and the reversal of such expansion normally caused by particle sliding and reorientation. The decomposition would then be expressed as:

$$\varepsilon_v = \varepsilon_{vc} + \varepsilon_{vd} = \varepsilon_{vc} + \varepsilon_{vd,ir} + \varepsilon_{vd,re} \quad (1.1)$$

Zhang and Wang (2006, 2012) pointed out that since ε_{vc} is solely dependent on the change in effective confining pressure, there exists a threshold $\varepsilon_{vc,0}$ at which zero effective stress is reached. Once this threshold is reached, the ε_{vc} would then be determined the volumetric compatibility Eq. (1.1). For sand to leave liquefaction state when $\varepsilon_{vc} < \varepsilon_{vc,0}$, sufficient dilatancy would be needed, and hence sufficient shear strain would be required according to dilatancy relations.

1.3.2 Constitutive Modelling of Soil Liquefaction

Numerous constitutive models have been developed aiming to simulate the stress-strain behaviour of saturated sands during cyclic loading, including generalized plasticity models (e.g. Pastor et al. 1990; Zienkiewicz and Mroz 1984), hypoplasticity models (e.g. Wu and Bauer 1994; Wu et al. 1996), multi-surface models (e.g. Mroz et al. 1978; Prevost 1985; Parra-Colmenares 1996; Elgamel et al. 2002, 2003; Yang et al. 2003) and bounding surface plasticity models (e.g. Wang et al. 1990; Papadimitriou et al. 2001; Dafalias and Manzari 2004; Wang and Dafalias 2003; Boulanger and Ziotopoulou 2013). Pastor et al. (1990) suggested predicting cyclic mobility through applying a “discrete memory factor” to the plastic modulus in their generalized plasticity model. Wu and Bauer (1994) developed a simple hypoplasticity model that accounts for basic cyclic behaviour of sand, though the model’s independence from stress history limits its application

under complex stress paths. Wang et al. (1990) proposed a bounding surface hypoplasticity model for sand which was able to simulate cyclic stress path through reducing plastic shear modulus with the accumulation of plastic shear strain. Papadimitriou et al. (2001) and Dafalias and Manzari (2004) developed bounding surface plasticity models that simulated sand behaviour under cyclic loading by applying evolving fabric tensors on the plastic modulus and dilatancy rate respectively, enhancing the contraction upon unloading and thus allowing the stress path to approach liquefaction during undrained loading. These models all made significant contributions to the description of cyclic mobility, but none are able to reflect the accumulation of shear strain at liquefaction during each load cycle after initial liquefaction, with stress-strain relationship following almost the same path each cycle, which contradicts experimental findings.

To reflect the shear strain generated at liquefaction, Boulanger and Ziotopoulou (2013) further modified the model by Dafalias and Manzari to achieve the accumulation of shear strain after initial liquefaction by adding fabric history and cumulative fabric terms. In the multi-surface models by Parra-Colmenares (1996), Elgamal et al. (2002, 2003) and Yang et al. (2003), in order to model the accumulation of shear strain near liquefaction state, an additional shear strain accumulation was introduced at a “neutral phase” when the effective stress path crossed the phase transformation line at relatively low effective confining pressure. These two sets of more recent models have taken a big step forward in the simulation of liquefaction behaviour of sand, however both models lack the physical basis for the formulation of post-liquefaction shear strains, causing the shear strain accumulation to be arbitrary and occur at somewhat high shear stress instead of at liquefaction.

Based on their proposed mechanism for large post-liquefaction deformation of sand, Zhang and Wang (2012) formulated a constitutive model within the framework of bounding surface plasticity suited for two dimensional stress space. The model proved capable in simulating the cyclic mobility and large post-liquefaction shear deformation of sand. However, the model does underestimate contraction during initial loading and may overestimate it during load reversal. And as critical state behaviour was not considered, it does not comply with critical state soil mechanic principles and is not able to provide unified description of sand under different densities and confining pressures with a same set of parameters.

Significant progress on clarifying the role of critical state (Roscoe et al. 1958; Schofield and Wroth 1968) for sand has been made over the past few decades through rigorous work by various researchers, including Been and Jefferies (1985), Ishihara (1993), Wood et al. (1994), Li and Dafalias (2000), etc. Thus making the unified constitutive description for sand of different densities and confining pressures possible, which has been an approach adopted by numerous recent constitutive models (e.g. Wood et al. 1994; Li and Dafalias 2000; Papadimitriou et al. 2001; Dafalias and Manzari 2004; Boulanger and Ziotopoulou 2013). These previous research have provided valuable insights into the mechanical behaviour of sands.

1.4 Seismic Response of Piles in Liquefiable Ground

It is well recognized that the analysis of the seismic response of piles in liquefiable ground is an extremely important and, due to its intrinsic complexity, challenging subject in geotechnical earthquake engineering. Such analysis have evolved from simple static methods to more sophisticated high fidelity numerical simulations.

1.4.1 Soil-Pile Kinematic Interaction

A variety of pseudo-static analysis methods have been proposed and adopted by design guidelines and codes for assessing the behaviour of piles in liquefiable ground. The Japanese Road Association (JRA 2002) and Dobry et al. (2003a, b) suggested force-based methods that treat liquefied soil layers as a limit lateral pressure acting on piles. Many other studies have adopted displacement-based approaches in the form of a static “beam on nonlinear Winkler foundation (BNWF)” or the “p-y” method, where soil resistance is reflected through a series of nonlinear springs attached to the pile. After introducing the nonlinear p-y method for laterally loaded piles (Reese and Matlock 1956; McClelland and Focht 1958; Matlock 1970; Reese et al. 1988; API 2000), and others established p-y curves for clays and sands that have been widely adopted. Subsequently, the p-y method was extended to liquefiable soils based on observations from shaking table, centrifuge shaking table, and field blast-induced liquefaction tests (Liu and Dobry 1995; Brandenburg et al. 2005; Cubrinovski et al. 2006), by applying a “p multiplier” (AIJ 2001; Brandenburg et al. 2007), or by developing specific p-y curves for liquefied sand (Goh and O’Rourke 1999; Rollins et al. 2005). Combining the force- and displacement-based methods, Cubrinovski et al. (2006) proposed to use limit pressures for non-liquefied crust layers and linear springs with a “stiffness degradation factor” for liquefied layers during liquefaction-induced lateral spreading. While the aforementioned pseudo-static methods are able to reflect the basic force-displacement relationship of soil-pile interaction and can be performed with ease, they are incapable of capturing the dynamically evolving soil properties and their effects on soil-pile interaction during earthquakes. Pseudo-static methods also suffer difficulties in appropriately combining inertial and kinematic loads (Liyanapathirana and Poulos 2005; Tokimatsu et al. 2005; Caltrans 2013).

Dynamic analysis is not limited by the empirical assumptions of pseudo-static methods, and can reflect the progressive changes in soil-pile interaction in liquefiable ground. Based on a dynamic p-y element developed by Boulanger et al. (1999) that incorporated elastic, plastic, damping and gap components, Brandenburg et al. (2012) associated the capacity of the p-y material linearly with the effective stress in the free field for the degradation of p-y behaviour due to liquefaction. Liyanapathirana and Poulos (2005) used a degraded soil stiffness instead of effective stress of the free field in their p-y formulation to take

liquefaction into consideration. These methods utilize the ground motion and effective stress obtained from free field site response analysis, but cannot accurately consider near field properties. Varun (2010) proposed a semi-empirical method of generating near field pore pressure from free field values and plastic work in the p - y element, which to some extent incorporates the effect of near-field soil.

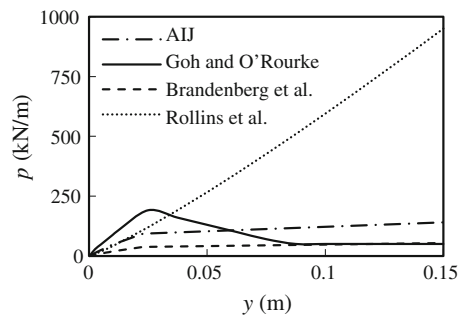
Although p - y methods provide a useful means to reflect the interaction between pile and free-field soil in liquefiable ground, they over-simplify the dynamic response of soil and the approximation of the material properties tend to be rather crude. Figure 1.11 shows the p - y curves calculated for the liquefied Showa Bridge site, showing strong discrepancies between various models.

1.4.2 Structure-Pile Inertial Interaction

Extensive studies have been dedicated to the structure inertia considering soil-structure interaction (e.g. Novak 1974; Gazetas and Mylonakis 1998; Mylonakis and Gazetas 2000; Jeremić et al. 2004). Since soil's constraint on pile foundations is far from rigid, the superstructure's natural period would increase if soil-structure interaction is taken into account. Most current design codes assume that the structure nature period is larger than the characteristic site period, and thus consider SSI to be beneficial, which can be neglected in conservative design. However, Gazetas and Mylonakis (1998) showed that during the 1977 Bucharest, 1985 Mexico City, and 1995 Kobe earthquakes, the peak response spectral occurred at periods larger than 1 s, while most design codes have characteristic site period less than 1 s, which means that neglecting the effects of SSI may actually lead to over-optimistic design.

Novak (1974) and Gazetas and Dobry (1984) formulated impedance pile head models to allow for the calculation of structure inertia considering the effects of SSI. These models have clear physical meanings and are simple to use, but is limited in their application due to the high non-linearity and complexity of the SSI problem.

Fig. 1.11 p - y Relationship for the Showa bridge site



1.4.3 *Coupling of Kinematic and Inertial Interactions*

Apart from the individual inertial and kinematic components of the seismic soil-pile-structure response problem, another important yet puzzling question that has drawn increasing attention is how the inertial and kinematic effects combine to generate the dynamic pile demand, especially in liquefiable grounds (Badelow and Poulos 2015; Khosravifar et al. 2015). Various design codes and pseudo-static analysis studies have adopted distinctly different methods in combining the inertial and kinematic effects. The Caltrans guidelines (2013) suggest that the peak pile demand can be estimated by summing 100 % of the kinematic demand with 50 % of the inertial demand, which would provide a rough account for the fact that the peak kinematic and inertial demands may not occur simultaneously. The Caltrans guidelines (2013) also point out that in some cases the kinematic and inertial loading of the same direction may have opposite effects. The AASHTO design specifications (2010, 2014) assume that pile moments are mainly induced by lateral loads from the superstructure, and thus use only the inertial forces in pseudo-static design. Abghari and Chai (1995) proposed that 25 or 50 % of the peak inertial force should be combined with the peak kinematic displacement for the calculation of pile demand, depending on whether the pile deflection or moment was being calculated. Tabesh and Poulos (2001) showed that using the full peak inertial force worked well in their pseudo-static analysis. Liyanapathirana and Poulos (2005) suggested the above method overestimates the inertial demand in liquefiable ground, and instead used the maximum ground surface acceleration to calculate the inertial demand.

Observations from dynamic tests, including shaking table tests and centrifuge shaking table tests, have been used to shed more light on this issue. Based on results from a series of shaking table tests on piles in dry and liquefiable sands, Tokimatsu et al. (2003, 2005) suggested that the inertial force and ground displacement are in phase when the natural period of the superstructure is less than that of the ground, which is always true for liquefied ground, while being out of phase elsewhere. If the inertial and kinematic effects are in phase, the maximum pile demand occurs when the inertial force and ground displacement are both at their peaks and acting in the same direction, else the maximum pile demand occurs when neither is at a maximum (Tokimatsu et al. 2005). However, Adachi et al. (2004) showed that in liquefied ground, where the natural period of the superstructure is supposedly less than that of the ground, the maximum inertial force and the maximum kinematic displacement may not act on the pile simultaneously, the phasing of these two components with each other and also with the maximum pile demand depends on soil conditions. Brandenberg et al. (2005) and Chang et al. (2005) exhibited that during liquefaction, the phasing of inertial and kinematic effects could change with the change of pile foundation setup.

The discrepancies in the observed test results and among various design methods indicate that further investigation is needed to understand the coupling of the inertial and kinematic demands on piles. Recent developments in dynamic

numerical simulation methods for piles in liquefiable ground can provide an important means to conduct such investigations.

Three-dimensional (3D) dynamic continuum methods can model soil-pile interaction in liquefiable ground with a high fidelity by properly taking into account the effects of kinematic and inertial interactions, the effects of pore water pressures, and nonlinear constitutive behaviour of soil (Finn 2004). Finn and Fujita (2002) proposed a 3D finite element model that used an equivalent linear constitutive model for soil and beam elements which were connected directly to the soil elements for piles. However, Wotherspoon (2006) and Sanchez and Roesset (2013) reported that because the geometrical cross section of the pile is not reflected through the beam elements, directly connecting one-dimensional pile beam elements with soil elements tends to underestimate the stiffness of the pile. Cheng and Jeremic (2009a, b) and Lu et al. (2011) created a void in the finite element mesh to represent the pile hole, and connected the pile beam-column elements with surrounding soil elements using rigid beam-column links, aiming at physically representing the pile cross section. Fully 3D models representing piles with solid elements can be used with appropriate element types and meshing accounting for bending of the pile (Jie et al. 2013), thereby providing a more realistic physical representation of the soil-pile system. Soil constitutive model is a crucial component and should adequately reflect physical processes including plasticity, dilatancy, cyclic mobility, and especially post-liquefaction deformation. Cheng and Jeremic (2009a, b) used the Dafalias and Manzari (2004) model and Lu et al. (2011) a multiyield surface plasticity model (Yang et al. 2003) for sand. However, neither of these models was able to provide ideal description of the post-liquefaction behaviour of sand (Wang et al. 2014).

1.5 Downdrag of Piles in Consolidating Ground

Pile foundations embedded in soil profiles that settle due to surcharge loading, ground water level drop, liquefaction, etc., are subject to increased axial loads (i.e., drag load) and/or pile head settlements (i.e., downdrag).

1.5.1 *Consolidation Induced Dragload and Downdrag Settlement*

Consolidation-induced downdrag and drag load have been the topic of numerous field studies utilizing instrumented piles (e.g., Bjerrum et al. 1969; Endo et al. 1969; Fellenius 1972, 1984; Poulos and Davis 1980). Based on field observations Fellenius (1972) developed the neutral plane solution, NPS, where the neutral plane is the depth of maximum axial load marking the transition between downward shaft friction and upward shaft friction. The neutral plane depth is typically computed by

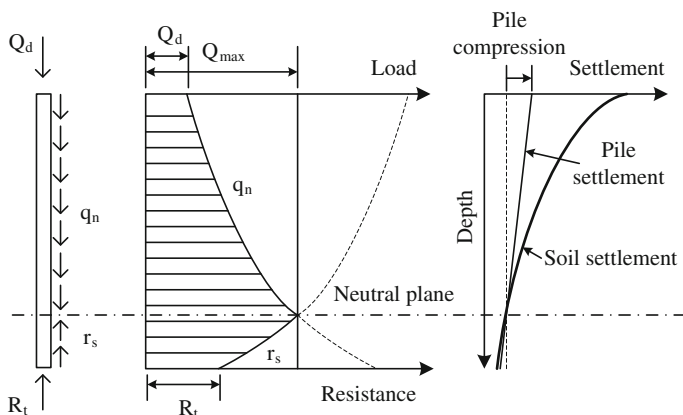


Fig. 1.12 Illustration of the neutral plane solution (after Fellenius 1984)

summing axial loads from the top down and from the bottom up, and by force equilibrium the neutral plane lies at the intersection of these two lines as shown in Fig. 1.12. Typically the shaft friction capacity, f_s , is assumed to be mobilized along the full length of the pile because small relative displacements between soil and pile are required to mobilize f_s . Based on the observation that shaft friction is mobilized in an upward direction when the pile settles more than the soil, and in a downward direction when the soil settles more than the pile, Fellenius (1972) postulated that the soil settlement and the pile settlement are identical at the neutral plane. This approach has been widely used to calculate downdrag settlement, and has been adopted by several design guidelines (AASHTO 2014; Hannigan et al. 2006; Canadian Geotechnical Society 1992; Ministry of Housing and Urban-Rural Development of China 2008, 2010; Ministry of Transport of China 2012, etc.).

Although the neutral plane concept has contributed significantly to our understanding of piles in settling ground, several assumptions made in its typical application may deviate from actual loading conditions. First, as soil expels pore water during consolidation the effective stress increases, thereby resulting in time- and depth-varying f_s and time-varying neutral plane depth. Second, shaft friction exhibits elasto-plasticity such that relative displacements between a pile and soil may be small enough to mobilize only a portion of the ultimate shaft friction capacity, whereas full mobilization (i.e., rigid-plastic response) is typically assumed. Third, tip resistance is often assumed to be constant whereas in reality it depends on pile tip settlement.

To address these assumptions, a number of studies have approached the downdrag problem using continuum numerical solutions (e.g., Esmail 1996; Lee and Ng 2004; Jeong et al. 2004; Hanna and Sharif 2006; Sun and Yan 2010). However, the interface between the soil and pile requires careful selection of contact elements, and the complexity of the three dimensional continuum solutions renders them poorly suited to routine use. Due to the computational complexity of modelling a soil continuum, other researchers have adopted a beam on nonlinear Winker foundation (BNWF) approach to the neutral plane problem in which t-z

elements model soil-pile interaction and a beam-column models the pile (e.g., Wong and Teh 1995; Kim and Mission 2011). However, the properties of the interaction elements are typically time-invariant and do not capture the evolution of effective stress at the soil pile interface during consolidation, and therefore neglect the evolution of shaft friction capacity and neutral plane depth with time. Wong and Teh (1995) acknowledge this problem, and suggest using effective stress conditions at the time when downdrag is to be computed (often the end of primary consolidation) to define properties of the t-z materials.

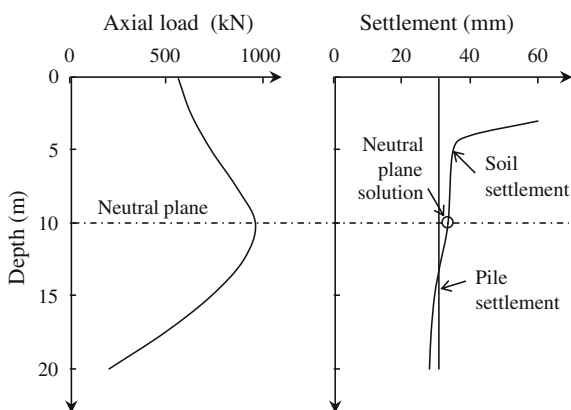
A shift in neutral plane has been observed in many cases by both full scale test and numerical observations. Endo's et al. (1969) observation data from full scale tests in sandy silt, clay, and silt exhibited an upward movement of the neutral of around 5 m in 2 years after pile driving. Bozozuk (1972) recorded the axial load distribution of piles in fine soils and clay deposit over 10 years after pile driving, and test results showed a 5 m downward shift in the neutral plane position. Sun and Yan (2010) conducted finite element simulations of a single pile in consolidating ground due to surcharge considering slip between pile and soil and found the neutral plane to move downwards during consolidation (2.13) (Fig. 1.13).

1.5.2 Post-liquefaction Reconsolidation Induced Dragload and Downdrag Settlement

In Strand's (2008) blast-induced liquefaction tests, the post-reconsolidation induced dragload and downdrag settlement of piles was observed. The tests showed that during the reconsolidation process, the axial pile force increases due to dragload, and the pile settles due to downdrag. The neutral plane was observed to change its position during the reconsolidation process.

Stringer and Madabhushi (2013) conducted a series of centrifuge shaking table experiments and also showed that the pile axial force and settlement would increase

Fig. 1.13 Difference in pile settlement between neutral plane solution and numerical simulation (data from Sun and Yan 2010)



during the reconsolidation phase after the seismic motion. In their experiments, the permeability and tip resistance of the ground was observed to affect the drag load and downdrag settlement.

Fellenius and Siegel (2008) suggested that the traditional NPS can still be used for calculating the dragload and downdrag of piles due to post-liquefaction reconsolidation. They proposed that when the neutral plane is beneath the liquefied layer, the reconsolidation process has almost no contribution to the settlement of the pile, and when the neutral plane is above the liquefied layer, the loss of skin friction in the liquefied layer would cause more pile tip resistance to be mobilized.

Due to the significant change in the pore pressure in the ground during reconsolidation, the position of the neutral plane would also experience obvious changes, which raises the question of which neutral plane position during the reconsolidation process should be used to calculate the dragload and downdrag of piles. Boulanger and Brandenburg (2004) demonstrated that accounting for the evolution of shaft friction capacity and the associated changes in neutral plane depth can result in significant differences in estimated downdrag settlement.

1.6 Scope of Dissertation

The main objective of this dissertation is to study the seismic behaviour of single piles in liquefiable soil by reproducing the seismic response, analysing the response mechanism, and developing calculation methods. In order to achieve these objectives, the dissertation is organized into the following chapters:

Chapter 2: A unified plasticity model for large post-liquefaction shear deformation of sand and its numerical implementation. The formulation and numerical implementation of a unified constitutive model for seismic liquefaction analysis based on the physics of post-liquefaction deformation is presented and validated. The model is unique in that it provides a unified description of sand of different conditions from pre- to post-liquefaction under monotonic and cyclic loading.

Chapter 3: Analysis of seismic single pile response in liquefiable ground. A series of centrifuge shaking table tests on single piles in liquefiable ground are conducted. A three dimensional finite element analysis method is developed and applied on the simulation of the centrifuge tests. The major influence factors, role of inertial and kinematic effects, and coupling of inertial and kinematic effects for single piles in liquefiable ground are investigated.

Chapter 4: Dragload and downdrag settlement of single piles due to post-liquefaction reconsolidation. A beam on nonlinear Winkler foundation (BNWF) solution is developed for the analysis of dragload and downdrag settlement of single piles in consolidating and post-liquefaction reconsolidating ground. A modified neutral plane solution that is amenable to hand calculation is also formulated. The proposed BNWF and modified neutral plane solutions are validated against measurements from a centrifuge tests. Factors influencing the

dragload and downdrag settlement of single piles during post-liquefaction reconsolidation is studied

Chapter 5: Conclusions and future work. The main findings of the dissertation is summarized, with recommendations for future research on pile foundations in liquefiable ground.

References

- Abghari A, Chai J. Modeling of soil-pile-superstructure interaction for bridge foundations. In: Proceedings, Performance of Deep Foundations under Seismic Loading, ASCE, New York; 1995. p. 45–59.
- Adachi N, Suzuki Y, Miura K. Correlation between inertial force and subgrade reaction of pile in liquefied soil. In: Proceedings of the 13th World Conference on Earthquake Engineering, Vancouver; 2004.
- America Petroleum Institute (API). Recommended practice or planning, designing, and constructing fixed offshore platforms-working stress design. API Recommended Practice, 2A (WSD); 2000.
- American Association of State Highway and Transportation Officials (AASHTO). LRFD bridge design specifications. 3rd ed. Washington, DC; 2010.
- American Association of State Highway and Transportation Officials (AASHTO). Guide specifications for LRFD seismic bridge design. 2nd ed. Washington, DC; 2014 (interim).
- Architectural Institute of Japan (AIJ). Recommendations for design of building foundations. Tokyo: AIJ; 2001 (in Japanese).
- Arulmoli K, Muraleetharan KK, Hossain MM, Fruth LS. VELACS: Verification of Liquefaction Analysis by Centrifuge Studies, Laboratory Testing Program, Soil Data Report, The Earth Technology Corporation, Project No. 90-0562, Irvine, California; 1992.
- Badelow F, Poulos HG. Geotechnical foundation design for some of the world's tallest buildings. In: Proceedings of the Fifteenth Asian Regional Conference on Soil Mechanics and Geotechnical Engineering, Fukuoka; 2015.
- Been K, Jefferies MG. A state parameter for sands. *Geotechnique*. 1985;35(2):99–112.
- Bjerrum L, Johannessen IJ, Eide O. Reduction of negative skin friction on steel piles to rock. In: Proceedings 7th International Conference on Soil Mechanics and Foundation Engineering. Vol 2. Mexico City; 1969. p. 27–34.
- Boulanger RW, Brandenburg SJ. Neutral plane solution for liquefaction-induced downdrag on vertical piles. In: Proceedings ASCE Geo-Trans Conference, California; 2004. p. 27–31.
- Boulanger RW, Ziotopoulou K. Formulation of a sand plasticity plane-strain model for earthquake engineering applications. *Soil Dyn Earthquake Eng*. 2013;53:254–67.
- Boulanger RW, Curras CJ, Kutter BL, Wilson DW, Abghari A. Seismic soil-pile-structure interaction experiments and analysis. *J Geotech Geoenviron Eng*. 1999;125(9):750–9.
- Bozozuk M. Downdrag measurements on a 160-ft floating pipe test pile in marine clay. *Can Geotech J*. 1972;9(2):127–36.
- Brandenburg SJ, Boulanger RW, Kutter BL, Chang D. Behavior of pile foundations in laterally spreading ground during centrifuge tests. *J Geotech Geoenviron Eng*. 2005;131(11):1378–91.
- Brandenburg SJ, Boulanger RW, Kutter BL, Chang D. Static pushover analyses of pile groups in liquefied and laterally spreading ground in centrifuge tests. *J Geotech Geoenviron Eng*. 2007;133(9):1055–66.
- Brandenburg SJ, Zhao M, Boulanger RW, Wilson DW. p-y plasticity model for nonlinear dynamic analysis of piles in liquefiable soil. *J Geotech Geoenviron Eng*. 2012;139(8):1262–74.
- California Department of Transportation (Caltrans). Guidelines on foundation loading and deformation due to liquefaction induced lateral spreading. California; 2013.

- Canadian Geotechnical Society (CGS). Canadian foundation engineering manual, CFEM. 3rd ed. Vancouver: BiTech Publishers; 1992.
- Chang S, Boulanger RW, Kutter BL, Brandenberg SJ. Experimental observations of inertial and lateral spreading loads on pile groups during earthquakes. Austin: GeoFrontiers Conference, Geotechnical Special Publication 133; 2005.
- Cheng Z, Jeremic B. Numerical modeling and simulation of pile in liquefiable soil. *Soil Dyn Earthquake Eng.* 2009;29(11):1405–16.
- Cubrinovski M, Kokusho T, Ishihara K. Interpretation from large-scale shake table tests on piles undergoing lateral spreading in liquefied soils. *Soil Dyn Earthquake Eng.* 2006;26(2–4):275–86.
- Dafalias YF, Manzari MT. Simple plasticity sand model accounting for fabric change effects. *J Eng Mech.* 2004;130(6):622–34.
- Dobry R, Abdoun T, O'Rourke TD, Goh SH. Single piles in lateral spreads: field bending moment evaluation. *J Geotech Geoenviron Eng.* 2003;129(10):879–89.
- Eberhard MO, Baldrige S, Marshal J, Mooney W, Rix GJ. The MW 7.0 Haiti earthquake of January 12, 2010, USGS/EERI Advance Reconnaissance Team; 2010.
- Elgamal A, Yang Z, Parra E. Computational modeling of cyclic mobility and post-liquefaction site response. *Soil Dyn Earthquake Eng.* 2002;22(4):259–71.
- Elgamal A, Yang Z, Parra E, Ragheb A. Modeling of cyclic mobility in saturated cohesionless soils. *Int J Plast.* 2003;19(6):883–905.
- Endo M, Minou A, Kawasaki T, Shibata T. Negative skin friction acting on steel piles in clay. In: *Proceedings 8th International Conference on Soil Mechanics and Foundation Engineering*. Vol 2. Mexico City; 1969. p. 85–92.
- Esmail H. Neutral plane of single piles in clay subjected to surcharge loading. M.S. Thesis. Quebec, Canada: Concordia University; 1996.
- Fellenius BH. Downdrag on long piles in clay due to negative skin friction. *Can Geotech J.* 1972;9(4):323–37.
- Fellenius BH. Negative skin friction and settlement of piles. In: *Proceedings of the Second International Seminar, Pile Foundations*, Nanyang Technological Institute, Singapore; 1984. p. 1–12.
- Fellenius BH, Siegel TC. Pile drag load and downdrag in a liquefaction event. *J Geotech Geoenviron Eng.* 2008;134(9):1412–6.
- Finn WDL. An Overview of the behaviour of pile foundations in liquefiable and non-liquefiable soils during earthquake excitation. In: *Proceedings of the 11th International Conference on Soil Dynamics & Earthquake Engineering*, Berkeley; 2004.
- Finn WDL, Fujita N. Piles in liquefiable soils: seismic analysis and design issues. *Soil Dyn Earthquake Eng.* 2002;22(9–12):731–42.
- Fukuoka M. Damage to civil engineering structures. *Soils Found.* 1966;6(2):45–52.
- Gazetas G, Dobry R. Horizontal response of piles in layered soils. *J Geotech Eng.* 1984;110(1):20–40.
- Gazetas G, Mylonakis G. Seismic soil-structure interaction: new evidence and emerging issues. In: *Proceedings of a Speciality Conference, Geotechnical Earthquake Engineering and Soil Dynamics III*. Vol 75. ASCE Geotechnical Special Publication; 1998. p. 1119–74.
- Goh S, O'Rourke TD. Limit state model for soil-pile interaction during lateral spread. In: *Proceedings of the seventh US-Japan workshop on earthquake resistant design of lifeline facilities and countermeasures against soil liquefaction*, Seattle; 1999. p. 237–60.
- Hamada M. Large ground deformations and their effects on lifelines: 1964 Niigata earthquake. *Case Studies of Liquefaction and Lifelines Performance during Past Earthquake*. Technical Report NCEER-92-0001, National Centre for Earthquake Engineering Research, Buffalo; 1992.
- Hanna AM, Sharif A. Drag force on single piles in clay subjected to surcharge loading. *Int J Geomech.* 2006;6(2):89–96.
- Hannigan PJ, Goble G, Likins GE, Rausche F. Design and construction of driven pile foundations, FHWA-HI-97-013. Washington, DC: National Highway Institute Federal Highway Administration, U.S. Department of Transportation; 2006.
- Ishihara K. Liquefaction and flow failure during earthquakes. *Geotechnique.* 1993;43(3):351–415.

- Ishihara K. Terzaghi oration: geotechnical aspects of the 1995 Kobe earthquake. In: Proceedings of the International Conference on Soil Mechanics and Foundation Engineering, Hamburg; 1997. p. 2047–73.
- Iwasaki T. Soil liquefaction studies in Japan: state-of-the-art. *Soil Dyn Earthquake Eng.* 1986;23(4):49–58.
- Japan Road Association (JRA). Specifications for highway bridges. Tokyo: Public Works Research Institute and Civil Engineering Research Laboratory; 2002.
- Jeong S, Lee J, Lee CJ. Slip effect at the pile-soil interface on dragload. *Comput Geotech.* 2004;31:115–26.
- Jeremić B, Kunnath S, Xiong F. Influence of soil-foundation-structure interaction on seismic response of the I-880 viaduct. *Eng Struct.* 2004;26(3):391–402.
- Jie YX, Yuan HN, Zhou HD, Yu YZ. Bending moment calculations for piles based on the finite element method. *J Appl Math.* 2013.
- Khosravifar A, Ugalde J, Travararou T. Design of piles in liquefied soils for combined inertial and kinematic demands. In: Proceedings of the 6th International Conference on Earthquake Geotechnical Engineering (6ICEGE), Christchurch; 2015.
- Kim H, Mission JLC. Development of negative skin friction on single piles: uncoupled analysis based on nonlinear consolidation theory with finite strain and the load-transfer method. *Can Geotech J.* 2011;48(6):905–14.
- Kutter BL, Chen Y, Shen CK. Triaxial and torsional shear test results for sand. Naval Facilities Engineering Service Center, Contact Report CR 94.003-SHR, Port Hueneme, California; 1994.
- Lee CJ, Ng CWW. Development of down-drag on piles and pile groups in consolidating soil. *J Geotech Geoenviron Eng.* 2004;130(9):905–14.
- Li XS, Dafalias YF. Dilatancy for cohesionless soils. *Geotechnique.* 2000;50(4):449–60.
- Liu HS. A case analysis of earthquake damage of pile foundations. *Earthquake Resistant Eng.* 1999;01:37–43 (in Chinese).
- Liu L, Dobry R. Effect of liquefaction on lateral response of piles by centrifuge model tests. *National Center for Earthquake Engineering Research (NCEER) Bulletin,* 1995;9(1):7-11.
- Liu JL, Gao WS, Qiu MB. Application handbook for the technical code for building pile foundations. Beijing: China Architecture and Building Press; 2010 (in Chinese).
- Liyanapathirana DS, Poulos HG. Pseudostatic approach for seismic analysis of piles in liquefying soil. *J Geotech Geoenviron Eng.* 2005;131(12):1480–7.
- Lu J, Elgamal A, Yan L, Law KH, Conte JP. Large-scale numerical modeling in geotechnical earthquake engineering. *Int J Geomech.* 2011;11(6):490–503.
- Madabhushi SPG, Patel D, Haigh SK. Geotechnical aspects of the Bhuj earthquake, EEFIT Report on the Bhuj Earthquake. London: Institution of Structural Engineers; 2005.
- Matlock H. Correlations for design of laterally loaded piles in soft clay. In: Proceedings of the II Annual Offshore Technology Conference, Houston; 1970. p. 577–94.
- McClelland B, Focht JA Jr. Soil modulus for laterally loaded piles. *Trans ASCE.* 1958;123:1049–86.
- Ministry of Housing and Urban-Rural Development of China. JGJ94-2008 Technical code for building pile foundations. Beijing; 2008 (in Chinese).
- Ministry of Housing and Urban-Rural Development of China. GB50011-2010 code for seismic design of buildings. Beijing; 2010 (in Chinese).
- Ministry of Transport of China. JTS167-4-2012 Code for harbour pile engineering. Beijing; 2012 (in Chinese).
- Mroz Z, Norris VA, Zienkiewicz OC. An anisotropic hardening model for soils and its application to cyclic loading. *Int J Numer Anal Meth Geomech.* 1978;3(2):203–21.
- Mylonakis G, Gazetas G. Seismic soil-structure interaction: beneficial or detrimental? *J Earthquake Eng.* 2000;4(3):277–301.
- Novak M. Dynamic stiffness and damping of piles. *Can Geotech J.* 1974;11(4):574–98.
- Papadimitriou AG, Bouckovalas GD, Dafalias YF. Plasticity model for sand under small and large cyclic strains. *J Geotech Geoenviron Eng.* 2001;127(11):973–83.

- Parra-Colmenares EJ. Numerical modeling of liquefaction and lateral ground deformation including cyclic mobility and dilation response in soil systems. Ph.D. Thesis. Troy, New York: Rensselaer Polytechnic Institute; 1996.
- Pastor M, Zienkiewicz OC, Chan A. Generalized plasticity and the modelling of soil behaviour. *Int J Numer Anal Meth Geomech.* 1990;14(3):151–90.
- Poulos HG, Davis EH. *Pile foundation analysis and design.* New York: Wiley; 1980.
- Prevost JH. A simple plasticity theory for frictional cohesionless soils. *Int J Soil Dyn Earthquake Eng.* 1985;4(1):9–17.
- Reese LC, Matlock H. Nondimensional solutions for laterally loaded piles with soil modulus assumed proportional to depth. In: *Proceedings of the VIII Texas Conference on Soil Mechanics and Foundation Engineering,* Austin; 1956.
- Reese LC, O'Neill MW. Drilled shafts: construction procedures and design methods. Report No. FHWA-HI-88-042. Virginia: U.S. Department of Transportation, Federal Highway Administration, Office of Implementation; 1988.
- Rollins KM, Gerber TM, Lane JD, Ashford SA. Lateral resistance of a full-scale pile group in liquefied sand. *J Geotech Geoenviron Eng.* 2005;131(1):115–25.
- Roscoe KH, Schofield AN, Wroth CP. On the yielding of soils. *Geotechnique.* 1958;8(1):22–53.
- Ross G, Seed H, Migliacio R. Performance of highway bridge foundations in the great Alaska earthquake of 1964. // Committee on the Alaskan Earthquake of the Division of Earth Sciences National Research Council. *The Great Alaska Earthquake of 1964.* Washington, DC: National Academy of Sciences; 1973.
- Sanchez M, Roesset JM. Evaluation of models for laterally loaded piles. *Comput Geotech.* 2013;48:316–20.
- Schofield AN, Wroth CP. *Critical state soil mechanics.* London: McGraw-Hill; 1968.
- Seed HB. Soil liquefaction and cyclic mobility evaluation for level ground during earthquakes. *J Geotech Eng Div.* 1979;105(2):201–55.
- Seed HB, Lee KL. Liquefaction of saturated sands during cyclic loading. *J Soil Mech Found Eng Div ASCE.* 1966;92(SM6):105–34.
- Shamoto Y, Zhang JM. Mechanism of large post-liquefaction deformation in saturated sands. *Soils Found.* 1997;2(37):71–80.
- Soga K. Geotechnical aspects of Kobe earthquake. EEFIT Report on the Kobe Earthquake. London: Institution of Structural Engineers; 1997.
- Stewart JP, Brandenburg SJ. Preliminary report on seismological and geotechnical engineering aspects of the April 4 2010 mw 7.2 El Mayor-Cucapah (Mexico) earthquake. Report of the National Science Foundation-Sponsored Geoenvironmental Extreme Events Reconnaissance (GEER) Team; 2010.
- Strand SR. Liquefaction mitigation using vertical composite drains and liquefaction-induced downdrag on piles: implications for deep foundation design. Ph.D Thesis. Utah: Brigham Young University; 2008.
- Stringer ME, Madabhushi S. Re-mobilization of pile shaft friction after an earthquake. *Can Geotech J.* 2013;50(9):979–88.
- Sun TK, Yan WM. Development of neutral plane on a pile in a consolidating ground. In: *Proceedings of the 2nd International Symposium on Computational Mechanics.* Vol 1233; 2010. p. 1594–99.
- Tabesh A, Poulos HG. Pseudostatic approach for seismic analysis of single piles. *J Geotech Geoenviron Eng.* 2001;127(9):757–65.
- Tokimatsu K. Behaviour and design of pile foundations subjected to earthquakes. In: *Proceedings of the Twelfth Asian Regional Conference on Soil Mechanics and Geotechnical Engineering,* Singapore; 2003. p. 1065–96.
- Tokimatsu K, Hiroshi O, Satake K, Shamoto Y, Asaka Y. Effects of lateral ground movements on failure patterns of piles in the 1995 Hyogoken-Nambu earthquake. In: *Proceedings of a Speciality Conference, Geotechnical Earthquake Engineering and Soil Dynamics III.* Vol 75. ASCE Geotechnical Special Publication; 1998. p. 1175–86.

- Tokimatsu K, Suzuki H, Sato M. Effects of inertial and kinematic interaction on seismic behaviour of pile with embedded foundation. *Soil Dyn Earthquake Eng.* 2005;25:753–62.
- Tokimatsu K, Tamura S, Suzuki H, Katsumata K. Building damage associated with geotechnical problems in the 2011 Tohoku Pacific Earthquake. *Soils Found.* 2012;52(5):956–74.
- Varun. A non-linear dynamic macroelement for soil structure interaction analyses of piles in liquefiable sites. Ph.D Thesis. Atlanta: Georgia Institute of Technology; 2010.
- Wang ZL, Dafalias YF. Simulation of post-liquefaction deformation of sand. *Const Model Geomater.* 2003; 100–7.
- Wang ZL, Dafalias YF, Shen CK. Bounding surface hypoplasticity model for sand. *J Eng Mech.* 1990;116(5):983–1001.
- Wang R, Zhang JM, Wang G. A unified plasticity model for large post-liquefaction shear deformation of sand. *Comput Geotech.* 2014;59:54–66.
- Wong KS, Teh CI. Negative skin friction on piles in layered soil deposits. *J Geotech Eng.* 1995;121(6):457–65.
- Wood MD, Belkheir K, Liu DF. Strain softening and state parameter for sand modelling. *Geotechnique.* 1994;50(4):449–60.
- Wotherspoon LM. Three dimensional pile finite element modelling using OpenSees. In: 2006 NZSEE Conference Proceedings, Napier; 2006.
- Wu W, Bauer E. A simple hypoplastic constitutive model for sand. *Int J Numer Anal Meth Geomech.* 1994;18(12):833–62.
- Wu W, Bauer E, Kolymbas D. Hypoplastic constitutive model with critical state for granular materials. *Mech Mater.* 1996;23(1):45–69.
- Yang Z, Elgamal A, Parra E. Computational model for cyclic mobility and associated shear deformation. *J Geotech Geoenviron Eng.* 2003;129(12):1119–27.
- Yen WP, Chen G, Buckle I, Allen T, Alzamora D, Ger J, Arias JG. Post-earthquake reconnaissance report on transportation infrastructure: impact of the February 27, 2010, Offshore Maule Earthquake in Chile. FHWA-HRT-11-030, Federal Highway Administration, Virginia; 2011.
- Yoshida N, Watanabe H, Yasuda S. Liquefaction-induced ground failure and related damage to structures during 1991 Telire-Limon, Costa Rica, earthquake. In: Proceedings from the 4th Japan-U.S. Workshop on Earthquake Resistant Design of Lifeline Facilities and Countermeasures for Soil Liquefaction, Hawaii; 1992. p. 37–52.
- Yoshida N, Tazoh T, Wakamatsu K, Yasuda S, Towhata I, Nakazawa H, Kiku H. Causes of Showa bridge collapse in the 1964 Niigata earthquake based on eyewitness testimony. *Soils Found.* 2007;47(6):1075–87.
- Zhang JM. Cyclic critical stress state theory of sand with its application to geotechnical problems. Ph.D Thesis. Tokyo: Tokyo Institute of Technology; 1997.
- Zhang JM, Wang G. Mechanism of large post-liquefaction deformation of saturated sand. *Chin J Geotech Eng.* 2006;28(7):835–40 (in Chinese).
- Zhang JM, Wang G. Large post-liquefaction deformation of sand, part I: physical mechanism, constitutive description and numerical algorithm. *Acta Geotech.* 2012;7(2):69–113.
- Zhang JM, Shamoto Y, Tokimatsu K. Moving critical and phase-transformation stress state lines of saturated sand during undrained cyclic shear. *Soils Found.* 1997;2(37):51–9.
- Zienkiewicz OC, Mroz Z. Generalized plasticity formulation and application to geomechanics. *Mech Eng Mater.* 1984; 44:655–79 (Desai CS, Gallagher RH, editors. Wiley).

Chapter 2

A Unified Plasticity Model for Large Post-liquefaction Shear Deformation of Sand and Its Numerical Implementation

This chapter builds on the work of Zhang and Wang (2012) to present the formulation of a unique model that (1) achieves the simulation of post-liquefaction shear deformation based on its physics, allowing the unified description of pre- and post-liquefaction behaviour of sand; (2) directly links the cyclic mobility of sand with reversible and irreversible dilatancy, enabling the unified description of monotonic and cyclic loading; (3) introduces critical state soil mechanics concepts to achieve unified modelling of sand under different states. Modelling of large post-liquefaction shear deformation is achieved based on the physics proposed by Zhang and Wang. The proposed model is able to appropriately describe some important features of sand, including dilatancy during loading and unloading, and softening of dense sand. The model is first described in triaxial stress space, and then generalized into multiaxial stress space with three dimensional mapping rules for the calculation of plasticity and dilatancy. The determination of the model parameters is described. The cutting-plane stress integration scheme and the Pegasus procedure for the three dimensional implementation of the model into the finite-element framework OpenSees (McKenna and Fenves 2001) are presented in detail. The OpenSees platform is chosen for its great capabilities in geotechnical earthquake engineering simulation and most importantly for the model to be openly available to the technical community. Finally, the performance of the model and its three dimensional implementation is evaluated by simulations of classical drained and undrained triaxial experiments on Toyoura sand by Verdugo and Ishihara (1996) and undrained cyclic torsional experiments on Toyoura sand. Simulations of the VELACS centrifuge shaking table tests are also carried out.

2.1 Model Formulation in Triaxial Stress Space

A description of the proposed constitutive model is first provided in triaxial stress space. The model operates within the framework of bounding surface plasticity proposed by Dafalias and Popov (1975) and adopts features of the hypoplasticity model developed by Wang et al. (1990). The model uses the two dilatancy induced volumetric strain components for the successful description of the dilatancy behaviours of sand in both monotonic and cyclic loading, and accounts for the generation of post-liquefaction shear deformation at zero effective confining stress based on the physics of post-liquefaction deformation proposed by Zhang and Wang (2012). Critical state soil mechanics principles were incorporated into the model to allow unified description of sand by introducing the state parameter (Been and Jefferies 1985).

In the current model framework, mean effective pressure change induced volumetric strain is assumed to be elastic and shear induced volumetric strain is assumed to be fully plastic, matching the decomposition of volumetric strain stated previously in Eq. (1.1) with traditional elastic and plastic decompositions.

2.1.1 Basic Equations

The incremental stress-strain relations follow the typical equations for elastic-plasticity:

$$\dot{\varepsilon}_q^e = \frac{\dot{q}}{3G}; \quad \dot{\varepsilon}_v^e = \frac{\dot{p}}{K} \quad (2.1)$$

$$\dot{\varepsilon}_q^p = \frac{\dot{\eta}}{H}; \quad \dot{\varepsilon}_v^p = D \left| \dot{\varepsilon}_q^p \right| \quad (2.2)$$

where the elastic and plastic strains are denoted by superscripts e and p respectively. G and K are the elastic shear and bulk moduli, H is the plastic shear modulus and D dilatancy rate.

The model neglects the plastic volumetric strains during constant stress ratio loading for simplicity, though this proposition would cause underestimation of the reconsolidation settlement of soil. The elastic volumetric strain ε_v^e corresponds to the mean effective stress change induced volumetric strain ε_{vc} , and ε_v^p corresponds to the dilatancy induced volumetric strain $\varepsilon_{vd,ir} + \varepsilon_{vd,re}$ in Eq. (1.1).

2.1.2 Elastic Moduli

The elastic shear and bulk moduli are defined as suggested by Richart et al. (1970):

$$G = G_o \frac{(2.973 - e_{in})^2}{1 + e_{in}} p_a \left(\frac{p}{p_a} \right)^{\frac{1}{2}} \quad (2.3)$$

$$K = \frac{1 + e_{in}}{\kappa} p_a \left(\frac{p}{p_a} \right)^{\frac{1}{2}} \quad (2.4)$$

where e_{in} is the initial void ratio, p_a is the atmospheric pressure for normalization, G_o and κ are material constants. The elastic moduli were defined using the initial void ratio so that elastic volumetric strain is strictly dependent only on effective stress, which decouples the elastic moduli with shear induced volumetric strains. Thus making it consistent with our decomposition of volumetric strains.

2.1.3 State Parameter

For the incorporation of critical state behaviour, and for the unified description of sand at various densities with a same set of parameters, the state parameter Ψ proposed by Been and Jefferies (1985) is introduced to consider the dependency of sand behaviour on the current state.

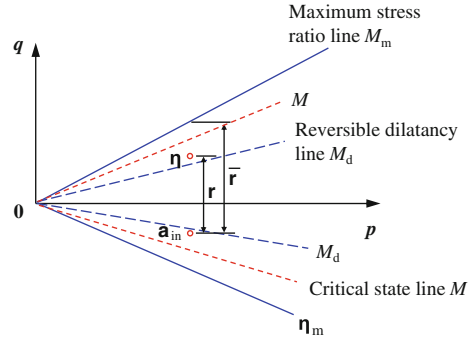
$$\Psi = e - e_c \quad (2.5)$$

with e being the current void ratio and e_c the critical void ratio. At critical state, Roscoe et al. (1958) and Schofield and Wroth (1968) proposed that $e = e_c$ and $q_c/p_c = M$, where M is defined as the critical stress ratio as shown in Fig. 2.1. The relationship between the critical void ratio e_c and mean effective stress is determined using Li and Wang's (1998) power formulation which have proved effective for various types of sands (Li and Wang 1998; Ling and Yang 2006):

$$e_c = e_0 - \lambda_c (p_c/p_{at})^{\xi} \quad (2.6)$$

where e_0 is the void ratio at $p_c = 0$ and λ_c and ξ are constants. By correct consideration for the variation of plasticity and dilatancy with the state parameter, the model is applicable to different pressures and densities using a single set of parameters.

Fig. 2.1 Schematic illustration of critical state, maximum stress ratio and reversible dilatancy lines with mapping rules in triaxial stress space



2.1.4 Plastic Loading and Load Reversal

By adopting Wang's (1990) hypoplasticity approach, plastic loading and load reversal is determined by the sign of:

$$l = \dot{\eta}(\eta - \alpha_{in}) \quad (2.7)$$

where α_{in} is the stress ratio at the previous load reversal. Plastic loading is induced when $l > 0$, and load reversal occurs at $l < 0$.

2.1.5 Plastic Modulus

The plastic modulus and relevant mapping rules in the model are modified from the work of Wang et al. (1990). The peak mobilized stress ratio, which has been shown to be dependent on the state parameter (Been and Jefferies 1985), is here defined using an exponential variation with Ψ as proposed by Li and Dafalias (2000) to be $M_p = M \exp(-n^p \Psi)$. A maximum stress ratio (M_m) surface is proposed to define the mapping rule, as shown in Fig. 2.1 in triaxial stress space. By using the peak mobilized and maximum stress ratios, the plastic modulus can be determined in a way that is related to the bounding surface plasticity concept. Thus, the plastic modulus is expressed as:

$$H = \frac{h}{p} G \exp(-n^p \Psi) \left(\frac{M \exp(-n^p \Psi)}{M_m} \left(\frac{\bar{\rho}}{\rho} \right) - 1 \right) \quad (2.8)$$

where h is a model parameter; n^p is a model constant; ρ is the distance from the current stress ratio η to α_{in} ; and $\bar{\rho}$ is the distance between the projection of current stress on the maximum stress ratio surface and α_{in} (Fig. 2.1).

The maximum stress ratio M_m surface is defined to expand according to the maximum stress ratio that has occurred during loading, until it reaches the peak

mobilized stress ratio $M \exp(-n^b \Psi)$. Once the current stress ratio reaches outside $M \exp(-n^b \Psi)$, the maximum stress ratio follows the current stress ratio until it falls on the peak mobilized stress ratio again. Through this formulation, the plastic modulus $H = 0$ is satisfied at the critical state and the softening response where $H < 0$ is also made possible when the stress ratio exceeds the peak mobilized stress ratio M_p .

2.1.6 Dilatancy

The determination of dilatancy is a unique part of the proposed model. According to the propositions made by Shamoto and Zhang (1997) and Zhang (1997), the dilatancy of sand is decomposed into a reversible and an irreversible component, through which the dilatancy during load reversal and cyclic loading can be properly reflected. In this model, the dilatancy rate D is determined by combining the reversible part D_{re} and irreversible part D_{ir} :

$$D = \frac{\dot{\epsilon}_v^p}{|\dot{\epsilon}_q^p|} = D_{re} + D_{ir} = \frac{\dot{\epsilon}_{vd, re}}{|\dot{\epsilon}_q^p|} + \frac{\dot{\epsilon}_{vd, ir}}{|\dot{\epsilon}_q^p|} \quad (2.9)$$

Through experimental observations Zhang and Wang (2012) pointed out that reversible dilatancy remained on the expansion side, generating and releasing during loading and unloading cycles. The generation and release rate of reversible dilatancy are here defined using separate equations. The generation rate of reversible dilatancy, for which $D_{re, gen}$ is negative, is defined in a form similar to Rowe's (1962) dilatancy theory:

$$D_{re, gen} = d_{re, 1}(M_d - \eta) \quad (2.10)$$

where $d_{re, 1}$ is a reversible dilatancy parameter, and $M_d = M \exp(n^d \Psi)$ is the stress ratio at which reversible dilatancy changes from contraction to expansion, and also follows an exponential variation with Ψ (Li and Dafalias 2000), shown as the reversible dilatancy line in Fig. 2.1. Reversible dilatancy remains non-positive and is released after load reversal, the release rate is defined as:

$$D_{re, rel} = (d_{re, 2} \chi)^2 / p \quad (2.11)$$

$d_{re, 2}$ is another dilatancy parameter used to calculate the release of reversible dilatancy. $\chi = \min(-d_{ir} \frac{\dot{\epsilon}_{vd, re}}{\dot{\epsilon}_{vd, ir}^{pr}}, 1)$ is a function controlling the reversible dilatancy release process, where d_{ir} is an irreversible dilatancy constant and $\dot{\epsilon}_{vd, ir}^{pr}$ is the $\dot{\epsilon}_{vd, ir}$ at previous load reversal. This function χ guarantees $D_{re, rel}$ to be zero when $\dot{\epsilon}_{vd, re}$ is completely released, and restricts the release rate from becoming overly large, thus avoiding the overestimation of contraction upon load reversal. Note that prior to the

first load reversal, χ is set as 0 and the release rate $D_{re,rel}$ is constantly 0. Reversible dilatancy can thus be expressed together as:

$$D_{re} = \frac{\dot{\varepsilon}_{vd,re}}{|\dot{\varepsilon}_q^p|} = \begin{cases} D_{re,gen}, & |\eta| \geq M_{d,c/e} \quad \& \quad |\dot{\eta}| > 0 \\ D_{re,rel}, & |\eta| < M_{d,c/e} \quad \text{or} \quad |\dot{\eta}| < 0 \end{cases} \quad (2.12)$$

It has been observed that the irreversible dilatancy induced volumetric strain $\varepsilon_{vd,ir}$ remains contractive, and followed the pattern of accumulating asymptotically during loading with a decreasing rate during each monotonic shearing since the last stress reversal. Irreversible dilatancy rate D_{ir} is defined to satisfy these features as:

$$D_{ir} = \frac{\dot{\varepsilon}_{vd,ir}}{|\dot{\varepsilon}_q^p|} = d_{ir} \exp(n^d \Psi - \alpha \varepsilon_{vd,ir}) \left(\langle M_d - \eta \rangle + \exp(\chi) + \left(\frac{\gamma_{d,r} \langle 1 - \exp(n^d \Psi) \rangle}{\gamma_{d,r} \langle 1 - \exp(n^d \Psi) \rangle + \gamma_{mono}} \right)^2 \right) \quad (2.13)$$

Here α is a parameter controlling the decrease rate of irreversible dilatancy, γ_{mono} is the shear strain since the last stress reversal and $\gamma_{d,r}$ is a reference shear strain. $\langle \cdot \rangle$ are the MacCauley brackets that yield $\langle x \rangle = x$ if $x > 0$ and $\langle x \rangle = 0$ if $x \leq 0$. The $\exp(n^d \Psi - \alpha \varepsilon_{vd,ir})$ part of the equation reflects asymptotic accumulation of irreversible dilatancy, and the part $\left(\frac{\gamma_{d,r} \langle 1 - \exp(n^d \Psi) \rangle}{\gamma_{d,r} \langle 1 - \exp(n^d \Psi) \rangle + \gamma_{mono}} \right)^2$ reflects the decreasing dilatancy rate during each monotonic loading process. By introducing $\langle M_d - \eta \rangle$ into the formulation, the initial contraction during loading can be appropriately reflected, and $\exp(\chi)$ enhances the contraction upon load reversal. The incorporation of state parameter allows the formulation to take density and effective pressure into consideration and comply with critical state soil mechanic principles.

A most significant result of incorporating the state parameter in the definition of plastic modulus, reversible and irreversible dilatancy is that the model becomes fully compatible with critical state soil mechanics requirements and capable of simulating the behaviour of sand at various densities with the same set of material constants. The unique formulation of plastic modulus and dilatancy rates allows for the appropriate simulation of both monotonic and cyclic loading. These features will be shown in the simulations later in this chapter.

2.1.7 Post-liquefaction Shear Deformation

As plasticity caused by constant η loading is neglected in this model, the volumetric strain caused by mean effective stress change ε_{vc} proposed by Zhang and Wang (2012) in Eq. (2.1) matches ε_v^e in Eq. (2.1). By substituting Eq. (2.4) into Eq. (2.1)

and integrating from the current effective stress p to zero effective stress, the threshold ε_{vc} at which zero effective stress is reached is expressed as a function of p :

$$\varepsilon_{vc,0} = f(p) = -\frac{2\kappa}{1 + e_{in}} \left(\frac{p}{p_a} \right)^{\frac{1}{2}} \quad (2.14)$$

Based on Zhang and Wang's (2012) theory, once the current ε_{vc} (or ε_v^e) decreases beyond the threshold value $\varepsilon_{vc,0}$, sand liquefies and p remains constant at 0, $\dot{\varepsilon}_v^e = \frac{\dot{p}}{K}$ in Eq. (2.1) becomes invalid and ε_{vc} is then determined by the volumetric compatibility equation Eq. (1.1) and is able to exceed $\varepsilon_{vc,0}$.

For sand to exit the state of liquefaction when $\varepsilon_{vc} < \varepsilon_{vc,0}$, sufficient dilation must occur for ε_{vc} to become greater than $\varepsilon_{vc,0}$ again. According to the dilation equation in Eq. (2.2), sufficient dilation would depend on the shear strain ε_q^p generated at liquefaction state, which is the cause of large post-liquefaction shear deformation:

$$\varepsilon_v^p = \int (D_{ir} + D_{re}) d \left| \varepsilon_q^p \right| \quad (2.15)$$

2.2 Multiaxial Generalization

With the model presented fully in triaxial stress space, its multiaxial generalization is then possible. The basic equations for the multiaxial generalization are:

$$\dot{\varepsilon}_v^e = \frac{\dot{p}}{K}; \quad \dot{\mathbf{e}}^e = \frac{\dot{\mathbf{s}}}{2G} \quad (2.16)$$

$$\dot{\varepsilon}_v^p = \langle L \rangle D; \quad \dot{\mathbf{e}}^p = \langle L \rangle \mathbf{m} \quad (2.17)$$

$p = \text{tr}(\boldsymbol{\sigma})/3$ is the mean effective stress, with $\boldsymbol{\sigma}$ being the effective stress tensor; $\mathbf{s} = \boldsymbol{\sigma} - p\mathbf{I}$ is the deviatoric stress, \mathbf{I} being the rank two identity tensor; $\varepsilon_v = \text{tr}(\boldsymbol{\varepsilon})$ is the volumetric strain, $\boldsymbol{\varepsilon}$ being the strain tensor; $\mathbf{e} = \boldsymbol{\varepsilon} - \varepsilon_v/3\mathbf{I}$ is the deviatoric strain tensor. L is the plastic loading index and \mathbf{m} the deviatoric strain flow direction. The deviatoric stress ratio tensor is here defined as $\mathbf{r} = \frac{\mathbf{s}}{p}$, and $q = \sqrt{\frac{3}{2}\mathbf{s} : \mathbf{s}}$, $\eta = \frac{q}{p}$.

The total stress-strain relation can be formulated by combining Eqs. (2.16) and (2.17) to be:

$$\dot{\boldsymbol{\varepsilon}} = \frac{1}{2G} p \dot{\mathbf{r}} + \left(\frac{1}{2G} \mathbf{r} + \frac{1}{3K} \mathbf{I} \right) \dot{p} + \left(\mathbf{m} + \frac{D}{3} \mathbf{I} \right) \langle L \rangle \quad (2.18)$$

with the elastic moduli G and K still defined by Eqs. (2.3) and (2.4).

The critical, maximum stress ratio and reversible dilatancy surfaces shown schematically in Fig. 2.2 are defined by:

$$f_c(\boldsymbol{\sigma}) = \eta - Mg(\theta) = 0 \quad (2.19)$$

$$f_m(\boldsymbol{\sigma}) = \eta - M_m g(\theta) = 0 \quad (2.20)$$

$$f_d(\boldsymbol{\sigma}) = \eta - M_d g(\theta) = 0 \quad (2.21)$$

where θ is the lode angle calculated according to:

$$\theta = \frac{1}{3} \sin^{-1} \left(-\frac{\mathbf{s} : \mathbf{s} : \mathbf{s}}{6q} \right) \quad (2.22)$$

The function $g(\theta)$ in this model follows Zhang's (1997) proposition which showed excellent agreement with test data, and is defined as:

$$g(\theta) = \frac{1}{1 + M_p(1 + \sin 3\theta - \cos^2 3\theta)/6 + (M_p - M_{p,o}) \cos^2 3\theta/M_{p,o}} \quad (2.23)$$

$$M_p = \frac{6 \sin \phi_f}{3 - \sin \phi_f} \quad (2.24)$$

$$M_{p,o} = \frac{2\sqrt{3} \tan \phi_f}{\sqrt{3 + 4 \tan^2 \phi_f}} \quad (2.25)$$

$M_p = M \exp(-n^b \Psi)$ is the peak mobilized stress ratio at triaxial compression and ϕ_f is the corresponding friction angle, $M_{p,o}$ is the peak mobilized stress ratio under torsional shear after isotropic consolidation.

Similar to the triaxial space formulation, plastic loading is determined in three dimensional space by the load index L :

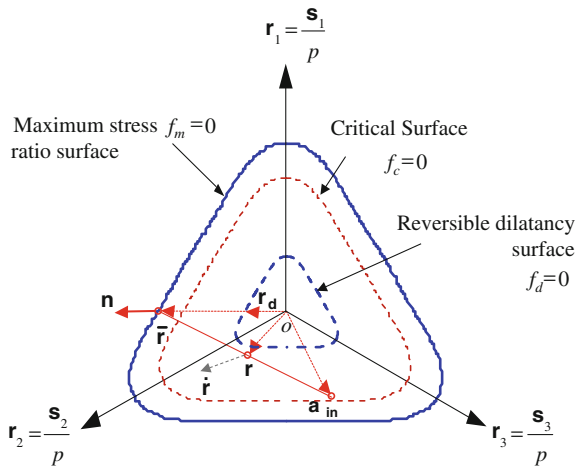
$$L = \frac{\mathbf{L} : \underline{\boldsymbol{\sigma}}}{H} = \frac{p\boldsymbol{\epsilon} : \mathbf{n}}{H} \quad (2.26)$$

Here \mathbf{n} is a unit deviatoric tensor serving as the loading direction in deviatoric stress space in the model, and the loading direction \mathbf{L} is defined as $\mathbf{L} = \mathbf{n} - \frac{1}{3}(\mathbf{n} : \mathbf{r})\mathbf{I}$. Plastic loading is induced when $L > 0$, and load reversal occurs at $L < 0$.

It is further assumed that the deviatoric strain flow direction \mathbf{m} in Eq. (2.17) is the same as the loading direction in deviatoric stress space so as:

$$\mathbf{m} = \mathbf{n} = \bar{\mathbf{r}} / \sqrt{\bar{\mathbf{r}} : \bar{\mathbf{r}}} \quad (2.27)$$

Fig. 2.2 Schematic illustration of critical state, maximum stress ratio and reversible dilatancy surfaces with mapping rules



Here $\bar{\mathbf{r}}$ represents the projection of the current stress point on the maximum stress ratio surface in deviatoric stress space (Fig. 2.2), the mapping rule for this projection is adopted from the work of Wang et al. (1990). As shown in Fig. 2.2, the projection of current stress ratio on the maximum stress ratio surface $\bar{\mathbf{r}}$ is defined as the intersection between the extension of the line from the previous load reversal point α_{in} to \mathbf{r} and the maximum stress ratio surface:

$$\bar{\mathbf{r}} = \alpha_{in} + \beta(\mathbf{r} - \alpha_{in}) \quad (2.28)$$

where β can be solved by substituting Eq. (2.27) into Eq. (2.19). It needs pointing out that although theoretically \mathbf{n} should be the unit normal to the maximum stress ratio surface in deviatoric stress ratio space, due to the numerical difficulty in calculating the normal to the surface, a compromise is made for the model to be numerically applicable by setting the deviatoric loading and flow directions to be the same as $\bar{\mathbf{r}}$ (Fig. 2.2), which is the same approach taken by Andrianopoulos et al. (2010).

When the loading index L is positive, plastic loading occurs. Once L becomes negative, load reversal takes place and the projection centre α_{in} is updated to be the current stress ratio.

The plastic modulus H can then be defined based on the mapping rule and Eq. (2.8):

$$H = \frac{2}{3}hg(\bar{\theta})G \exp(-n^p\Psi) \left(\frac{M \exp(-n^b\Psi)}{M_m} \left(\frac{\bar{\rho}}{\rho} \right) - 1 \right) \quad (2.29)$$

where the factor $\frac{2}{3}$ is for the equation to be compatible with that in triaxial stress space, $\bar{\rho}$ is the distance between $\bar{\mathbf{r}}$ and α_{in} , and ρ the distance between \mathbf{r} and α_{in} .

The mapping rule for reversible dilatancy is defined so that the projection of the current stress ratio on the reversible dilatancy surface \mathbf{r}_d is the intersection between $\bar{\mathbf{r}}$ and the reversible dilatancy surface:

$$\mathbf{r}_d = \frac{M_d}{M_m} \bar{\mathbf{r}} = \frac{M \exp(n^d \Psi)}{M_m} \bar{\mathbf{r}} \quad (2.30)$$

The generation and release of reversible dilatancy can then be judged by the angle between $\mathbf{r}_d - \mathbf{r}$ and \mathbf{n} :

$$D_{re} = \frac{\dot{\epsilon}_{vd, re}}{\dot{\gamma}^p} = \begin{cases} D_{re, gen}, & (\mathbf{r}_d - \mathbf{r}) : \mathbf{n} < 0 \\ D_{re, rel}, & (\mathbf{r}_d - \mathbf{r}) : \mathbf{n} > 0 \end{cases} \quad (2.31)$$

While the release rate still follows the triaxial formulation Eq. (2.11), the generation rate of reversible dilatancy now becomes:

$$D_{re, gen} = \sqrt{\frac{2}{3}} d_{re, 1} (\mathbf{r}_d - \mathbf{r}) : \mathbf{n} \quad (2.32)$$

$\sqrt{\frac{2}{3}}$ is introduced for consistency with the formulation in triaxial stress space.

Irreversible dilatancy rate D_{ir} defined in the triaxial formulation by Eq. (2.13) is still valid in the multiaxial formulation. The generation of post-liquefaction shear deformation also follows the description in the triaxial stress space formulation.

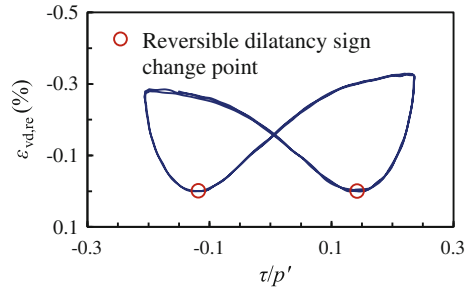
2.3 Determination of Model Parameters

Table 3.1 lists the 14 parameters used in the model. Some parameters used in this model have been documented by previous researchers, including the elastic modulus constants (G_0 , κ) (Zhang and Wang 2012; Richart et al. 1970), plastic modulus parameter (h) (Wang et al. 1990) and critical state parameters (M , λ_c , e_0 , ξ) (Li and Dafalias 2000), the calibration methods suggested for these parameters in the respective studies can be adopted.

The state parameter constants n^p and n^d can be determined through $n^p = \ln(M/\eta_p)/\Psi_p$ and $n^d = \ln(M_d/M)/\Psi_d$ derived from Eqs. (2.8) and (2.10), where η_p and Ψ_p are η and Ψ at peak stress ratio in a monotonic drained triaxial test, and M_d and Ψ_d are those at reversible dilatancy sign change points.

It is important to note here that the determination method of n^d is different to that suggested by Li and Dafalias (2000) due to the way dilatancy is defined in this dissertation. Drained cyclic torsional or triaxial tests should be used for the determination of n^d here, as M_d can only be acquired once irreversible dilatancy is negligible after a number of loading cycles. For example, Fig. 2.3 shows the stress ratio and reversible dilatancy component relations after 18 cycles of a drained cyclic

Fig. 2.3 Stress ratio and reversible dilatancy component relations after 18 cycles of a drained cyclic torsional test for Toyoura sand (data from Shamoto and Zhang 1997)



torsional test for Toyoura sand. At this stage, irreversible dilatancy becomes negligible, and M_d can be determined from the figure to be 0.222. Using the critical state parameters for Toyoura sand given by Li and Wang (1998), the state parameter Ψ_d at this state is -0.232 , thus yielding a n^d of 7.8 for Toyoura sand.

The reversible dilatancy parameters $d_{re,1}$ can be determined using the relationship between η and $\frac{d\epsilon_{vd}}{d\gamma^p}$ from drained cyclic tests as suggested by Zhang and Wang (2012), and $d_{re,2}$ should then be chosen to ensure the release of reversible dilatancy.

For the irreversible dilatancy parameters (d_{ir} and α especially, γ_{dr} can generally be set at 0.05), a trial-and-error process should be adopted to simulate the stress strain behaviour of undrained cyclic torsional/triaxial tests of different initial confining pressure or shear stress amplitude, as was described by Zhang and Wang (2012). The parameter d_{ir} mainly determines how fast liquefaction is reached in undrained cyclic tests, and α controls the decrease rate of irreversible dilatancy.

2.4 Model Implementation

The constitutive model is implemented into the open source finite element framework OpenSees (McKenna and Fenves 2001) using a cutting plane algorithm (Simo and Ortiz 1985) with substepping for the stress integration scheme. Solid-fluid coupled elements needed for the undrained and partially drained analysis of sand, which is essential for liquefaction analysis, are already incorporated into OpenSees [e.g. u-p elements by Yang et al. (2008) and SSP u-p elements by McGann et al. (2012)].

2.4.1 Numerical Treatment for Zero Effective Stress State

In the implementation of the model, to avoid numerical difficulties at zero effective stress during liquefaction, a p_{\min} is set as the minimum effective confining pressure, thus for p to be:

$$\begin{cases} \dot{p} = K \dot{\varepsilon}_v^e, & \varepsilon_{vc} > \varepsilon_{vc,0} \\ p = p_{\min}, & \varepsilon_{vc} \leq \varepsilon_{vc,0} \end{cases} \quad (2.33)$$

The threshold mean effective stress change induced volumetric strain then becomes:

$$\varepsilon_{vc,0} = -\frac{2\kappa}{1+e} \left(\left(\frac{p}{p_a} \right)^{\frac{1}{2}} - \left(\frac{p_{\min}}{p_a} \right)^{\frac{1}{2}} \right) \quad (2.34)$$

The effectiveness of this approach has been validated by Zhang and Wang (2012).

2.4.2 Stress Integration Scheme

The cutting-plane algorithm was chosen for its simplicity and efficiency, being a semi-explicit integration scheme, relatively small time increments are needed for stability. To increase stability, a substepping technique is proposed.

At the beginning of each step, the strain increment from the global converged state is used to calculate an elastic prediction of stress increment, note once again $\varepsilon_{vc} = \varepsilon_v^e$ and p is expressed as a function of ε_{vc} :

$$(\varepsilon_{vc})_{n+1}^{trial} = (\varepsilon_{vc})_n + (\Delta\varepsilon_v)_{n+1} \quad (2.35)$$

$$p_{n+1}^{trial} = g((\varepsilon_{vc})_{n+1}^{trial}) = \begin{cases} p_a \left(\frac{p_m}{p_a} \right)^{\frac{1}{2}} + \frac{1+e_m}{2k} (\varepsilon_{vc})_{n+1}^{trial}{}^2, & (\varepsilon_{vc})_{n+1}^{trial} > \varepsilon_{vc,0} \\ p_{\min}, & (\varepsilon_{vc})_{n+1}^{trial} \leq \varepsilon_{vc,0} \end{cases} \quad (2.36)$$

$$\mathbf{s}_{n+1}^{trial} = \mathbf{s}_n + 2G_{n+1}^{trial} \Delta \mathbf{e}_{n+1} \quad (2.37)$$

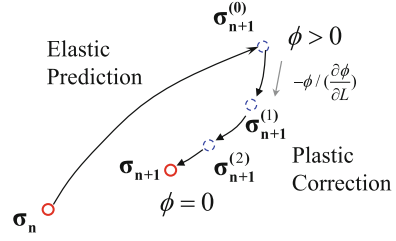
where n is the current step and $n + 1$ the next step. The elastic prediction of stress increment along with the shear strain increment is used to determine the number of sub-steps needed:

$$n_{sub} = \max(\lceil \Delta\gamma_{n+1}/tolerance1 \rceil, \lceil \Delta\eta_{n+1}/tolerance2 \rceil) \quad (2.38)$$

where $\Delta\gamma_{n+1} = \sqrt{\frac{2}{3} \Delta \mathbf{e}_{n+1} : \Delta \mathbf{e}_{n+1}}$, $tolerance1$ and $tolerance2$ are the tolerable shear strain and shear stress invariable increment in each sub-step, $\lceil \cdot \rceil$ is a round up function.

After determining the number of sub-steps, the strain increment at each sub-step is acquired through dividing the strain increment by n_{sub} . The cutting-plane algorithm is then used for the stress integration during each sub-step. Figure 2.4 provides a graphical illustration of the cutting-plane algorithm. The main concept of

Fig. 2.4 Schematic illustration of the cutting plane stress integration algorithm



the cutting plane algorithm is to first make an elastic estimate of the stress increment and then bring the stress back to the solution through plastic correction by enforcing the consistency condition $\phi = 0$ using the first order Taylor series expansion of the consistency condition during each iteration (Fig. 2.4). The main steps of the algorithm are as follows.

1. Initialize the local iteration number k , plastic strain increment and loading index

$$k = 0; \quad (\dot{\epsilon}_v^p)_{n+1}^{(k)} = 0; \quad (\dot{\epsilon}^p)_{n+1}^{(k)} = 0; \quad L = 0; \quad (2.39)$$

2. Elastic prediction of stress state at next step

$$(\epsilon_{vc})_{n+1}^{(k)} = (\epsilon_{vc})_n + (\Delta \epsilon_v)_{n+1} \quad (2.40)$$

$$p_{n+1}^{(k)} = g((\epsilon_{vc})_{n+1}^{(k)}); \quad \mathbf{s}_{n+1}^{(k)} = \mathbf{s}_n + 2G_{n+1}^{(k)} \Delta \mathbf{e}_{n+1} \quad (2.41)$$

3. Check consistency condition to determine whether plastic loading or load reversal occurs

$$\phi^{(k)} = (\mathbf{s}_{n+1}^{(k)} - \mathbf{s}_n) : \mathbf{n}_{n+1}^{(k)} - (p_{n+1}^{(k)} - p_n) \mathbf{r}_n : \mathbf{n}_{n+1}^{(k)} - LH_{n+1}^{(k)} \quad (2.42)$$

If $\phi^{(k)} > 0$, plastic loading is induced, go to step 4; else, load reversal happens and stress-strain relationship at current step is assumed to be elastic, the projection centre is updated, $(\boldsymbol{\alpha}_{in})_{n+1} = \mathbf{r}_n$, go to step 6.

4. Plastic correction through the calculation of loading index increment, as shown in Fig. 2.4

$$\Delta L^{(k)} = -\phi^{(k)} / \left(\frac{\partial \phi}{\partial L} \right)^{(k)} = \frac{\phi^{(k)}}{H_{n+1}^{(k)} + 2G_{n+1}^{(k)} - K_{n+1}^{(k)} D_{n+1}^{(k)} (\mathbf{r}_{n+1}^{(k)} : \mathbf{n}_{n+1}^{(k)})} \quad (2.43)$$

Update loading index and stress-strain state

$$L^{(k+1)} = L^{(k)} + \Delta L^{(k)} \quad (2.44)$$

$$(\Delta \varepsilon_v^p)_{n+1}^{(k+1)} = L^{(k+1)} D_{n+1}^{(k)}; \quad (\Delta \mathbf{e}^p)_{n+1}^{(k+1)} = L^{(k+1)} \mathbf{n}_{n+1}^{(k)} \quad (2.45)$$

$$(\varepsilon_{vc})_{n+1}^{(k+1)} = (\varepsilon_{vc})_n + ((\Delta \varepsilon_v)_{n+1} - (\Delta \varepsilon_v^p)_{n+1}^{(k+1)}) \quad (2.46)$$

$$p_{n+1}^{(k+1)} = g((\varepsilon_{vc})_{n+1}^{(k+1)}); \quad \mathbf{s}_{n+1}^{(k+1)} = \mathbf{s}_n + 2G_{n+1}^{(k+1)} (\Delta \mathbf{e}_{n+1} - (\Delta \mathbf{e}^p)_{n+1}^{(k+1)}) \quad (2.47)$$

5. Check residual of consistency condition for convergence

$$\phi^{(k+1)} = \Delta \mathbf{s}_{n+1}^{(k+1)} : \mathbf{n}_{n+1}^{(k+1)} - \Delta p_{n+1}^{(k+1)} \mathbf{r}_n : \mathbf{n}_{n+1}^{(k+1)} - L_{n+1}^{(k+1)} H_{n+1}^{(k+1)} \quad (2.48)$$

If $|\phi^{(k+1)}| > \textit{tolerance}$, convergence is not reached, $k = k + 1$ and go to step 4; else go to step 6.

6. Update stress, strain and internal variables

$$p_{n+1} = p_{n+1}^{(k+1)}; \quad \mathbf{s}_{n+1} = \mathbf{s}_{n+1}^{(k+1)}; \quad (\varepsilon_{vc})_{n+1} = (\varepsilon_{vc})_{n+1}^{(k+1)} \quad (2.49)$$

As the cutting-plane algorithm is semi-explicit, the continuum tangent operator is used in the solution of the global finite element equations:

$$\boldsymbol{\sigma}_{n+1} = \boldsymbol{\sigma}_n + \mathbf{D}_{ep} : \Delta \boldsymbol{\varepsilon}_{n+1} \quad (2.50)$$

$$\mathbf{D}_{ep} = \mathbf{D}_e - \frac{\mathbf{D}_e : (\mathbf{m} + \frac{D_r + D_{rc}}{3} \mathbf{I}) \otimes (\mathbf{n} - \frac{1}{3}(\mathbf{r} : \mathbf{n})\mathbf{I}) : \mathbf{D}_e}{H + (\mathbf{n} - \frac{1}{3}(\mathbf{r} : \mathbf{n})\mathbf{I}) : \mathbf{D}_e : (\mathbf{m} + \frac{D_r + D_{rc}}{3} \mathbf{I})} \quad (2.51)$$

where \mathbf{D}_e is the elastic tangent operator.

2.4.3 Determination of Projection Point on Maximum Stress Ratio Surface

For the three dimensional implementation of the model, the determination of the projection of the current stress state on the maximum stress ratio surface is needed. As analytically solving β in Eq. (2.27) is of some difficulty, in the implementation β is solved numerically using the Pegasus procedure developed Dowel and Jarratt (1972) guaranteeing fast unconditional convergence, which has been used in the implementation of constitutive models by Sloan et al. (2001) and Andrianopoulos et al. (2010). The main steps of the procedure are as follows.

1. Set $\beta_0 = 0$ and $\beta_1 = 1$ initially
2. Calculate

$$\bar{\mathbf{r}}(\beta_0) = \boldsymbol{\alpha}_{\text{in}} + \beta_0(\mathbf{r} - \boldsymbol{\alpha}_{\text{in}}); \quad \bar{\mathbf{r}}(\beta_1) = \boldsymbol{\alpha}_{\text{in}} + \beta_1(\mathbf{r} - \boldsymbol{\alpha}_{\text{in}}) \quad (2.52)$$

$$f_m(\beta_0) = \eta(\beta_0) - M_m g(\theta(\beta_0)); \quad f_m(\beta_1) = \eta(\beta_1) - M_m g(\theta(\beta_1)) \quad (2.53)$$

3. Judge whether $\bar{\mathbf{r}}(\beta_0)$ and $\bar{\mathbf{r}}(\beta_1)$ are on either side of the maximum stress ratio surface
 If $f_m(\beta_0)f_m(\beta_1) < 0$ and $f_m(\beta_1) > 0$ go to step 4, else if $f_m(\beta_0)f_m(\beta_1) > 0$ and $f_m(\beta_1) < 0$ then set $\beta_0 = \beta_1$ and $\beta_1 = 2\beta_1$ and go to step 2.
4. Calculate

$$\beta = \beta_1 - \frac{f_b(\beta_1)(\beta_1 - \beta_0)}{f_b(\beta_1) - f_b(\beta_0)} \quad (2.54)$$

$$\bar{\mathbf{r}}(\beta) = \boldsymbol{\alpha}_{\text{in}} + \beta(\mathbf{r} - \boldsymbol{\alpha}_{\text{in}}) \quad (2.55)$$

$$f_m(\beta) = \eta(\beta) - M_m g(\theta(\beta)) \quad (2.56)$$

If $|f_m(\beta)| < \textit{tolerance}$, convergence is reached, else go to step 5.

5. Update β_0 and β_1 according to the relative value of $f_m(\beta_0)$, $f_m(\beta_1)$ and $f_m(\beta)$.
 If $f_m(\beta)f_m(\beta_1) < 0$, then $\beta_1 = \beta$ and $f_m(\beta_1) = f_m(\beta)$, then go to step 4; else if $f_m(\beta)f_m(\beta_1) > 0$, then $f_m(\beta_0) = \frac{f_m(\beta_0)f_m(\beta_1)}{f_m(\beta_0) + f_m(\beta_1)}$, $\beta_1 = \beta$ and $f_m(\beta_1) = f_m(\beta)$, go to step 4.

2.4.4 Symmetrisation of the Elastic-Plastic Tangent

As is seen in Eq. (2.51) the tangent operator is not symmetric due to the non-associated flow rule, resulting in an asymmetric system of equations, which is undesirable due to the high computational cost. Various methods that symmetrise non-associated constitutive models have been developed (e.g. Pande and Pietruszczak 1986; Xiong 1986; Luo et al. 2013). In our implementation, the tangent matrix transformation technique developed by Xiong (1986) was adopted, and is expressed as:

$$\mathbf{D}_{\text{ep}} = \mathbf{D}_e - \frac{\mathbf{D}_e : (\mathbf{m} + \frac{D}{3}\mathbf{I}) \otimes (\mathbf{m} + \frac{D}{3}\mathbf{I}) : \mathbf{D}_e}{H + (\mathbf{n} - \frac{1}{3}(\mathbf{r} : \mathbf{n})\mathbf{I}) : \mathbf{D}_e : (\mathbf{m} + \frac{D}{3}\mathbf{I})} \cdot \frac{(\mathbf{n} - \frac{1}{3}(\mathbf{r} : \mathbf{n})\mathbf{I}) : \mathbf{D}_e : \Delta\boldsymbol{\varepsilon}}{(\mathbf{m} + \frac{D}{3}\mathbf{I}) : \mathbf{D}_e : \Delta\boldsymbol{\varepsilon}} \quad (2.57)$$

For the models of piles in liquefiable ground studied in this dissertation, this symmetrisation technique reduces computation time by 35 % on average.

In the OpenSees implementation of the model, an elastic material stage is incorporated into the code to avoid numerical instability in generating the initial stress state, further details of this technique can be found in the OpenSees command manual for the material ‘‘CycLiqCPSP’’ (<http://opensees.berkeley.edu>).

2.5 Validation of Model Formulation and Implementation

The performance of the model is here evaluated by conducting element experiment simulations and simulation of the VELACS centrifuge shaking table tests.

2.5.1 Undrained and Drained Triaxial Experiment Simulation

Triaxial data of undrained and drained loading from Verdugo and Ishihara has been widely used in the evaluation and validation of constitutive models (e.g. Wang et al. 1990; Dafalias and Manzari 2004), as they cover a wide range of confining pressures and initial void ratios. The Toyoura sand used in these experiments had a mean diameter of $D_{50} = 0.17$ mm, maximum and minimum void ratios of 0.977 and 0.597.

The model parameters used in the simulation are provided in Table 2.1. Most parameters for the simulation of Toyoura sand experiments were calculated via previously stated determination methods using experimental data from Zhang (1997) and Zhang et al. (1997) which will be used in the simulations of cyclic torsional tests as well. However, as the Toyoura sand ($D_{50} = 0.18$ mm, $e_{\max} = 0.973$ and $e_{\min} = 0.635$) used by Zhang et al. varied slightly from that used by Verdugo and Ishihara, and more importantly, the experiments by Zhang et al. and those by Verdugo and Ishihara were conducted using different preparation methods, different dilatancy parameters ($d_{re,1}$, and d_{ir}) were used for the simulation of the two respective sets of experiment (Table 2.1). The critical state parameters (M , λ_c , e_0 , ξ) used in the simulations were adopted from the work of Li and Wang (1998) and Li and Dafalias (2000).

Figure 2.5 shows the simulation results of the undrained experiments. With the confining pressure ranging from 0.1 to 3 MPa, and void ratio from 0.907 to 0.735, the model was able to achieve good agreement with experiment data using a single set of model parameters. Thus proving the proposed model to be capable in the simulation of highly dilative and contractive sand behaviour. The unloading processes were also simulated, exhibiting the effectiveness of the reversible and irreversible dilatancy formulations in the model.

Table 2.1 Model parameters for the simulations of element and centrifuge experiments

Sand	G_o	κ	h	M	$d_{re,1}$	$d_{re,2}$	d_{ir}	α	$\gamma_{d,r}$	n^p	n^d	λ_c	e_0	ξ
Toyourea ^a	200	0.008	1.8	1.25	0.6	30	1.4	20	0.05	1.1	7.8	0.019	0.934	0.7
Toyoureb ^b	200	0.008	1.8	1.35	0.35	30	0.75	20	0.05	1.1	7.8	0.019	0.934	0.7
Nevada	225	0.004	1.7	1.35	0.8	30	0.6	10	0.05	1.1	8.0	0.029	0.843	0.7

^aToyourea sand used by Verdugo and Ishihara (1996)

^bToyoureb sand used by Zhang et al. (1997) and Chiaro et al. (2013)

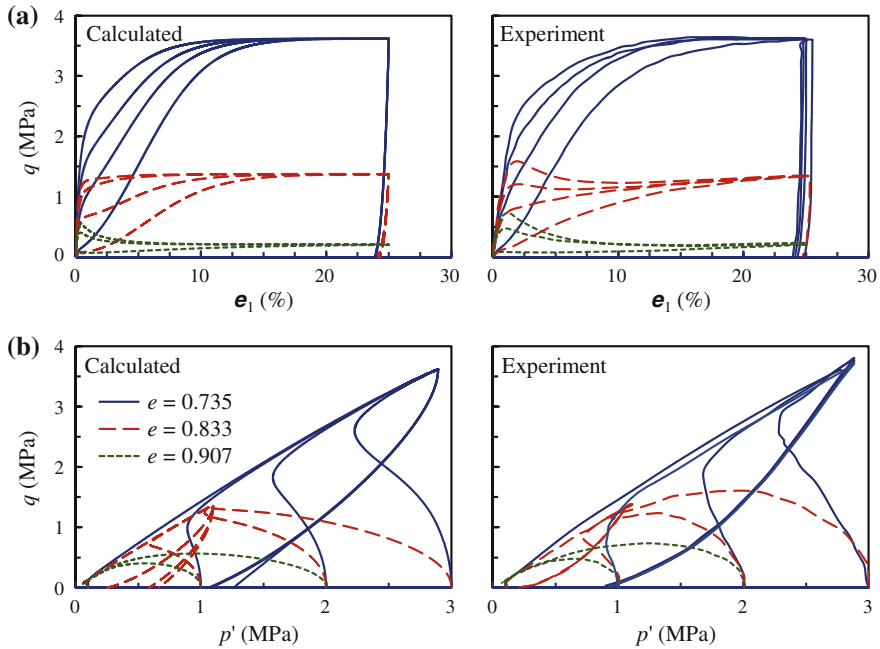


Fig. 2.5 Simulation of undrained triaxial tests on Toyoura sand of different void ratio and initial effective confining pressure (experiment data from Verdugo and Ishihara 1996)

Drained triaxial experiment simulations are presented in Fig. 2.6. Again, the proposed model showed good agreement with experiment data over a range of initial void ratios and confining pressures during both the loading and unloading stages. These simulation results are comparable to those of existing models well known for their simulative capabilities under such stress paths (e.g. Dafalias and Manzari 2004).

2.5.2 Undrained Cyclic Torsional Experiment Simulation

Two undrained hollow cylinder cyclic torsional experiments were simulated using the proposed model to evaluate its capabilities in modelling the cyclic response, and especially the large post-liquefaction shear deformation of sand. The experiments were on Toyoura sand of different densities by Zhang et al. (1997).

The two tests on Toyoura sand were conducted on sand of 60 and 48 % respectively, with the shear stress amplitude for the tests being 25 kPa, and the initial consolidation stress were 100 kPa. The model parameters used are provided in Table 2.1, which were determined as mentioned previously. Figures 2.7 and 2.8 compares the calculated stress path and stress-strain relationship with experiment

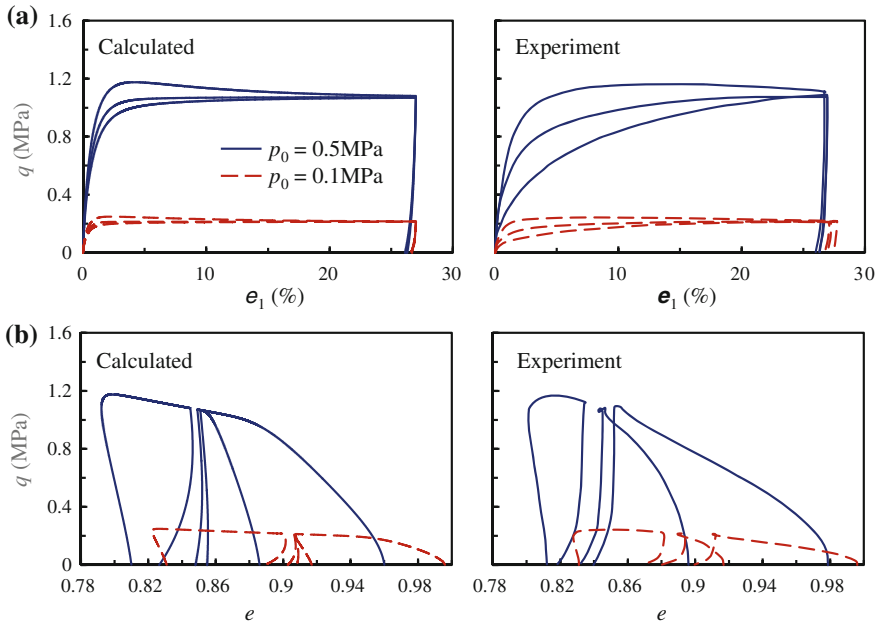


Fig. 2.6 Simulation of drained triaxial tests on Toyoura sand of different void ratio and initial effective confining pressure (experiment data from Verdugo and Ishihara 1996)

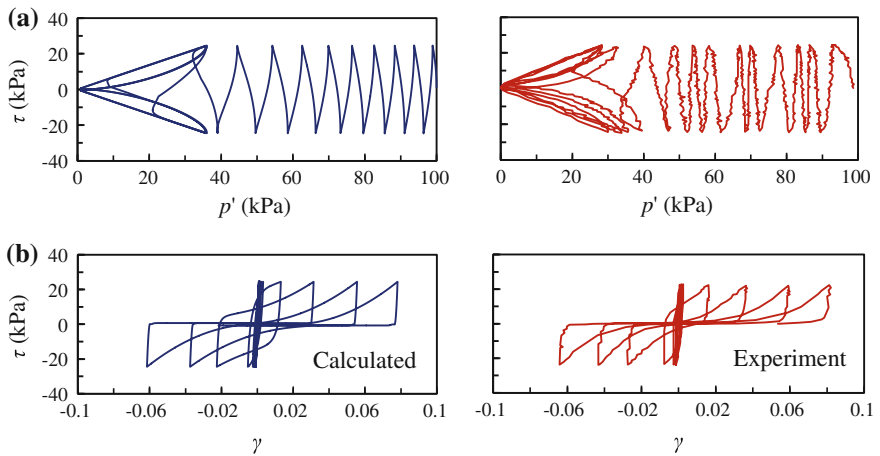


Fig. 2.7 Simulation of undrained cyclic torsional test for Toyoura sand at $Dr = 60\%$ (experiment data from Zhang et al. 1997)

results of Toyoura sand at 60 and 48 % relative density, and shows excellent agreement between them. The model fully captures the features of cyclic mobility of sand during loading and reverse loading. It is worth noting that the generation of shear

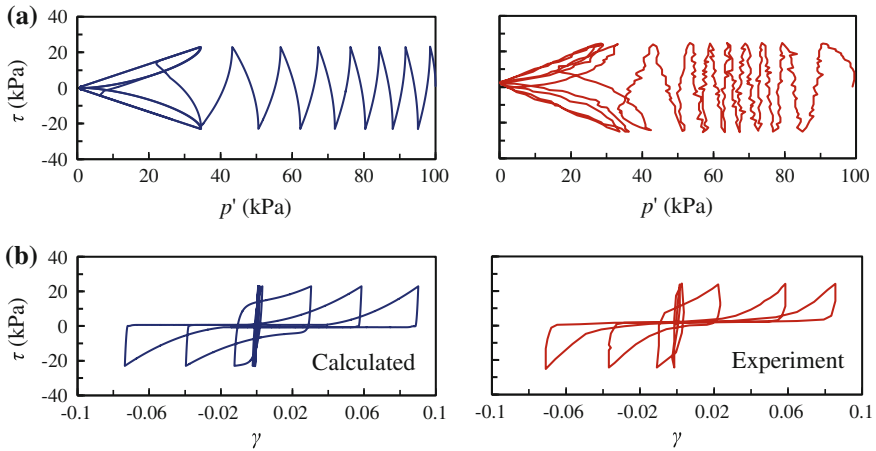


Fig. 2.8 Simulation of undrained cyclic torsional test for Toyoura sand at $D_r = 48\%$ (experiment data from Zhang et al. 1997)

strain at zero effective stress after initial liquefaction and its accumulation with the increasing number of load cycles is very well simulated. This feature is a great advantage of this model over most existing models which either are unable to simulate the accumulation of shear strain at zero effective stress (e.g. Papadimitriou et al. 2001; Dafalias and Manzari 2004) or artificially generate the shear strain at non-liquefaction state (e.g. Elgamal et al. 2002; Boulanger and Ziotopoulou 2013). Again, for the simulation of cyclic tests on Toyoura sand of different densities, the same set of parameters were used due to appropriate incorporation of critical state behaviour.

To display the ability of the model in modelling large shear strains, an undrained cyclic torsional test with a static shear stress bias for Toyoura sand at $D_r = 46.6\%$ conducted by Chiaro et al. (2013) was simulated. The preparation method for the sample used in the test was through air pluviation, which was the same as that of Zhang's experiments, hence the same parameters were used. Figure 2.9 shows the shear strain accumulation reached 32% in both the experiment and simulation. However, for more accurate reflection of such or even higher levels of shear strain, geometric nonlinearity should be taken into consideration for both the constitutive model and the finite element formulation, which is beyond the scope of the current study.

2.5.3 VELACS Centrifuge Experiment Simulation

To validate the performance of the proposed model and numerical algorithm in boundary value problems, the well documented VELACS centrifuge Model No.1 and Model No.2 were simulated and compared against RPI's experiment data (Taboada and Dobry 1993a, b). The basic setup of the centrifuge models are shown

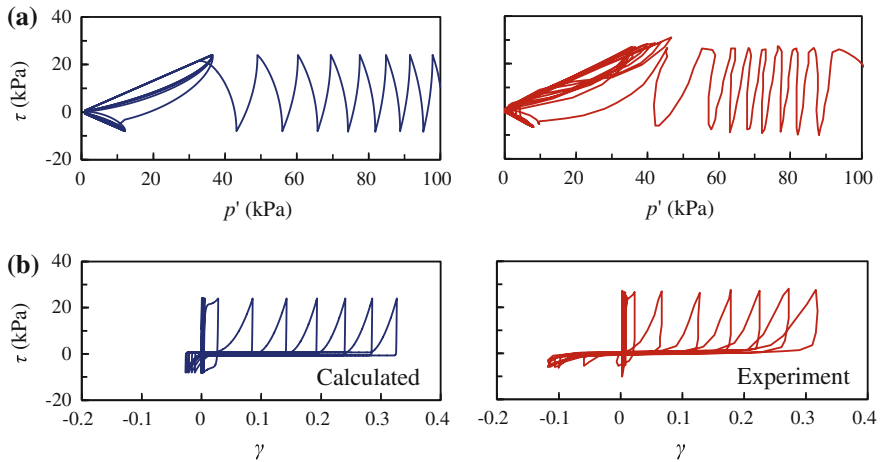


Fig. 2.9 Simulation of undrained cyclic torsional test with a static shear stress bias for Toyoura sand at $Dr = 46.6\%$ (experiment data from Chiaro et al. 2013)

in Fig. 2.10, the two models were almost identical apart from the fact that Model No. 2 had a slight inclination of 2° .

Since the centrifuge experiments were conducted in laminar boxes, they represent the one-dimensional seismic response of a liquefiable soil layer, and thus can be simulated using one single column of elements with properly set boundary conditions. In the simulations presented, three-dimensional Brick UP elements (Yang et al. 2008) with side length of 1.0 m were used to evaluate the performance of the model in 3D analysis. Figure 2.11 shows the finite element mesh, with its boundary conditions. The 4 nodes at the base of the finite element mesh were fixed to follow the input motion, the nodes on each level is then tied together using the Equal DOF command in OpenSees (McKenna and Fenves 2001). Free drainage was set at the top of the model, the rest of the boundary were undrained. For Model No. 2, the direction of gravity was tilted 2° as shown in Fig. 2.11. In the simulations, a gravity loading step was carried out with an elastic material stage and then with a plastic material stage as aforementioned to create the initial geostatic stress field. Ground motion for the two experiments were input at the base of the mesh using the actual input accelerations reported by Taboada and Dobry (1993a, b).

Nevada sand of 45 % relative density ($e = 0.724$) was used in both experiments. The model parameters were estimated based on experiment results (Arulmoli et al. 1992; Kutter et al. 1994), and are shown in Table 2.1. For permeability, an important parameter in the simulation, there has been various values reported for Nevada sand at such relative density, ranging from 1.05×10^{-3} m/s to 3.3×10^{-3} m/s (Bardet et al. 1993; Kutter et al. 1994; Taboada and Dobry 1998; etc.), Manzari and Arulanandan (1993), Andrianopoulos et al. (2010) suggested using time dependent permeability during liquefaction. For simplicity, the permeability k was set to be 1.6×10^{-3} m/s in between the various reported values.

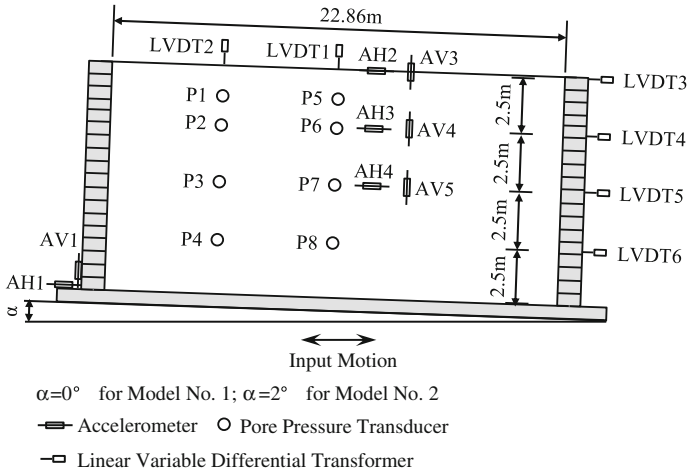


Fig. 2.10 Test configurations of VELACS centrifuge Model No. 1 and Model No. 2

Fig. 2.11 Finite element mesh using coupled 3D Brick UP element for Model No. 1, Model No. 2 and a three dimensional site response analysis

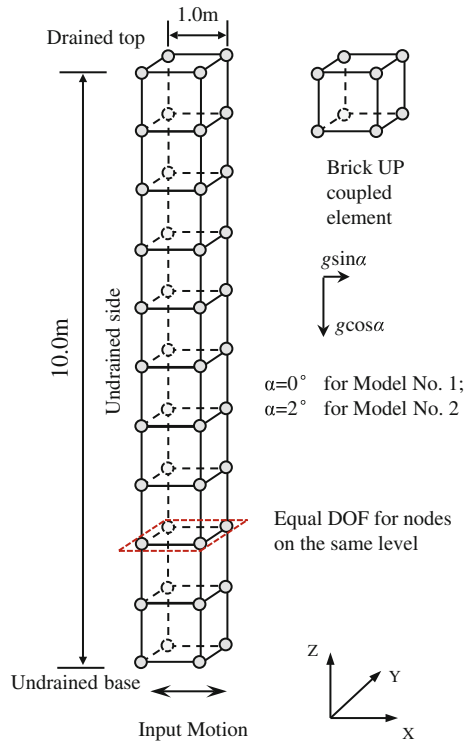
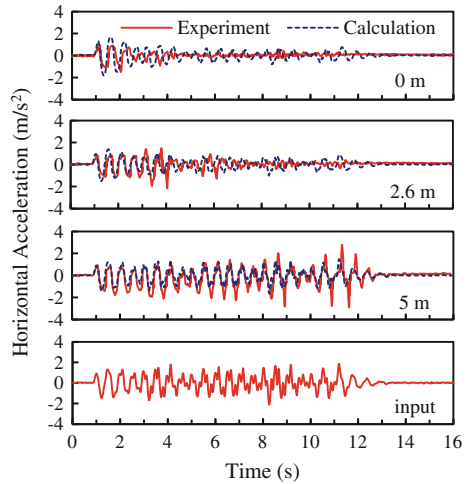


Fig. 2.12 Calculated and measured horizontal acceleration histories in Model No. 1



For the simulation of centrifuge Model No. 1, the calculated ground acceleration at three different depth are compared with recorded data in Fig. 2.12, showing satisfactory agreement. The attenuation of acceleration was notable in both the experiment data and simulation. The amplitude of the simulated lateral displacements were somewhat smaller than the experiment recordings, though final residual lateral displacements matched well (Fig. 2.13). Figure 2.14 shows the excess pore pressure time histories, excellent agreement between experiment and simulation results can be observed for the generation and dissipation process of excess pore pressure. It can be seen that soils above 5 m in depth all reached liquefaction

Fig. 2.13 Calculated and measured horizontal displacement histories in Model No. 1

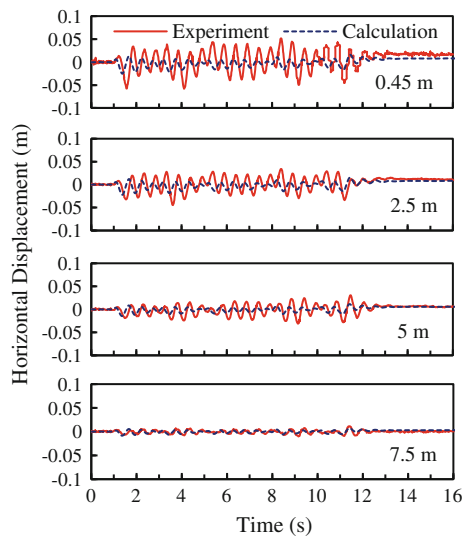
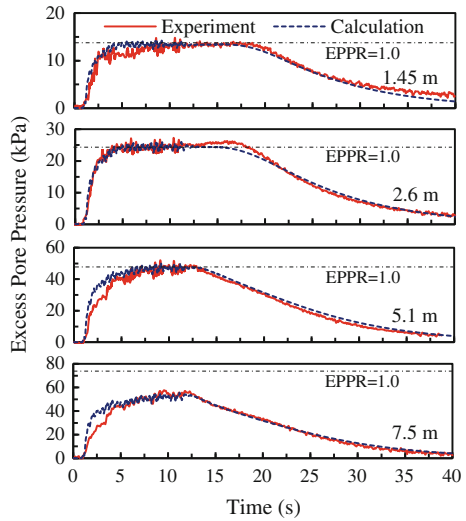


Fig. 2.14 Calculated and measured excess pore pressure histories in Model No. 1



during the seismic event, and the time needed to reach liquefaction was less with smaller depth. Figure 2.15 shows typical stress path and stress-strain relations at two different depths in Model No. 1, showing typical patterns of stiffness degradation during pore pressure build up. From Fig. 2.15, it can be clearly seen that soil reached liquefaction at 2.5 m depth and did not reach liquefaction at 7.5 m.

Figure 2.16 shows that the simulated soil settlement in Model No. 1 is significantly different to that measured in the experiment. In the experiment, settlement developed very quickly, reaching 22 cm after only 20 s, however, the calculated final settlement was only half of that, and reached its final value after 40 s. This discrepancy between simulated settlement and measured settlement in centrifuge tests has been observed in the application of many plasticity models for sand, and

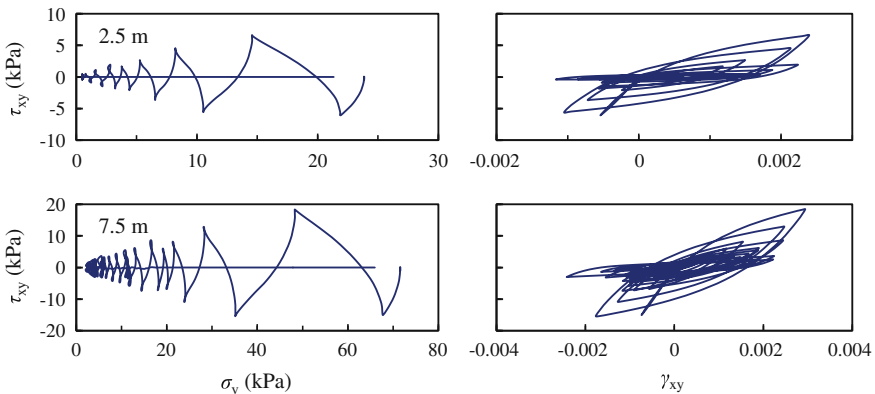


Fig. 2.15 Typical stress path and stress-strain relations at various depths in Model No. 1

Fig. 2.16 Calculated and measured soil settlement in Mode No. 1

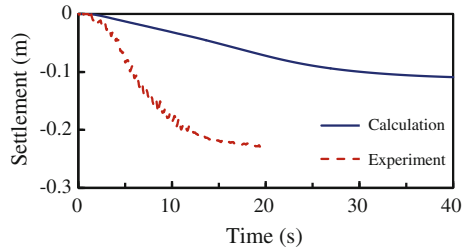
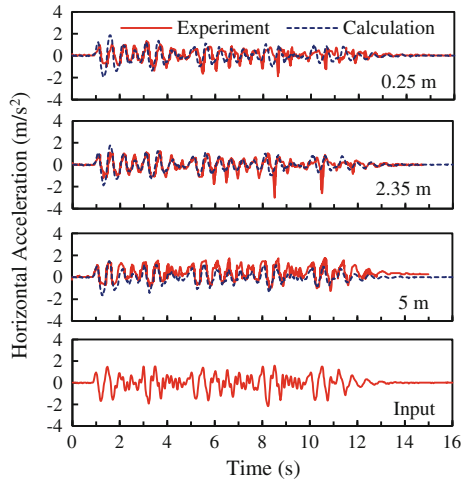


Fig. 2.17 Calculated and measured acceleration histories in Model No. 2



has been an issue of debate: (1) Zhang and Wang (2012) indicated that this difference may be caused by rate effects due to the high velocities in the centrifuge tests; (2) Boulanger and Ziotopoulou (2013) pointed out that the sedimentation process is not reflected in constitutive models; (3) Elgamal et al. (2003) assumes that the underestimation of settlement is due to the high nonlinearity of actual sand; (4) Shahir et al. (2012) tended to suggest that the change in the permeability of sand during liquefaction plays an important role.

In the simulation of Model No. 2, Fig. 2.17 again shows the good agreement for acceleration between experiment and calculation results. The trend and final residual value of the lateral displacements were well simulated (Fig. 2.18). The excess pore pressure time histories are shown in Fig. 2.19, with the patterns of excess pore pressure very closely simulated. The typical stress path and stress-strain relations shown in Fig. 2.20 were different from those of Model No. 1, as the ground inclination caused shear strain to accumulate in one direction, leading to the large lateral deformation in Fig. 2.21. Again, the simulation underestimates the settlement of the sand (Fig. 2.22).

Fig. 2.18 Calculated and measured horizontal displacement histories in Model No. 2

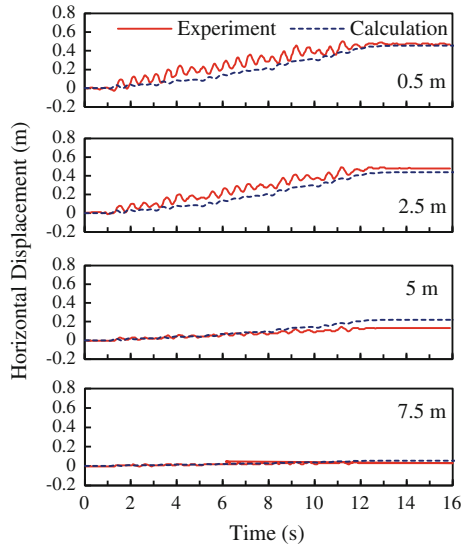
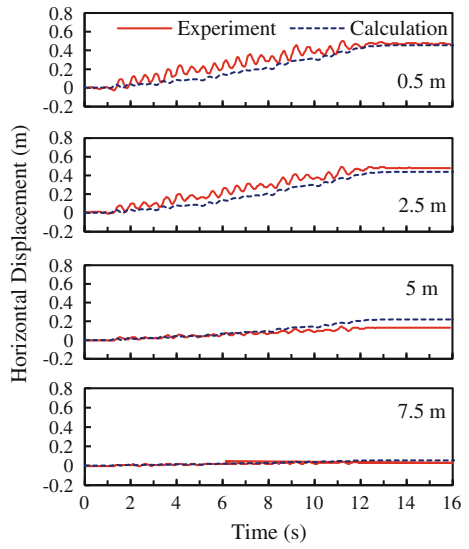


Fig. 2.19 Calculated and measured excess pore pressure histories in Model No. 2



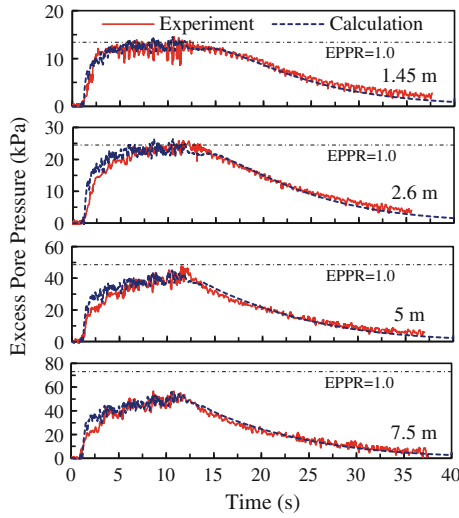


Fig. 2.20 Calculated and measured excess pore pressure histories in Model No. 2

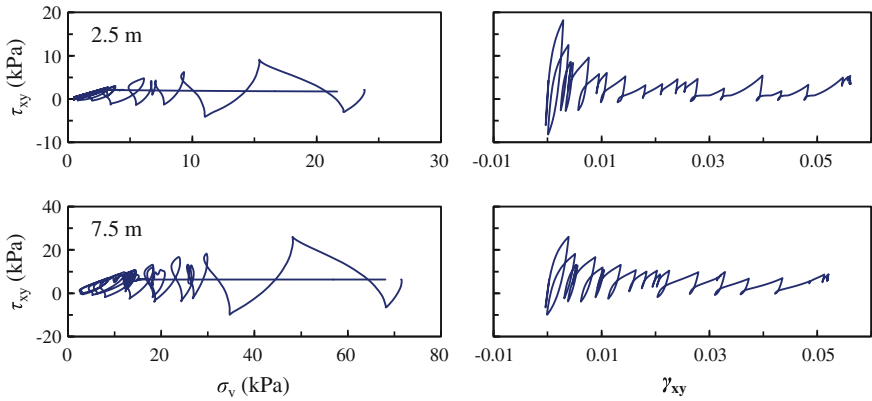
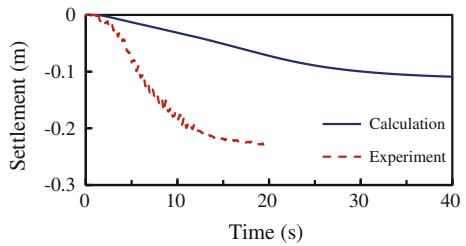


Fig. 2.21 Typical stress path and stress-strain relations in Model No. 2

Fig. 2.22 Calculated and measured soil settlement in Mode No. 2



2.6 Summary

This chapter presents the formulation and numerical implementation of a unified constitutive model for seismic liquefaction analysis based on the physics of post-liquefaction deformation established by Zhang and Wang (2012). The model is unique in that it provides a unified description of sand of different conditions from pre- to post-liquefaction under monotonic and cyclic loading.

By enforcing the volumetric compatibility equation at liquefaction according to Zhang and Wang's (2012) proposition, the model provides physically based computation of the generation and accumulation of shear strain at zero effective stress, which is a significant advantage over most existing models.

Through the appropriate formulation of two dilatancy components, namely reversible and irreversible, the model explicitly links the phenomenon of cyclic mobility to soil dilatancy, providing excellent modelling capabilities for both monotonic and cyclic response of sand.

The state parameter Ψ was incorporated into the model for compatibility with the critical state soil mechanics concept. The model was unified to allow the simulation of sand at different relative densities and confining pressures with a same set of parameters.

In the multiaxial formulation, the mapping rules for plasticity and dilatancy were proposed to be suitable in three dimensional space and accommodate the three dimensional numerical implementation of the model. Calibration methods for the model parameters were also provided.

Using a cutting-plane algorithm with substepping as the stress integration scheme, and the Pegasus procedure to locate the projection of current stress state on the maximum stress ratio surface, the model was implemented in the OpenSees finite element framework, making it openly available to the technical community.

The constitutive model and its three dimensional numerical implementation were validated against drained and undrained triaxial experiments, undrained cyclic torsional experiments and centrifuge experiments, showing the great capabilities of the model in simulating sand response of a wide range of densities and confining pressure, and highlighting its advantage in simulating large post-liquefaction shear deformations.

However, as the current model underestimates the reconsolidation settlement of sand, which is something that could be looked into in future improvements.

References

- Andrianopoulos KI, Papadimitriou AG, Bouckovalas GD. Explicit integration of bounding surface model for the analysis of earthquake soil liquefaction. *Int J Numer Anal Meth Geomech.* 2010;34(15):1586–614.
- Arulmoli K, Muraleetharan KK, Hossain MM, Fruth LS. VELACS: verification of liquefaction analysis by centrifuge studies, Laboratory testing program, Soil Data Report, The Earth Technology Corporation, Project No. 90-0562, Irvine, California; 1992.

- Bardet JP, Huang Q, Chi SW. Numerical predictions for Model No. 1. In: Proceedings, international conference on verification of numerical procedures for the analysis of soil liquefaction problems, vol. 1; 1993. pp. 67–86.
- Been K, Jefferies MG. A state parameter for sands. *Geotechnique*. 1985;35(2):99–112.
- Boulanger RW, Ziotopoulou K. Formulation of a sand plasticity plane-strain model for earthquake engineering applications. *Soil Dyn Earthq Eng*. 2013;53:254–67.
- Chiaro G, Kiyota T, Koseki J. Strain localization characteristics of loose saturated Toyoura sand in undrained cyclic torsional shear tests with initial static shear. *Soils Found*. 2013;53(1):23–34.
- Dafalias YF, Manzari MT. Simple plasticity sand model accounting for fabric change effects. *J Eng Mech*. 2004;130(6):622–34.
- Dafalias YF, Popov EP. A model of nonlinearly hardening materials for complex loading. *Acta Mech*. 1975;21(3):173–92.
- Dowell M, Jarratt P. The, “Pegasus” method for computing the root of an equation. *Bit Numer Math*. 1972;12(4):503–8.
- Elgamal A, Yang Z, Parra E. Computational modeling of cyclic mobility and post-liquefaction site response. *Soil Dyn Earthq Eng*. 2002;22(4):259–71.
- Elgamal A, Yang Z, Parra E, Ragheb A. Modeling of cyclic mobility in saturated cohesionless soils. *Int J Plast*. 2003;19(6):883–905.
- Kutter BL, Chen Y, Shen CK. Triaxial and torsional shear test results for sand. Naval Facilities Engineering Service Center, Contact Report CR 94.003-SHR, Port Hueneme, California; 1994.
- Li XS, Dafalias YF. Dilatancy for cohesionless soils. *Geotechnique*. 2000;50(4):449–60.
- Li XS, Wang Y. Linear representation of steady-state line for sand. *J Geotech Geoenviron Eng*. 1998;124(12):1215–7.
- Ling HI, Yang S. Unified sand model based on the critical state and generalized plasticity. *J Eng Mech*. 2006;132:1380–91.
- Luo T, Qin Z, Feng X, Xia F, Yao Y, Sheng D. A symmetrisation method for non-associated unified hardening model. *Comput Geotech*. 2013;52:38–45.
- Manzari MT, Arulanandan K. Numerical predictions for Model No. 1. In: Proceedings, international conference on verification of numerical procedures for the analysis of soil liquefaction problems, vol. 1; 1993. pp. 179–185.
- McGann CR, Arduino P, Mackenzie-Helnwein P. Stabilized single-point 4-node quadrilateral element for dynamic analysis of fluid saturated porous media. *Acta Geotech*. 2012:1–15.
- McKenna F, Fenves GL. OpenSees Manual. PEER Center. 2001. <http://OpenSees.berkeley.edu>.
- Pande GN, Pietruszczak ST. Symmetric tangential stiffness formulation for non-associated plasticity. *Comput Geotech*. 1986;2(2):89–99.
- Papadimitriou AG, Bouckovalas GD, Dafalias YF. Plasticity model for sand under small and large cyclic strains. *J Geotech Geoenviron Eng*. 2001;127(11):973–83.
- Richart FE Jr, Hall JR, Woods RD. *Vibrations of soils and foundations*. New Jersey: Prentice-Hall Inc; 1970.
- Roscoe KH, Schofield AN, Wroth CP. On the yielding of soils. *Geotechnique*. 1958;8(1):22–53.
- Rowe PW. The stress-dilatancy relation for static equilibrium of an assembly of particles in contact. In: Proceedings of the Royal Society of London. Series a. Mathematical and physical sciences, London, vol. 269(1339); 1962. pp. 500–527.
- Schofield AN, Wroth CP. *Critical state soil mechanics*. London: McGraw-Hill; 1968.
- Shahir H, Pak A, Taiebat M, Jeremic B. Evaluation of variation of permeability in liquefiable soil under earthquake loading. *Comput Geotech*. 2012;40:74–88.
- Shamoto Y, Zhang JM. Mechanism of large post-liquefaction deformation in saturated sands. *Soils Found*. 1997;2(37):71–80.
- Simo JC, Ortiz M. A unified approach to finite deformation elastoplastic analysis based on the use of hyperelastic constitutive equations. *Comput Meth Appl Mech Eng*. 1985;49(2):221–45.
- Sloan SW, Abbo AJ, Sheng D. Refined explicit integration of elastoplastic models with automatic error control. *Eng Comput*. 2001;18(1/2):121–54.

- Taboada VM, Dobry R. Experimental results of Model No. 1 at RPI. In: Proceedings, international conference on verification of numerical procedures for the analysis of soil liquefaction problems, vol. 1; 1993a. pp. 3–17.
- Taboada VM, Dobry R. Experimental results of Model No. 2 at RPI. In: Proceedings, international conference on verification of numerical procedures for the analysis of soil liquefaction problems, vol. 1; 1993b. pp. 277–294.
- Taboada VM, Dobry R. Centrifuge modeling of earthquake-induced lateral spreading in sand. *J Geotech Geoenviron Eng.* 1998;124(12):1195–206.
- Verdugo R, Ishihara K. The steady state of sandy soils. *Soils Found.* 1996;36(2):81–92.
- Wang ZL, Dafalias YF, Shen CK. Bounding surface hypoplasticity model for sand. *J Eng Mech.* 1990;116(5):983–1001.
- Xiong WL. Symmetric formulation of tangential stiffnesses for non-associated plasticity. *Appl Math Mech.* 1986;7(11):1043–52.
- Yang Z, Lu J, Elgamal A. OpenSees soil models and solid-fluid fully coupled elements user manual. University of California, San Diego, California. 2008. http://cyclic.ucsd.edu/opensees/OSManual_UCSD_soil_models_2008.pdf.
- Zhang JM. Cyclic critical stress state theory of sand with its application to geotechnical problems. Ph. D thesis, Tokyo Institute of Technology, Tokyo; 1997.
- Zhang JM, Wang G. Large post-liquefaction deformation of sand, part I: physical mechanism, constitutive description and numerical algorithm. *Acta Geotech.* 2012;7(2):69–113.
- Zhang JM, Shamoto Y, Tokimatsu K. Moving critical and phase-transformation stress state lines of saturated sand during undrained cyclic shear. *Soils Found.* 1997;2(37):51–9.

Chapter 3

Analysis of Seismic Single Pile Response in Liquefiable Ground

The seismic response of single piles in liquefiable ground is investigated in this chapter by conducting centrifuge shaking table tests and numerical simulations. The seismic response of single piles in liquefiable ground is investigated in this chapter by conducting centrifuge shaking table tests and numerical simulations. Typical setups of single piles in liquefiable ground is studied to enhance the understanding of the major influence factors on the behaviour of piles in liquefiable ground, and the dynamic coupling of structure-pile inertial interaction and soil-pile kinematic interaction.

3.1 Centrifuge Test on Single Piles in Liquefiable Ground

Three centrifuge tests on single piles were carried out in this dissertation, (listed in Table 3.1) including one in level ground (denoted LCS), one in slightly inclined ground (by 0.75° , denoted ICS), each of which had a superstructure on top of a pile cap fastened to the pile, and one in level ground without pile cap and superstructure (LNN).

The three centrifuge tests were conducted at 30g centrifugal acceleration at Tsinghua University's 50g-ton geotechnical centrifuge facility. The shaking table used on the centrifuge was designed to generate unidirectional horizontal acceleration with a maximum of 20g, in a frequency range of 10–250 Hz. Figure 3.1 shows the setup of the centrifuge tests.

All laboratory dimensions and measurements reported in the current study have been converted to the prototype scale to facilitate engineering interpretation. The basic scaling factors for dynamic centrifuge modelling (Kutter 1992) are provided in Table 3.2. A laminar box with minimal interlayer friction, with coefficient of friction smaller than 0.01, was used in the tests in order to model one-dimensional ground response. The length-to-depth ratio of the laminar box was 2 to ensure

Table 3.1 Centrifuge test and numerical simulation program

ID	Ground inclination	Remarks ^a
LCS ^b	Level	C, S
ICS ^c	0.75°	C, S
LNN	Level	C, S
LNS ^d	Level	S

^aC and S stand for centrifuge test and finite element simulation, respectively

^bThe LCS setup with models different in structure mass, soil stiffness and soil profile are studied through numerical simulations

^cThe ICS setup with models different in ground inclination and soil profile are studied through numerical simulations

^dThe LNS setup with models different in structure mass, soil stiffness and soil profile are studied through numerical simulations

Fig. 3.1 Diagram of centrifuge model tests for single piles in liquefiable ground (dimensions in cm)

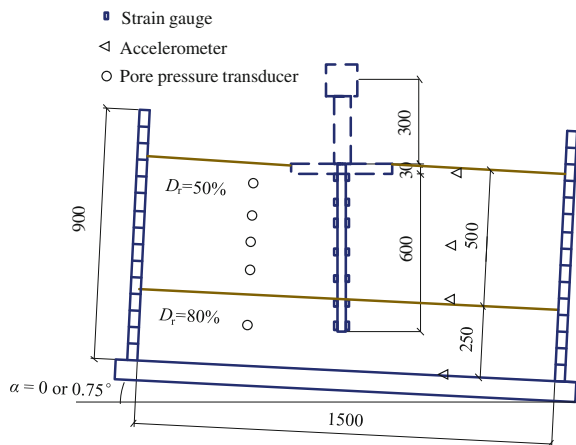


Table 3.2 Centrifuge shaking table test scale factors

Quantity	Symbol	Scale factor
Length	l	$1/n$
Density	ρ	1
Acceleration	a	n
Time (dynamic)	t_d	$1/n$
Time (consolidation)	t_c	$1/n^2$

Note n is the centrifugal acceleration in terms of gravity (g) during the test

minimal cantilever deformation (Hushmand et al. 1988). The ground model was made up with saturated Fujian sand and consisted of a top medium dense ($D_r = 50\%$) layer (5 m thick) and a bottom dense ($D_r = 70\%$) layer of 2.5 m. The Fujian sand is massively produced in Pingtan County of Fujian Province, China,

and complies with Standard Sand for Cement Strength Test (GB 178), a national standard of China. The specific gravity of the sand is 2.65; the maximum and minimum void ratios are 0.879 and 0.555, respectively. The coefficient of permeability of the sand is 1.5×10^{-4} m/s at 50 % relative density and 6.0×10^{-5} m/s at 80 %. A hydroxypropyl methyl cellulose (HPMC) solution with dynamic viscosity 30 times that of water at ambient temperature was used to resolve the discrepancy between the scale factor for dynamic time and consolidation time (Table 3.2). The sand was air pluviated to reach the desired density and then saturated with the HPMC solution under vacuum.

A 6 m long aluminium pile with a 0.3×0.3 m square cross section was modelled in all three tests. The pile head was fastened into a 0.3 m thick 2.7×2.7 m aluminium pile cap in the LCS and ICS tests, with a steel superstructure weighing 10.8 ton fixed on the top. Druck™ PDCR81 miniature pore pressure transducers was used for pore pressure measurement; Dytran™ 3035B/BG accelerometers were installed to measure horizontal acceleration; and the strains on the pile was acquired through 7 pairs of strain gauges and the strain values were used to calculate the bending moment. The pore pressure transducers and accelerometers were installed 4 m from the pile on either side along the centre line of the laminar box at various depths.

3.2 3D FEM Method for Simulation of Piles in Liquefiable Ground

A 3D FEM method for simulating the seismic behaviour of piles in liquefiable ground is developed. The unified plasticity model for large post-liquefaction shear deformation of sand, which has been implemented in OpenSees, is used to provide description for sand. OpenSees's u-p brick element is adopted for solid-fluid coupling in the effective stress analysis of saturated sand. The capability of the u-p formulation in capturing dynamic pore pressure was validated by Zienkiewicz et al. (1980, 1999) and is considered appropriate for soils with the coefficient of permeability smaller than 10^{-3} m/s in the complete loading frequency range, and acceptable for loading frequencies greater than 2 Hz when the coefficient of permeability is less than 10^{-1} m/s, which meets the requirements of this study, where the coefficient of permeability is in the range of 10^{-5} to 10^{-4} m/s.

Second order twenty-node brick elements are used for the piles to provide an appropriate physical representation of the soil-pile system. The cross section of a pile consists of a number of elements along the bending direction (Fig. 3.2), intended to fully capture the bending of the pile. The moment on the pile is calculated by summing the product of the average stress on each relevant element ($\sigma_{ave,i}$) with its area (A_i) and moment arm (l_i):

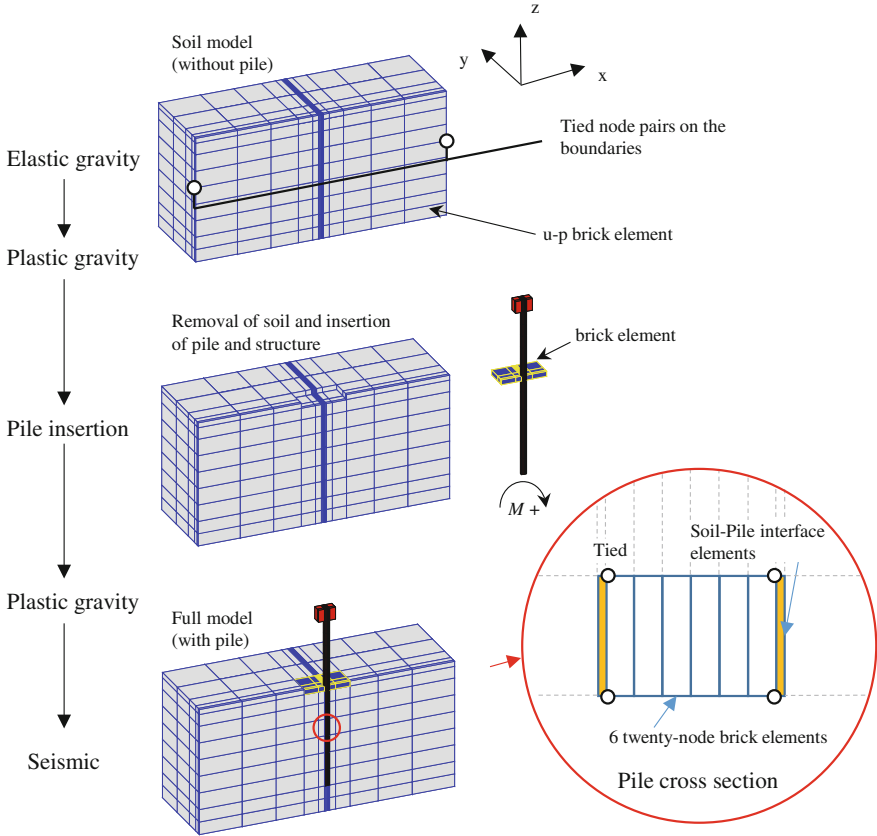


Fig. 3.2 Diagram of staged modelling technique for three dimensional finite element simulation of piles in liquefiable ground

$$M = \sum \sigma_{ave,i} A_i l_i \tag{3.1}$$

To prove that the finite element representation of the pile can accurately capture the bending deformation, we simulate a pile alone as a cantilever bending column in Fig. 3.3. The deflection and bending moments solved by the finite element model with six second-order hexahedron elements along the bending direction show excellent agreement with the corresponding closed-form solutions of Euler beam theory.

A hyperbolic model (Clough and Duncan 1971) is used for the soil-pile interface, in which the shear modulus is determined as:

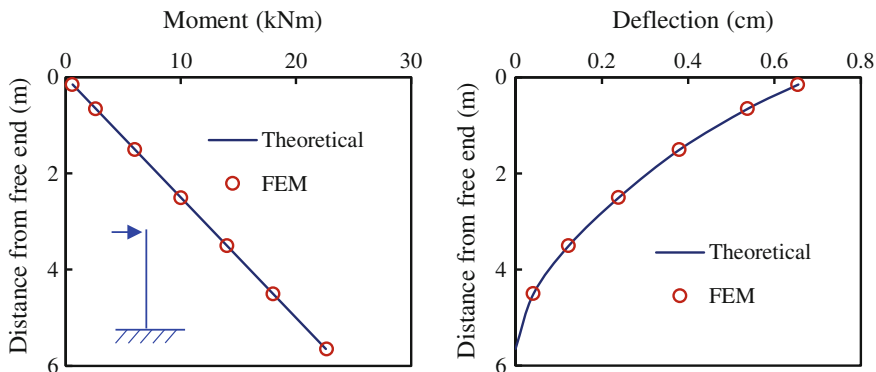


Fig. 3.3 Validation of moment and deflection calculation method using 6 twenty-node brick elements in a cross section

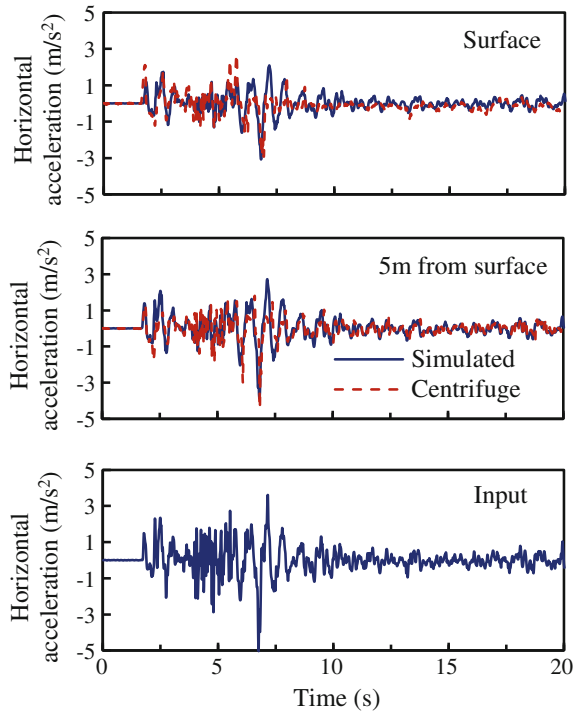
$$G_t = G_{0c} P_a \left(\frac{\sigma_n}{P_a} \right)^n \left(1 - R_f \frac{\tau}{\sigma_n \tan \phi} \right)^2 \quad (3.2)$$

where G_{0c} , n , R_f and ϕ are model parameters, P_a is the atmospheric pressure, and σ_n and τ are the normal and tangential stresses at the interface, respectively. For the simulations in this dissertation, the normal direction of the interface is the direction perpendicular to the associated pile surface.

A staged modelling procedure is adopted to simulate the physical process of pile installation in order to result in correct initial conditions for the subsequent seismic analysis. In the first stage, the soil block without piles is modelled using u-p formulation hexahedron elements with appropriate boundary conditions, and gravity is applied. Figure 3.4 shows the soil model for a level ground. If a sloping ground is to be modelled, the z coordinate of nodes in an original horizontal mesh can be changed to achieve the desired inclination without rotating the entire model. Note that the nodes that are connected with or in the place of the pile and pile cap should not be moved for the sloping models, so that the pile and pile cap to be inserted in the later stage can conveniently remain vertical. A close inspection of the calculated initial effective stress (not shown) found that the vertical stress contour is parallel to the inclined ground surface in the far-field, indicating that the slope condition is well simulated. An elastic gravity stage with consolidation is first carried out, during which linear elasticity is used for the soil. The state of the soil is then updated to comply with the proposed plasticity model, and a plastic gravity stage is then conducted to obtain an initial free-field stress.

Next, we use pile and interface elements to replace the soil elements at the specified location. The three displacement degrees of freedom (DOF) of adjacent nodes on the pile and interface are tied together, while the soil and interface elements have an extra pore pressure DOF. Pile caps and superstructures can also be added to the model if necessary (Fig. 3.2). Another plastic gravity step is subsequently carried out to account for settlement and consolidation caused by pile

Fig. 3.4 Horizontal acceleration histories at various depths from centrifuge test and numerical simulation of model LCS



insertion, generating the proper initial stress field in the soil and piles at a hydrostatic state prior to seismic loading. This procedure does not capture some effects of the pile installation process on soil, such as the stress relaxation for a drilled shaft and soil densification due to driving a high-displacement pile. These effects are expected to only influence the primary process that we focus on in an insignificant way. After the elastic, plastic, and plastic-with-pile gravity stages, the seismic simulation could then be conducted.

Numerical simulation has an important advantage in conducting large amounts of controlled simulations to study the influencing conditions and factors for the response of single piles in liquefiable ground, thus, the influence of soil-pile-structure setup, structure mass, soil stiffness, ground inclination, and soil layering are investigated in this dissertation using the numerical simulation method described. In validation and application of the proposed 3D finite element modelling method for piles in liquefiable ground, a series of numerical simulations are conducted, as summarized in Table 3.1. Apart from the three centrifuge test setups, a fourth scenario of a single pile in level ground with superstructure directly attached without a pile cap (LNS) is simulated numerically for comparison. The superstructure weight in the LNS case is less than the LCS and ICS cases (1.7 ton compared with 10.8 ton in prototype scales).

Table 3.3 Material parameters used in simulations

Fujian sand (CycLiqCPSP)	Value	Interface (Clough-Duncan)	Value
G_o	200	G_{oc}	500
κ	0.006	n	0.52
h	1.7	ϕ	30°
M	1.3	R_f	0.65
$d_{re,1}$	0.45		
$d_{re,2}$	30		
d_{ir}	0.6	Pile and cap (elastic)	Value
α	40	E	70 GPa
$\gamma_{d,r}$	0.05	V	0.33
n^p	1.1		
n^d	8		
λ_c	0.023	Structure column (elastic)	Value
e_0	0.837	E	200 GPa
ξ	0.7	V	0.3

Note n is the centrifugal acceleration in terms of gravity (g) during the test

The 3D finite element simulations are carried out in the prototype length- and time-scale. A half-model cut along the x - z plane through the pile centre is used with proper boundary conditions applied on the symmetry plane to take advantage of the symmetry of the problem. Each node on the negative- x boundary share the same DOF with the corresponding node on the positive- x boundary to simulate the effects of the laminar box. The tied boundary condition (including modified forms) is widely adopted as a reasonable method for simulating centrifuge experiments using shear beam containers (e.g. Elgamal et al. 2002; Andrianopoulos et al. 2010; Chaloulos et al. 2013). Free drainage boundary is applied at the ground surface. Input accelerations are forced on the bottom nodes. The pile is simulated using six rows of second order hexahedron elements along the bending direction (x). As no significant bending occurs along the y direction, only one row of elements are sufficient in that direction.

One set of model parameters for sand, interface, pile and structure is used in all the simulations as listed in Table 3.3. The elastic parameters for the pile and structure are typical values for aluminium and steel. For the sand model, the elastic shear modulus parameter (G_o), plastic modulus parameter (h) and critical state stress ratio (M) are calibrated against drained triaxial test data, and the elastic bulk modulus parameter (κ) was determined via the rebound curves of triaxial consolidation tests. The critical state parameters (λ_c , e_0 , ξ) for Fujian sand reported by Yang and Sze (2011) were used. The dilatancy parameters are back-calculated from the simulation of the LCS centrifuge test and used in the all the other simulations.

3.3 Test and Simulation Results

3.3.1 LCS, Level Ground with Cap and Superstructure

Figures 3.4, 3.5, 3.6, 3.7 and 3.8 shows the calculated and measured horizontal acceleration, excess pore pressure, and bending moment. The results from numerical simulation were in good agreement with those gained from centrifuge test.

Figures 3.4 and 3.5 depict the accelerations in time and frequency domains, respectively. The maximum input acceleration of model LCS was -4.95 m/s^2 , occurring at 6.76 s. Figure 3.6 shows that the excess pore pressure in the soil generated quickly upon the initiation of the seismic excitation, reaching excess pore pressure ratio (r_u , the ratio of excess pore pressure to initial effective stress) of up to 0.6 before 3 s. Excess pore pressure generation slowed down significantly between 3 and 5.5 s, even though the input motion intensified after 4 s. This is attributed to the attenuation of high frequency motion caused by the build-up of excess pore pressure and the corresponding softening of the soil. The input motion between 3 and 5.5 s consisted of much greater high frequency components (Fig. 3.5a), which was mostly filtered by the softened soil (Fig. 3.5b). The acceleration at the ground surface had a maximum of only 60 % that of the input. Centrifuge test results showed the top 4 m of sand had reached liquefaction after 10 s, where $r_u = 1.0$.

The calculated and measured bending moment histories at three different depth are shown in Fig. 3.7. The maximum bending moment in the pile was -58 kN m in the test and -60 kN m in the simulation, both of which occurred 0.2 s later than the time of peak input acceleration. No residual moment existed after the seismic motion had ceased. According to the peak moment distribution along the pile for model LCS in Fig. 3.8, the maximum bending moment was observed at the pile head, while the pile tip was free to rotate and had zero moment.

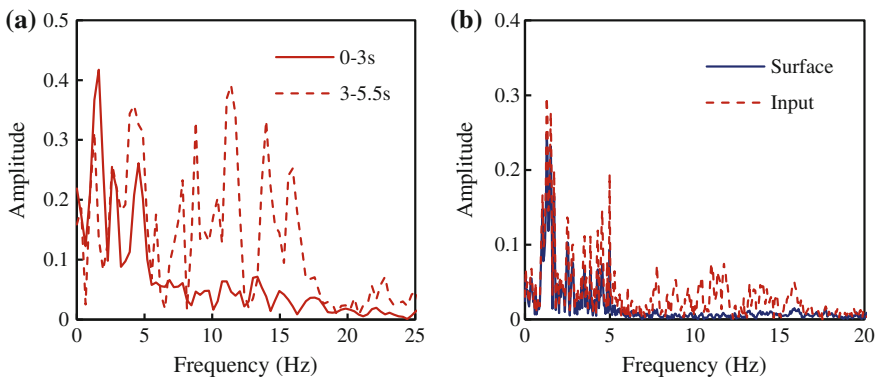


Fig. 3.5 Fourier amplitudes for: (a) input acceleration within two time intervals; (b) surface (simulated result) and input acceleration

Fig. 3.6 Excess pore pressure histories at various depths from centrifuge test and numerical simulation on model LCS

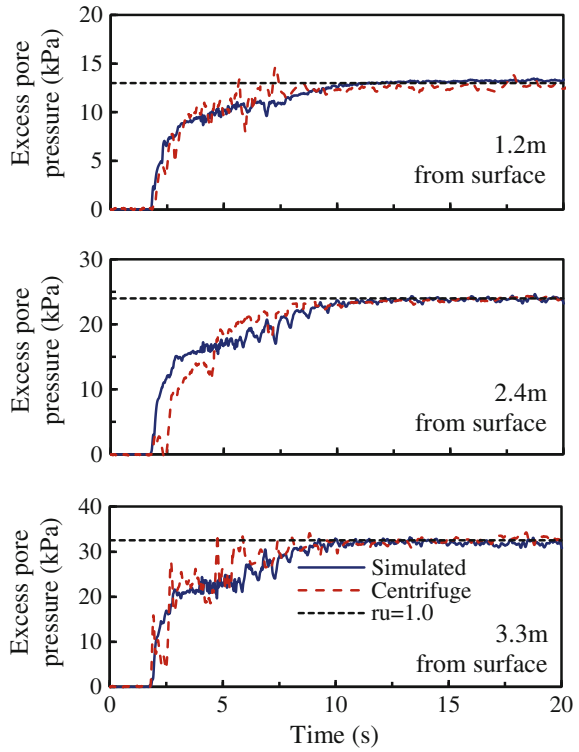


Fig. 3.7 Pile moment histories at various depths from centrifuge test and numerical simulation on model LCS

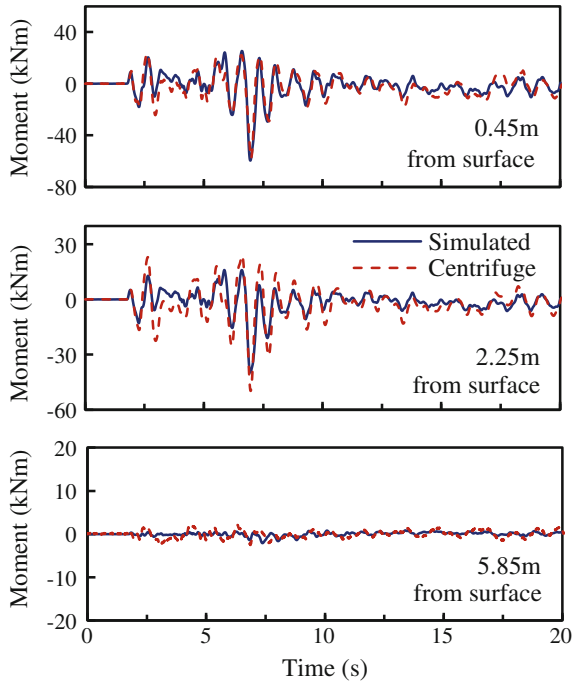
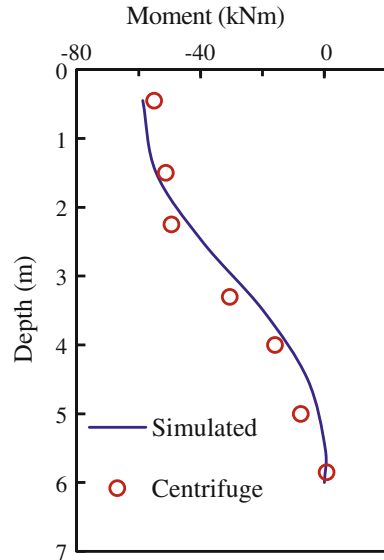


Fig. 3.8 Peak moment distribution along the pile from centrifuge test and numerical simulation on model LCS



3.3.2 ICS, Inclined Ground with Cap and Superstructure

The calculated and measured results for the model with pile cap and superstructure in slightly inclined ground (ICS) are shown in Figs. 3.9, 3.10, 3.11, 3.12 and 3.13. The soil acceleration attenuation (Fig. 3.9), excess pore pressure build-up (Fig. 3.10) and pile bending moment (Figs. 3.12 and 3.13) are accurately simulated using the proposed method, with exactly the same material parameters as those in the LCS simulation. Similar to the observation in the LCS simulation, the near-pile excess pore pressure during shaking in Fig. 3.10b is significantly smaller than that of the far-field measurement at the same depth in Fig. 3.10a, echoing the findings in González et al. (2009). Figure 3.11 provides simulated stress-strain relationship from both far-field and near-pile soil, showing that the far-field sand reached liquefaction and most of the shear strain was generated during lateral spreading. On the other hand, the near-pile sand did not quite reach liquefaction but exhibited larger shear stress amplitudes and much stronger dilatancy tendency, likely owing to the interaction between the pile and soil. The near-pile sand also experienced much smaller shear strain during seismic shaking, which concurs with the photo evidence from centrifuge tests by González et al. (2009).

The peak pile moment during the earthquake was -45 kN m (Fig. 3.12), which was smaller than that of model LCS partly due to the weaker input motion (maximum input acceleration -3.8 m/s^2 of ICS vs. -4.95 m/s^2 of LCS). The peak moment distributions of the inclined and level ground models during shaking were very much alike (Figs. 3.13a and 3.7). However, the ICS model retained a significant amount of residual moment after the earthquake, reaching 20 kN m at the

Fig. 3.9 Horizontal acceleration histories at various depths from centrifuge test and numerical simulation on model ICS

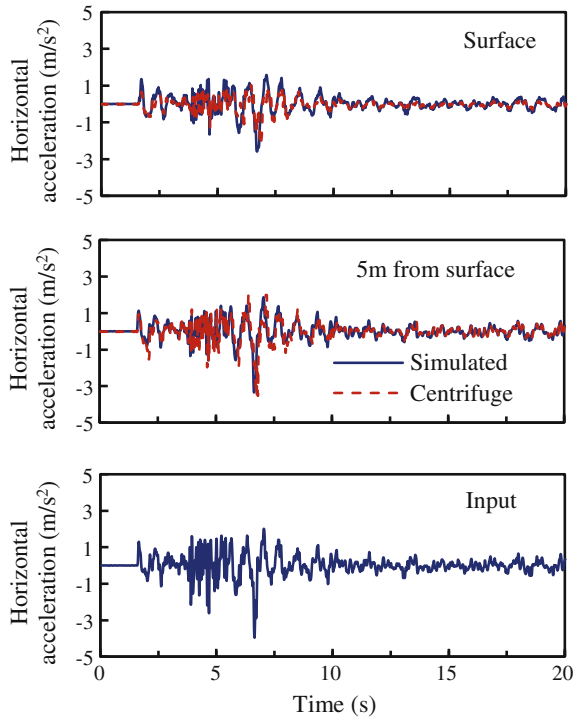
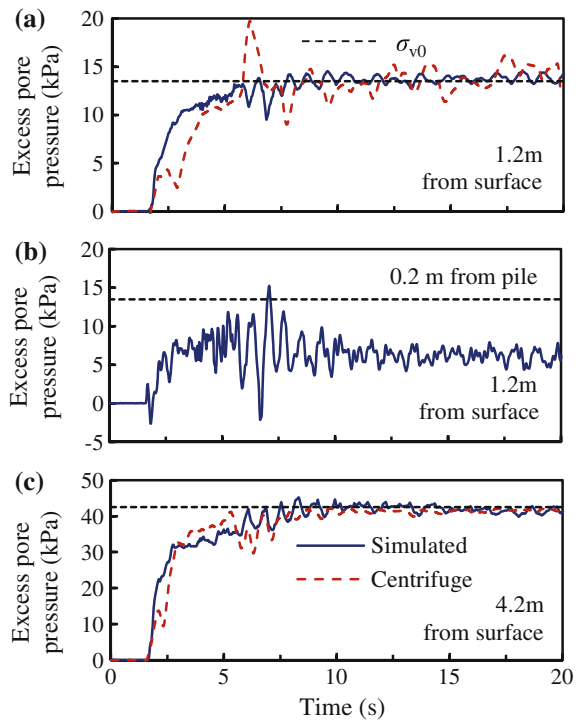


Fig. 3.10 Excess pore pressure histories at various depths and distance from pile in centrifuge test and numerical simulation on model ICS: (a) at 1.2 m from ground surface, 4.0 m from pile; (b) at 1.2 m from ground surface, 0.2 m from pile; (c) at 4.2 m from ground surface, 4.0 m from pile



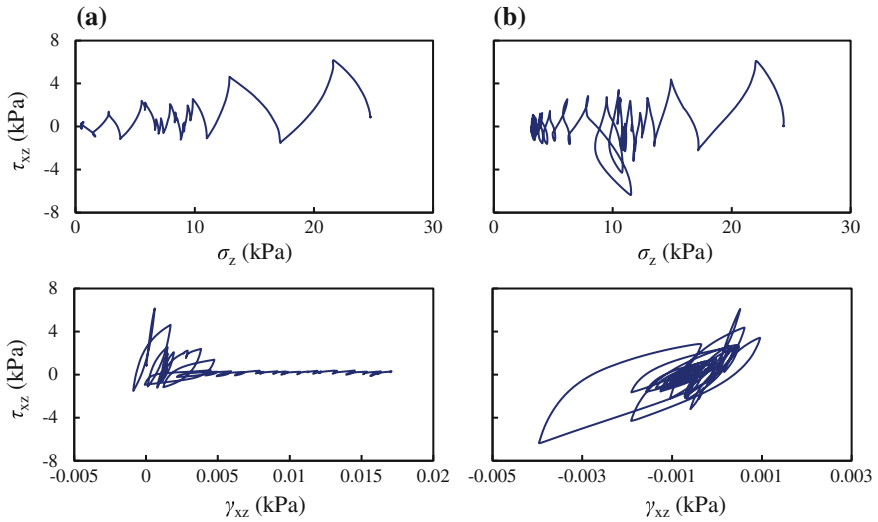
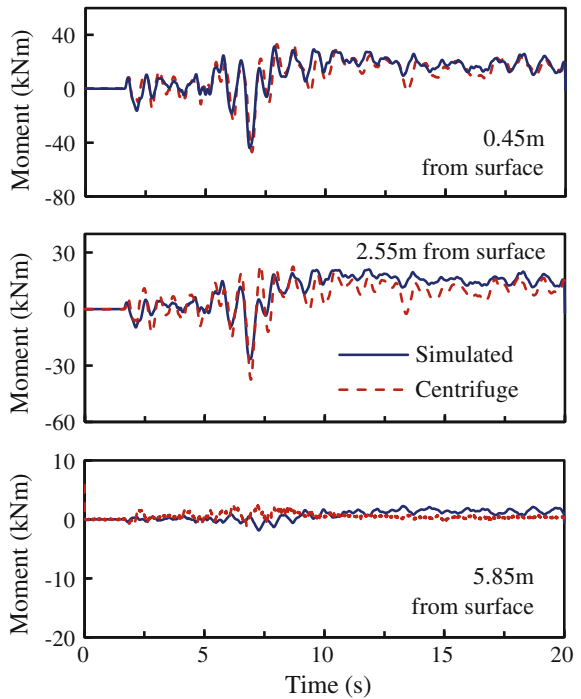


Fig. 3.11 Simulated stress strain relationship 2.6 m from ground surface for model ICS: (a) 4.0 m from pile; (b) 0.2 m from pile

Fig. 3.12 Pile moment histories at various depths from centrifuge test and numerical simulation on model ICS



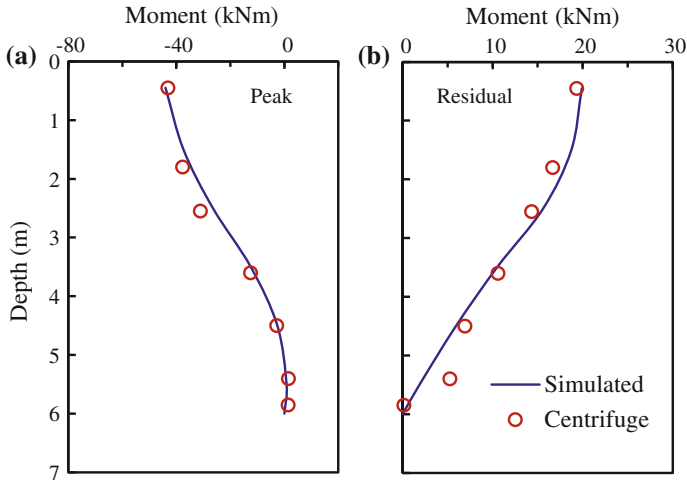


Fig. 3.13 Peak and residual moment distribution along the pile from centrifuge test and numerical simulation on model ICS. **a** Peak. **b** Residual

pile head (Fig. 3.13b). This residual moment was caused by the lateral spreading of the inclined ground after liquefaction, and amounted to nearly half of the peak moment even in the very gently inclined model (0.75°).

3.3.3 LNN and LNS, Level Ground without Cap, without and with Superstructure

The simulated and measured pile moment histories and peak distribution for the model without pile cap and superstructure in level ground (LNN) are shown in Figs. 3.14 and 3.15, respectively. The acceleration and pore pressure results were very similar to those of the LCS model and are not shown for conciseness. Compared with the LCS model with the same ground and seismic conditions, the pile in the LNN model experienced much smaller bending moments with a maximum of only 5 kN m. Since there was no pile cap or superstructure, the bending moment at both the pile head and tip were zero, and the maximum moment occurred at 3–4 m depth.

To comparatively study the influence of the pile cap and superstructure, a model with superstructure but without pile cap (LNS) was simulated numerically. Figure 3.15 compares the peak pile moment of the LNS and LNN models. The inertia of the superstructure caused the peak pile moment to be much larger down to 2 m depth in the LNS model, with a maximum of 21 kN m at the pile head. However, the peak pile moment below 3 m depth were almost identical for the LNS and LNN models, which echoes with Gazetas and Dobry’s (1984) suggestion that the active length of piles under horizontal dynamic loading is 5–15 times the pile diameter. It is worth noting that under the same seismic excitation, the peak bending

Fig. 3.14 Pile moment histories at various depths from centrifuge test and numerical simulation on model LNN

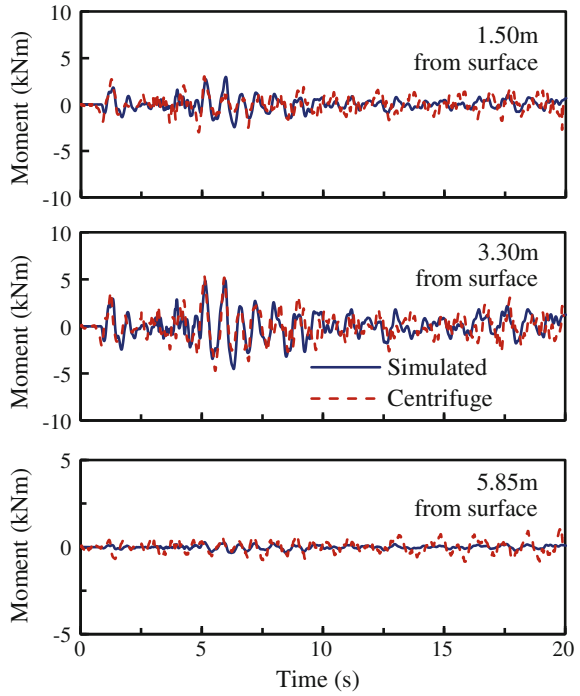
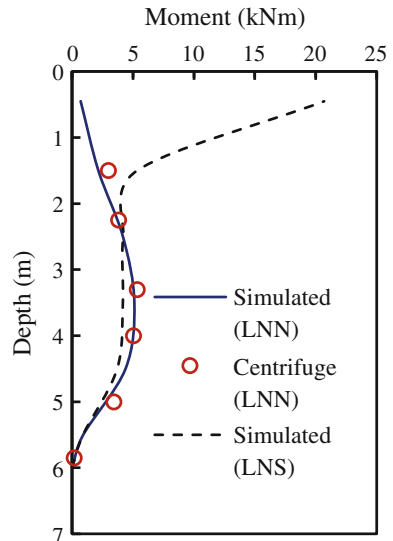


Fig. 3.15 Peak moment distribution along pile from centrifuge test and numerical simulation on models LNN and LNS (numerical simulation only for LNS)



moment for the piles in models LNN and LNS were positive, while that in the LCS model was negative. This difference is due to the different interaction modes caused by the pile cap, which will be discussed in the following section. Note that the pile moment values between LNS and LCS should not be compared directly since different superstructure weights were used.

3.4 Seismic Response of Single Piles in Liquefiable Ground

Through the centrifuge tests and numerical simulations, the seismic response of single piles in liquefiable ground is reproduced. The results from numerical simulations agreed very well with those from the centrifuge tests, validating the proposed 3D FEM method. Based on these validations, more in-depth analysis of single piles in liquefiable ground, can be conducted with confidence using the method, especially on the major influence factors, and the dynamic coupling of structure-pile inertial interaction and soil-pile kinematic interaction.

3.4.1 Major Factors Influencing Pile Responses

3.4.1.1 Pile Cap

Simulation results for models LCS and LNS have shown that under the same ground conditions and seismic input, single piles with and without pile cap experienced peak bending moments of opposite directions. Figure 3.16 shows that pile moment was strongly correlated to the displacement of soil and structure acceleration in both models, with the peak moment occurring at maximum positive surface soil displacement and negative structure acceleration. However, for the case with pile cap (LCS) the moment was negatively correlated to soil displacement and positively correlated to structure acceleration, which was opposite to the case without pile cap (LNS).

This difference in pile moment direction is a result of the difference in bending modes caused by the pile cap. Figure 3.17 shows the pile slope at the time of peak pile moment in model LCS and LNS. The pile slope is defined as $d\omega/dy$, where ω is the pile displacement in the x-direction. Under the same soil displacement and inertial force directions, the pile bent towards opposite directions with and without pile cap. While the slope at pile tip were close for both LCS and LNS cases, the LCS had a very small slope at the pile head making it almost vertical, and the slope at the pile head was greater than that at the pile tip for LNS. This means that the pile cap restricts the rotation of the pile head and thus causes the pile to bend as illustrated in Fig. 3.18a, whereas without the constraint of the cap, the pile would bend in the manner of Fig. 3.18b. The different bending modes hence lead to

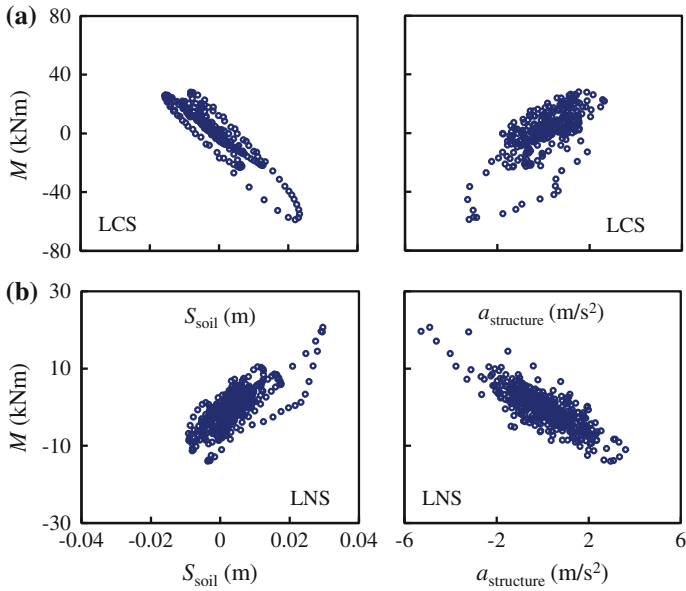
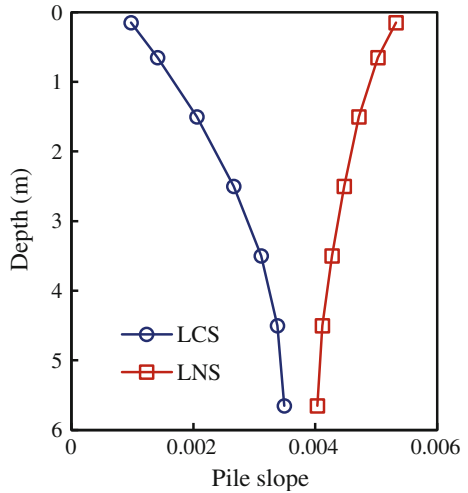


Fig. 3.16 Relationship between surface soil displacement, structure acceleration and pile moment for: (a) LCS and (b) LNS

Fig. 3.17 Pile slope at the time of peak pile moment in model LCS and LNS



different pile moment distributions. Bending modes influence the role of inertial and kinematic interactions in different pile model setups, and should be further investigated in future studies. Variations in pile cap size and modulus are expected to influence the magnitude of the constraint at the pile head and thus influence the response of piles.

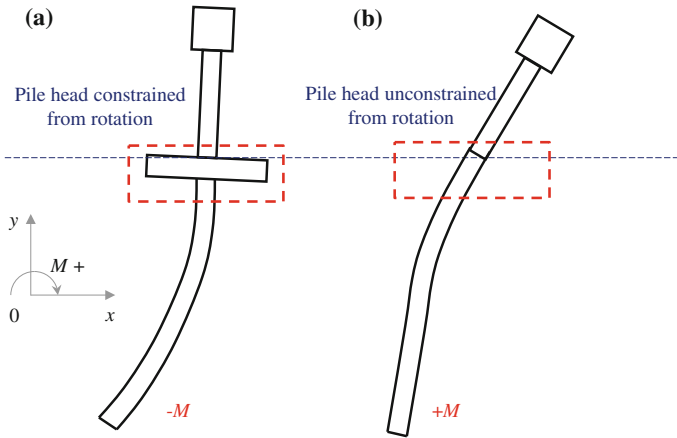


Fig. 3.18 Effect of pile cap on pile head rotation and pile moment

3.4.1.2 Lateral Spreading

Test and simulation results of the ICS model showed that lateral spreading of liquefiable ground could cause significant residual pile moment. Four models with different ground inclinations (1.5° , 2.25° , 3° , and 6°) but otherwise identical to ICS were numerically simulated to study this effect. Figure 3.19 shows the evolutions of the residual maximum pile moment, residual soil surface displacement, residual pile head displacement, and pile-soil relative displacement with respect to the ground inclination angle. As the ground slope increased, both the amount of lateral spreading and residual pile bending moment increased.

The p - y curves at 1.5 m depth in models with 0.75° and 6° inclinations were back-calculated from the simulation results (Fig. 3.20), with the soil resistance obtained by calculating the second order derivative of bending moment with respect to the depth. Comparison of the p - y curves in the two simulations shows that the soil resistance during lateral spreading in the model with more ground inclination is significantly greater and continues to increase with increasing displacement, while the soil resistance was much smaller and peaked early in the model with smaller inclination, similar to the observations by Abdoun et al. in centrifuge test 2° ground inclination (2003). Further investigation into the excess pore pressure time history in the model with 6° inclination shows that sand at 1.5 m depth from ground surface first reached liquefaction, but the excess pore pressure gradually decreased after about 7.5 s (Fig. 3.21), suggesting that near-surface sand had regained effective stress during lateral spreading. The stress strain relationship at the same position further confirms this observation, showing that as the surface sand dilates during lateral spreading, it regains effective stress (Fig. 3.22), which is a very important feature of post-liquefaction shear deformation of sand captured by the current constitutive model.

Fig. 3.19 Effect of ground inclination on residual pile and soil response: (a) residual maximum pile moment; (b) residual soil surface, pile head and pile-soil relative displacement

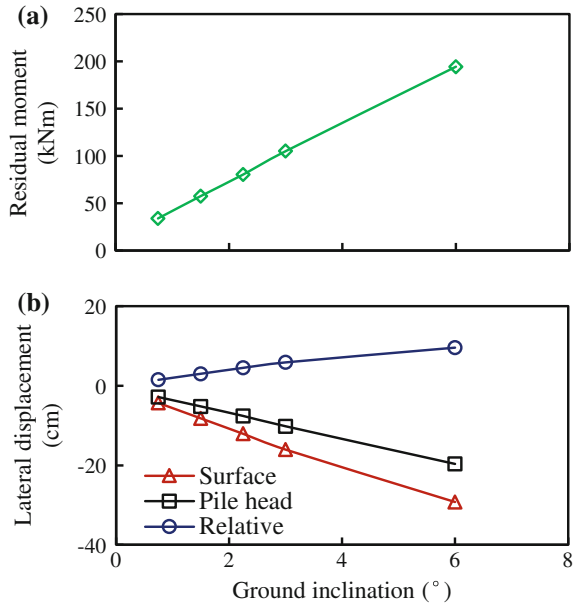


Fig. 3.20 Back calculated soil resistance (p - y) curve in FEM simulation of model ICS with 0.75° and 6° inclination

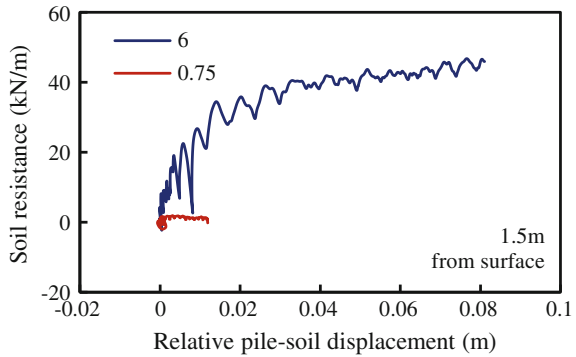


Fig. 3.21 Simulated excess pore pressure time history of model ICS with 6° inclination

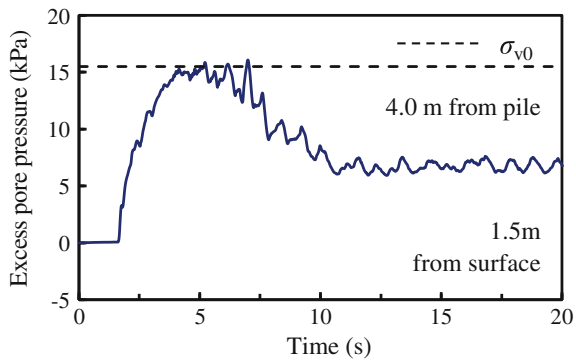
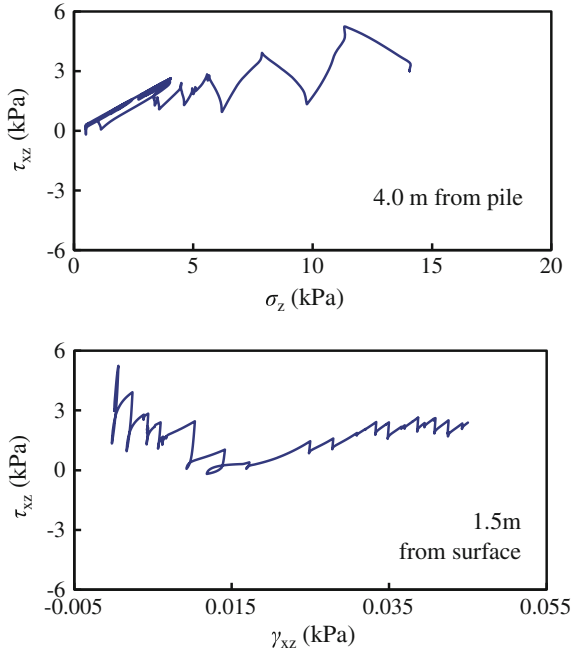


Fig. 3.22 Simulated stress strain relationship 1.5 m from ground surface and 4.0 m from pile for model ICS with 6° inclination



The increase in effective stress, combined with greater relative lateral displacement between pile and soil, causes the residual pile bending moment to increase with increased ground inclination. For the given material and structure, a ground inclination angle above 2° was sufficient to generate a residual moment greater than the peak moment during shaking, which explains the observed pile foundation failures that occurred during lateral spreading, and suggests that current design methods which do not take into consideration of the change in effective stress of sand during lateral spreading may underestimate the forces that are enforced onto the piles.

3.4.1.3 Non-liquefiable Crust

A non-liquefiable crust can often be found above liquefiable soil. The effect of a stiff non-liquefiable crust is here studied by replacing the top 2 m of the LCS and LNS models with a non-liquefiable layer to create models LCS-N and LNS-N. In the current simulations, the crust is modelled using linear elasticity, with a Young’s modulus of 30 MPa and Poisson’s ratio of 0.4, which is aimed to provide a basic understanding of the effect of a relatively stiff non-liquefiable crust, more advanced material model should be used in further in-depth analyses of the influence of the crust layer.

In the LCS-N model, the maximum moment of the pile occurred near the interface between the non-liquefiable and liquefiable layers instead of at the pile head, and was significantly greater than that of the LCS model (Fig. 3.23). The LNS-N showed similar results of maximum moment occurring at the soil layer interface. However, the direction of the moment at the soil layer interface was opposite to that at the pile head (Fig. 3.24), which is again related to the constraint on pile rotation. Figure 3.25 compares the pile slopes at peak pile moment of models LCS-N and LNS-N against their respective counterparts without

Fig. 3.23 Comparison between the peak moment distribution of models LCS-N and LCS

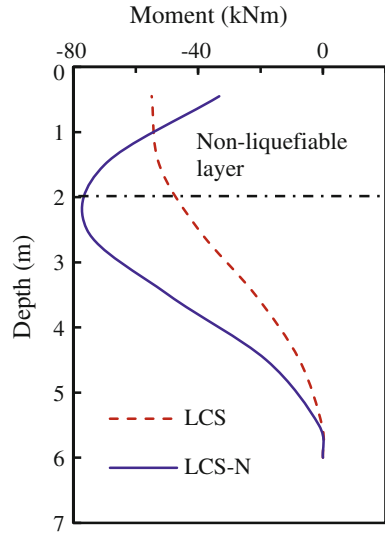


Fig. 3.24 Comparison between the peak moment distribution of models LNS-N and LNS

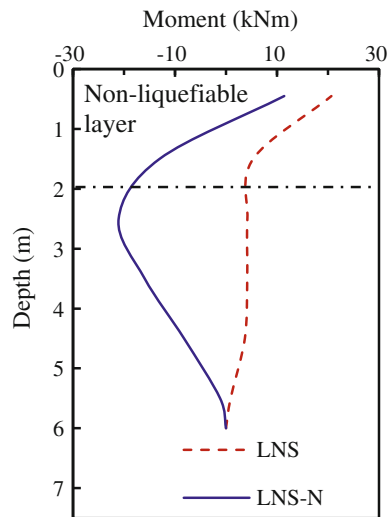
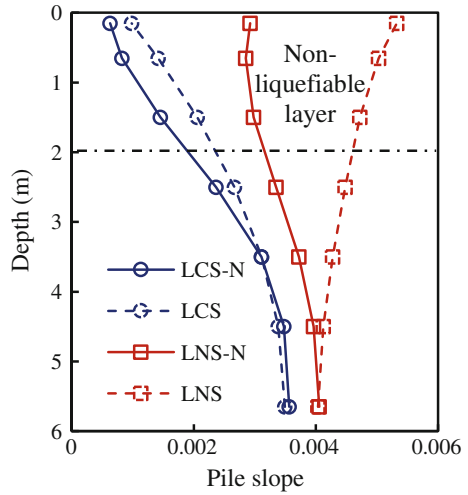


Fig. 3.25 Effect of non-liquefiable crust on pile head rotation



non-liquefiable layers. The comparison shows that the existence of a non-liquefiable crust acts as a weak constraint on the pile rotation within the layer, causing the bending and pile moment to intensify at the interface between non-liquefiable and liquefiable layers, which has been the observation in many case histories (e.g. Berrill and Yasuda 2002; Madabhushi et al. 2010).

3.4.2 Role of Inertial and Kinematic Effects

The typical simulation results in the previous section show that under the same input motion, the single pile with and without pile cap setups experiences peak pile moment demand at almost the same time at the pile head, but of different directions. This raises questions about the roles that structure inertial force and soil kinematic deformation play on the pile bending moment.

3.4.2.1 With Pile Cap

Figure 3.16a plots the pile head moment (maximum moment in the pile) against the structure acceleration and soil surface displacement in model LCS, representing inertial and kinematic interactions, respectively. In this model, the pile head moment is positively correlated with the structure acceleration (i.e. negatively correlated with structure inertial force) and is negatively correlated with the soil surface displacement. The correlation of pile head moment with the soil surface

displacement is stronger than that with the structure acceleration. When the pile head moment is at its peak (negative), the structure acceleration is close to its peak negative value (positive inertial force), while the soil surface displacement is close to its peak positive value. The roles of structure inertial force and soil deformation are looked into through applying a positive lateral force on the structure and

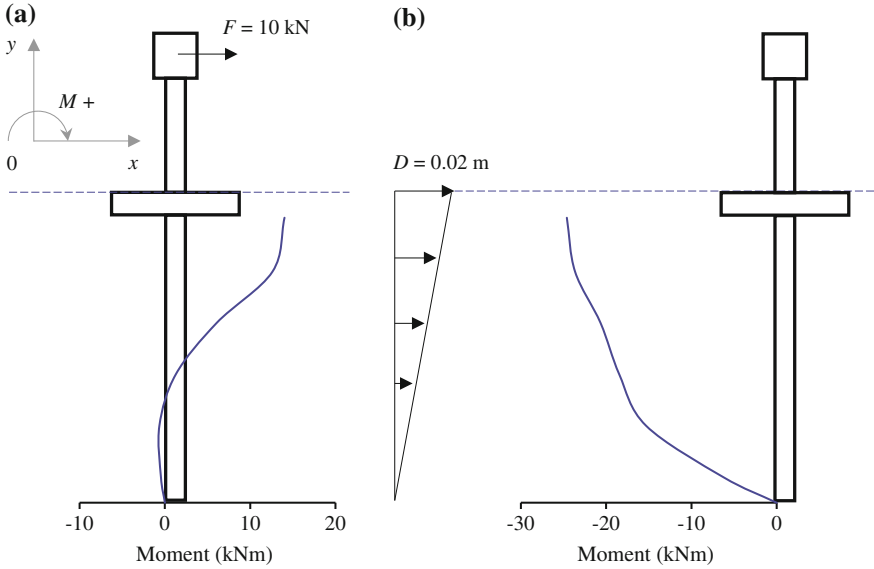
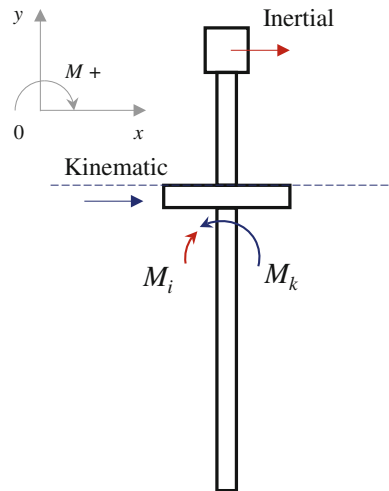


Fig. 3.26 Pile moment caused by (a) applying a static positive lateral force on the structure in model LCS, (b) applying a static positive deformation profile on the soil in model LCS

Fig. 3.27 Illustration of the pile head moment caused by positive kinematic and inertial effects in single pile models with pile cap. M_k is the pile head moment caused by kinematic interaction, and M_i is that caused by inertial force



applying a positive soil lateral displacement profile on the ground separately in two static simulations conducted on the model (Fig. 3.26). Figure 3.26a shows that when a positive lateral force is applied on the structure, the pile head is subjected to a positive bending moment, which is opposite to the trend in Fig. 3.16a. When a positive soil displacement profile is applied on the boundaries of the ground, as shown in Fig. 3.26b, a negative bending moment occurs at the pile head, similar to the pattern in Fig. 3.16a. Comparing the static simulation results in Fig. 3.26 with the dynamic results in Fig. 3.16, it is clear that in this model, the kinematic soil deformation plays a dominating role on the pile moment, while the structure inertial force works against the kinematic effect. Figure 3.27 depicts an illustration of the peak dynamic pile head bending moment demand in the single pile with pile cap setup generated by a combination of positive inertial force and positive kinematic deformation. It should be pointed out that the static simulations can only provide a qualitative understanding of the roles of inertial and kinematic effects, as the soil properties and the combination of the two effects changes during the dynamic simulation.

3.4.2.2 Without Pile Cap

The relationships between the pile head moment and the structure acceleration and soil surface displacement in model $NC_{m2.55G200}$ of the single pile without pile cap setup shown in Fig. 3.16b is opposite to those from the dynamic simulation of the single pile with pile cap setup. In this model, the pile head moment is negatively correlated with the structure acceleration (i.e. positively correlated with structure inertial force) and is positively correlated with the soil surface displacement. The correlation between the pile moment and the structure acceleration is slightly stronger than that between the pile moment and the soil surface displacement. The structure acceleration and soil surface displacement are at maximum negative and positive values, respectively, when the pile head moment is at its positive maximum, which means that under inertial and kinematic effects of the same direction, the single pile without pile cap setup experienced pile head moment of the opposite direction to the setup with pile cap. Similar to the static simulations on the single pile with pile cap setup, a positive lateral force is applied on the structure and a positive soil lateral displacement profile is applied on the soil in two static simulations, respectively. Figure 3.28 shows that a positive pile head moment is generated with positive lateral force on the structure, while the soil displacement profile only generates an insignificant amount of positive pile head moment, with the maximum moment occurring at the middle of the pile. For the single pile without pile cap setup, the inertial effect strongly dominates the pile moment demand at the pile head (Fig. 3.29).

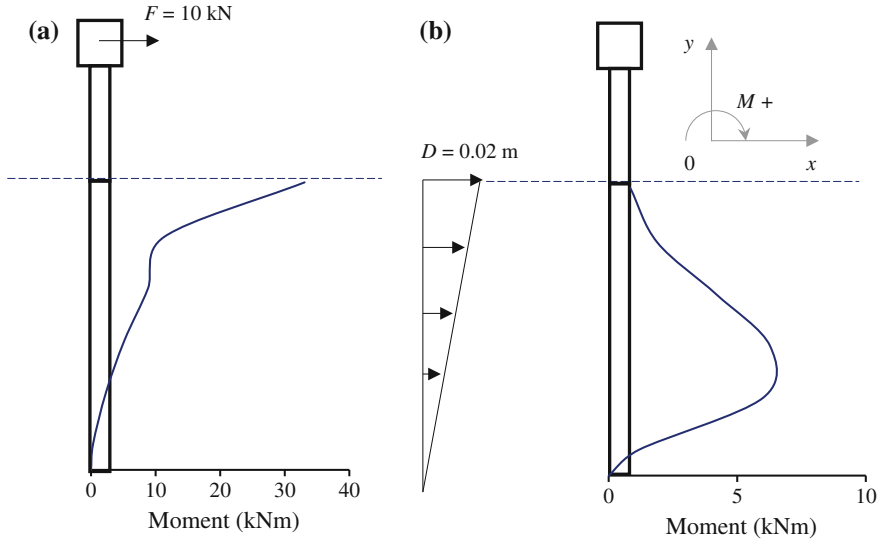
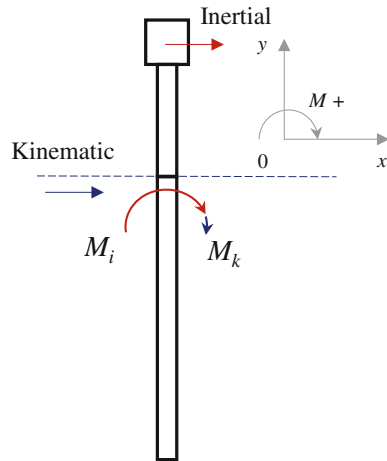


Fig. 3.28 Pile moment caused by (a) applying a static positive lateral force on the structure in model LNS, (b) applying a static positive deformation profile on the soil in model LNS

Fig. 3.29 Illustration of the pile head moment caused by positive kinematic and inertial effects in single pile models without pile cap. M_k is the pile head moment caused by kinematic interaction, and M_i is that caused by inertial force



3.4.3 Coupling of Inertial and Kinematic Effects

Upon acquiring a clear understanding of the roles of inertial and kinematic effects, it is then important to answer the question of how the inertial and kinematic effects combine to generate the dynamic pile bending moment demand in various setups. An important aspect in understanding the seismic inertial and kinematic effects on pile bending moment in liquefiable soils is the coupling of inertial and kinematic

interactions. Cross-correlation analysis between structure acceleration and pile moment, and between soil surface displacement and pile moment time history data can provide a method to quantify the correlation and phase difference between inertial and kinematic interactions. The cross-correlation coefficient of two discrete time series of data f and g can be calculated as (Box and Jenkins 1970):

$$(f * g)[\Delta] \stackrel{\text{def}}{=} \frac{\sum_{t=1}^n f[t]g[t + \Delta]}{\sqrt{(\sum_{t=1}^n f[t]f[t])(\sum_{t=1}^n g[t]g[t])}} \quad (3.3)$$

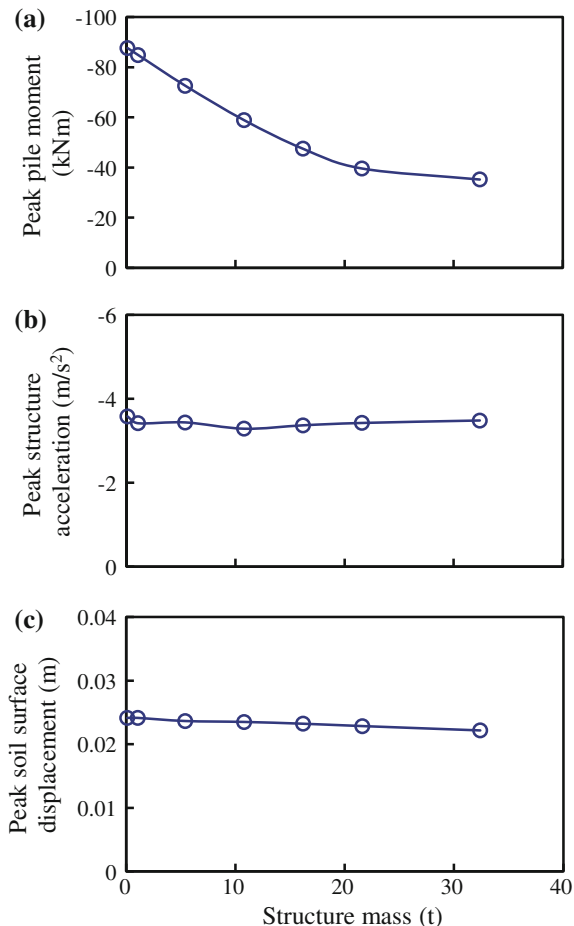
where t is the number of the data point in the series ranging from 1 to n , and Δ is the lag. Equation 3.1 always gives a coefficient value between 1 and -1 inclusive, where 1 represents total positive correlation, 0 is no correlation, and -1 is total negative correlation. When $\Delta = 0$, Eq. 3.1 measures the linear correlation between two original time series. By calculating the cross-correlation coefficient for lag $-(n - 1) \leq \Delta \leq n - 1$, the phase difference or time lag between the two correlated time series can be determined as the lag at which the maximum absolute value of cross-correlation coefficient is obtained.

3.4.3.1 Single Pile with Pile Cap

For the single pile with pile cap setup, Fig. 3.29 shows the influence of structure mass on peak pile moment, structure acceleration, and soil surface displacement based on the results from dynamic simulations on LCS models with different structure mass. These models have exactly the same settings for the soil, pile and pile cap, the mass of the superstructure is changed while its height and natural period remains the same. In this way, the motion of the soil-pile-structure system remains largely unchanged, as indicated by the negligible variations in the results of peak structure acceleration and soil surface displacement among the 7 models with different structure mass shown in Fig. 3.30b, c. The change in the peak pile moment is then almost solely induced by the change in structure mass, and hence peak inertial force. The pile absolute value of peak pile head moment decreases with increasing structure mass (Fig. 3.30a), meaning that an increase in inertial force from the superstructure could actually lead to a decrease in pile demand, which is because the structure inertial force works against the kinematic effect and the pile head moment in this setup. In this series of simulations, when the structure mass changed by 300 times from 0.108 to 32.4 t, the peak pile moment merely reduced by 60 % from -88 kN m to -35 kN. These results show that the inertial effects on pile moment in the single pile with pile cap setup is actually beneficial in terms of reducing pile bending moment demand, but the influence is very limited.

Figure 3.31 depicts the relationships between the pile head moment (maximum moment in the pile) and the structure acceleration, and between the pile head moment and the soil surface displacement in two simulations on LCS models with structure mass of 21.6 and 32.4 t, respectively. Comparing the results for the model

Fig. 3.30 Influence of structure mass on (a) peak pile moment, (b) peak structure acceleration, and (c) peak soil surface displacement in single pile models with pile cap



with a structure weighing 21.6 t in Fig. 3.31a with those for model LCS with structure mass of 10.8 t in Fig. 3.16, it can be seen that when the structure mass increases from 10.8 to 21.6 t, the correlation between inertial force and pile moment becomes stronger, while the correlation between kinematic deformation and pile moment becomes slightly stronger. However, if the mass of the structure further increases to 32.4 t, the correlations between both inertial and kinematic effects and pile moment become less significant (Fig. 3.31b).

Results from cross-correlation analysis between the structure acceleration and the pile moment, and between the soil surface displacement and the pile moment time histories in Fig. 3.32, for LCS models with different structure mass, quantify the observations in Fig. 3.31. At small structure masses, the pile moment has an almost perfect negative correlation with the kinematic soil displacement, with a

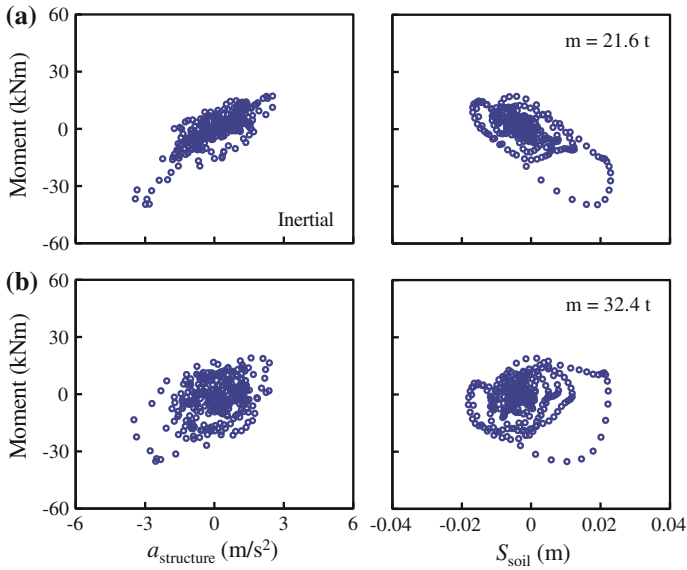
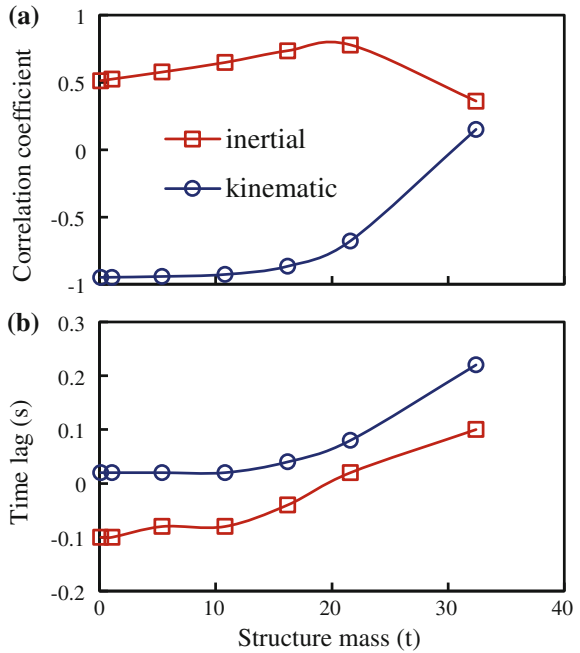


Fig. 3.31 Relationship between structure acceleration and pile head moment (inertial interaction), and between soil surface displacement and pile head moment (kinematic interaction) in models LCS with structure mass of (a) 21.6 t, and (b) 32.4 t

Fig. 3.32 Correlation coefficient and time lag of structure acceleration and pile head moment (inertial interaction), and of soil surface displacement and pile head moment (kinematic interaction) in relationship to structure mass for single pile models with pile cap



correlation coefficient of -0.95 (Fig. 3.32a). This correlation for kinematic interaction becomes less significant as the mass of the structure increases, with the coefficient becoming 0.15 for the model with a 32.4 t structure (Fig. 3.32a). The time lag between soil displacement and pile moment time histories also increases from 0.02 to 0.22 s (Fig. 3.32b). The correlation coefficient between the structure acceleration and the pile moment time histories is only 0.51 for the model with a 0.108 t structure, and increases with increasing structure mass to reach a maximum of 0.78 for the model with a 21.6 t structure, but decreases to 0.36 as the structure mass further increases to 32.4 t. The time lag between the structure acceleration and the pile moment changes from -0.1 to 0.1 s as the structure mass increases.

The influence of kinematic soil deformation on pile bending moment for the single pile with pile cap setup is investigated by altering the soil elastic shear modulus parameter (G_0) value in model LCS (Fig. 3.33). By changing G_0 value from 150 to 300 , the peak soil surface displacement reduces from 3.4 to 1.3 cm (Fig. 3.33c). The 62% decrease in peak soil surface displacement caused the peak

Fig. 3.33 Influence of soil shear modulus parameter G_0 on (a) peak pile moment, (b) peak structure acceleration, and (c) peak soil surface displacement in single pile models with pile cap

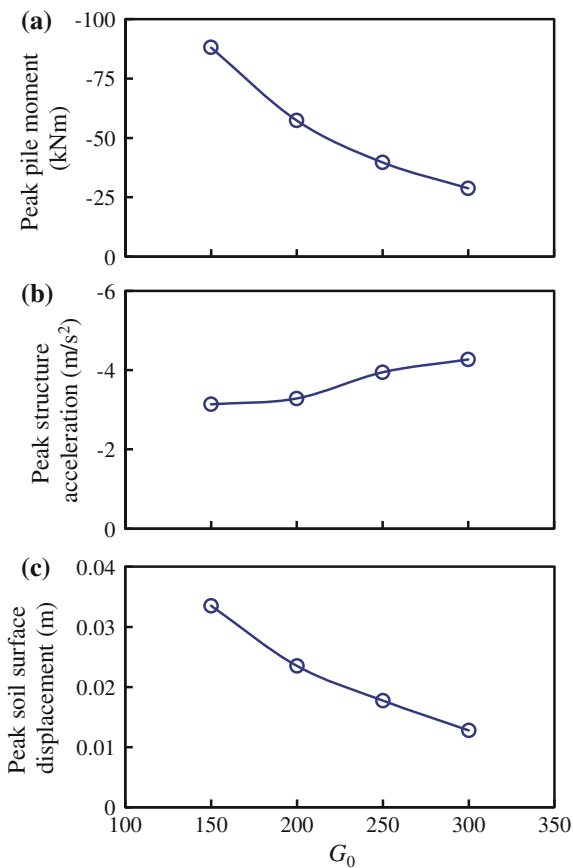
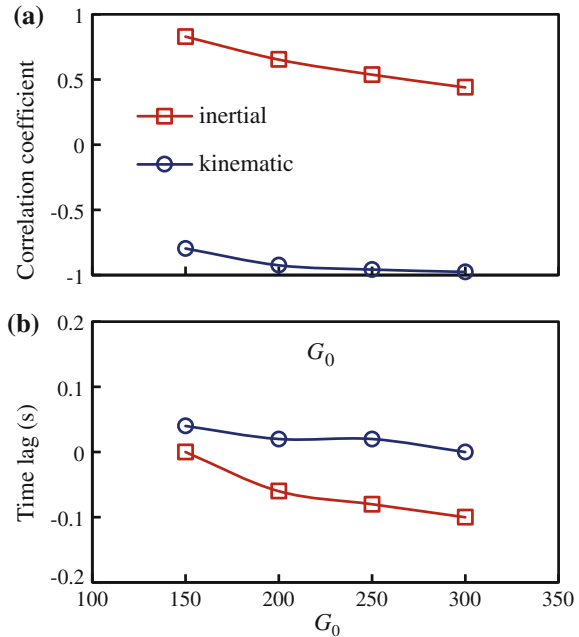


Fig. 3.34 Correlation coefficient and time lag of structure acceleration and pile head moment (inertial interaction), and of soil surface displacement and pile head moment (kinematic interaction) in relationship to soil elastic shear modulus parameter G_0 for single pile models with pile cap

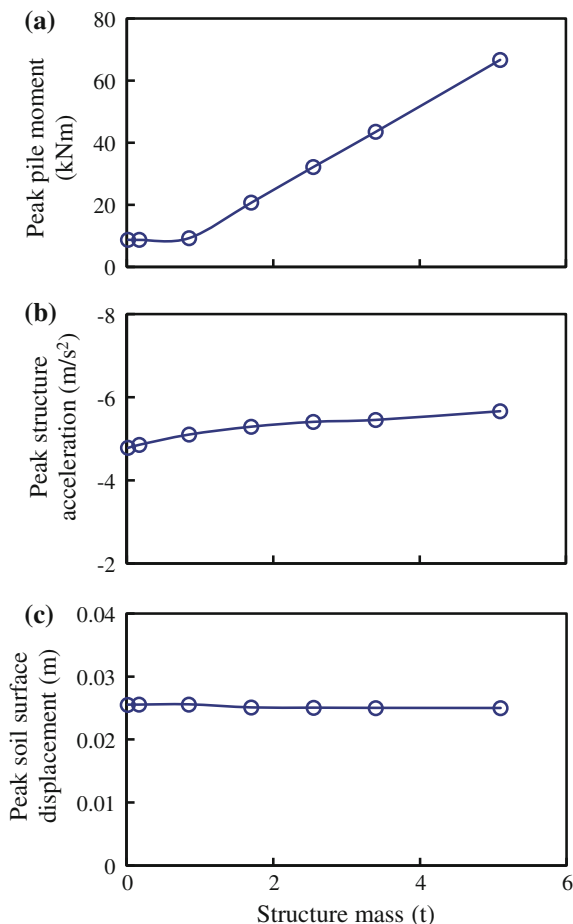


pile moment to reduce from -88 to -28 kN m, by 68 % (Fig. 3.34a). This indicates that for the single pile with pile cap setup, the soil kinematic deformation is highly influential to the pile moment demand, and limiting the soil deformation serves as a valid way to reduce the seismic pile bending moment demand. It should be noted out that the change in G_0 value also caused the peak structure acceleration to change from -3.1 to -4.3 m/s², however, as analysed in the influence of inertial effects, such a small change in inertial force would not significantly affect the pile moment. The change in soil elastic shear modulus parameter (G_0) value would not only change the displacement of the soil, but would be expected to influence the soil-pile interaction stiffness, which is not looked into in this study.

Cross correlation analyses on models with different soil elastic shear modulus parameter (G_0) value show that the stiffness, and hence the kinematic deformation, of the soil also affects the correlations for inertial and kinematic interactions (Fig. 3.35). The kinematic deformation shows stronger correlation with the pile moment with higher soil stiffness, when the structure was 10.8 t, the correlation coefficient reaches -0.97 with 0 time lag. However the inertial force has stronger correlation with the pile moment in soil with lower stiffness, for model $C_{m10.8G150}$, the correlation coefficient is 0.83 with 0 time lag.

For the single pile with embedded pile cap setup, the coupling of inertial and kinematic interactions is strongly influenced by the magnitudes of both the structure inertial force and the soil kinematic deformation.

Fig. 3.35 Influence of structure mass on (a) peak pile moment, (b) peak structure acceleration and (c) peak soil surface displacement in single pile models without pile cap



3.4.3.2 Single Pile without Pile Cap

For the single pile without pile cap setup, dynamic simulations on LNS models with different structure mass are conducted to investigate the influence of inertial effect, with the results shown in Fig. 3.35. In these simulations, the change in structure mass had negligible effect on the soil surface displacement (Fig. 3.35c), and the peak structure acceleration only increased slightly from -4.8 to -5.7 m/s^2 when the structure mass increased from 0.017 to 5.1 t (Fig. 3.35b). In contrast to the single pile with pile cap setup, the change in structure mass has a strong influence on the peak pile moment. When the structure mass increased by 6 times from 0.85 to 5.1 t, the peak inertial force (mass times peak acceleration) increased by 6.7 times from 4.3 to 29.1 kN, the peak pile moment increased by 7.2 times from 9.3 to 66.7 kN m (Fig. 3.35a). However, when the structure mass is small enough, 0.85 t in this case, the maximum pile moment no longer appears at the pile head, hence the change in

structure mass has almost no influence on the peak pile moment. These results show that when the structure inertial force is strong enough for the peak pile moment to occur at the pile head in the single pile without pile cap setup, the dynamic pile moment demand increases almost linearly with increasing peak inertial force.

For the single pile without pile cap setup, Fig. 3.36 shows that in the model with a 0.017 t structure, the correlations between the pile moment and the structure acceleration, and between the pile moment and the soil surface displacement

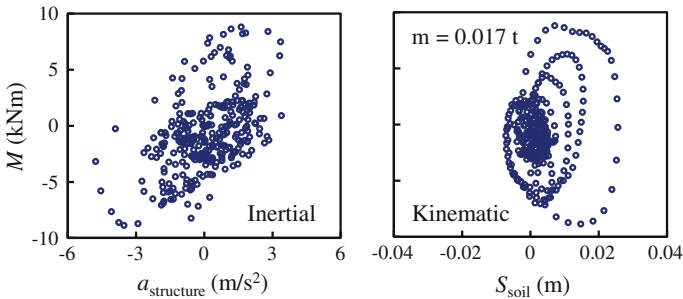
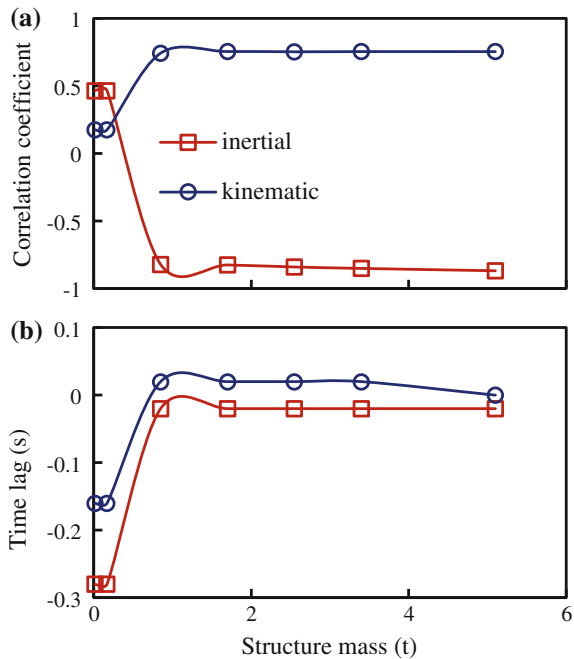


Fig. 3.36 Relationship between structure acceleration and pile moment (inertial interaction), and between soil surface displacement and pile moment (kinematic interaction) in the LNS model with 0.017 t structure

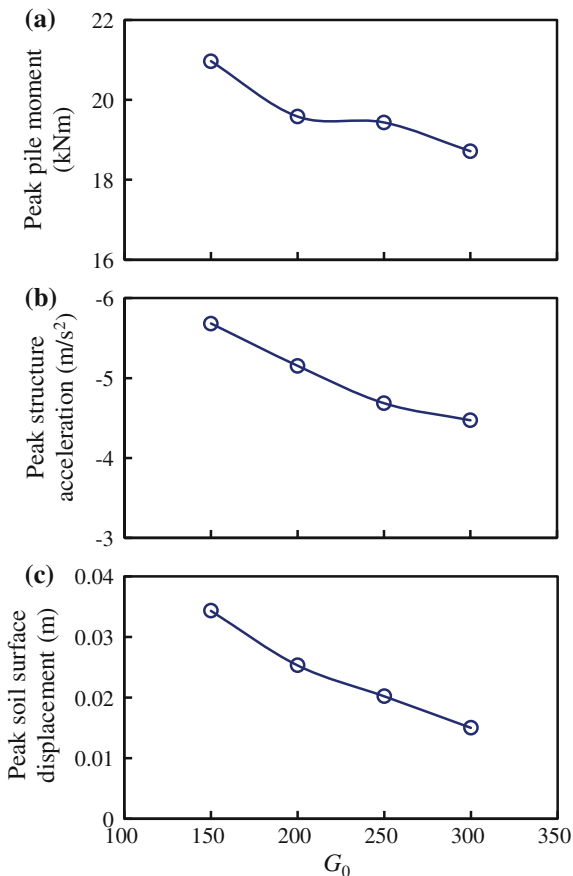
Fig. 3.37 Correlation coefficient and time lag of structure acceleration and pile head moment (inertial interaction), and of soil surface displacement and pile head moment (kinematic interaction) in relationship to structure mass for single pile models without pile cap



become much weaker than that in the model with structure mass of 1.7 t (Fig. 3.16b). The weaker correlations in this model is to be expected, as the maximum pile moment does not occur at the pile head, but at 3.5 m depth. When the structure mass is small enough so that the maximum pile moment does not occur at the pile head, the structure acceleration and the soil surface displacement has almost no correlation with the pile moment demand with large time lags (Fig. 3.37). However, if the structure mass is large enough, the pile moment has a correlation coefficient of around -0.85 and almost no time lag with structure acceleration, and has a correlation coefficient of around 0.75 and almost no time lag with the soil surface displacement, irrespective of the structure mass.

The influence of kinematic effects for the single pile without pile cap setup is investigated through dynamic simulations on LNS models with different soil elastic shear modulus parameter (G_0) value. Similar to the setup with pile cap, when G_0 value is changed from 150 to 300, the peak soil surface displacement reduces from 3.4 to 1.5 cm (Fig. 3.38c). This 56 % decrease in soil surface displacement only

Fig. 3.38 Influence of soil shear modulus parameter G_0 on (a) peak pile moment, (b) peak structure acceleration and (c) peak soil surface displacement in single pile models without pile cap



lead to a 10 % decrease in peak pile moment (Fig. 3.38a), which is most probably actually caused by the 17 % decrease in structure acceleration (Fig. 3.38b), based on the previous understanding of the influence of inertial effects. This shows that the soil kinematic deformation has little influence on the dynamic pile moment demand in the single pile without pile cap setup. However, if the inertial force from the structure is small enough that the maximum pile moment does not occur at the pile head, the influence of kinematic effects would be expected to be more significant.

Changes in soil elastic shear modulus parameter (G_0) value in LNS models caused no significant effects on the coupling of inertial and kinematic interactions. For the single pile without pile cap setup, it would be acceptable to consider the inertial and kinematic interactions to work in phase in designing for the pile moment demand.

3.5 Summary

A three dimensional finite element modelling method for piles in liquefiable ground is developed in this chapter. The method was validated against centrifuge shaking table tests, and subsequently employed in the study of the seismic response of piles. The unified plasticity model for large post-liquefaction shear deformation is used to simulate the liquefiable ground. Second order twenty node brick elements are used for the piles and a hyperbolic model for the soil-pile interface to provide appropriate physical representation of the soil-pile system. A staged modelling procedure is adopted for the method to provide correct initial conditions for the seismic analysis.

Three centrifuge shaking table tests on single piles with and without pile cap and superstructure, in level and inclined liquefiable grounds are conducted and simulated. The results of numerical simulation showed good agreement with the centrifuge test measurements of the accelerations and excess pore pressures within the soil, and especially the bending moments of the piles.

Some of the major factors for the seismic pile response in liquefiable ground observed in the centrifuge tests and past case histories are investigated using the proposed numerical simulation method. The existence of the pile cap is found to restrain the rotation of the pile head, change the bending mode of the pile, and hence cause piles with and without pile cap to experience bending moments of opposite directions. Inclined ground is found to increase lateral spreading of liquefied ground, and in turn result in greater pile residual moment. Even a modestly inclined ground was sufficient to generate a residual moment greater than the peak bending moment of a pile in a level but otherwise identical ground. The existence of a non-liquefiable crust restricts the pile rotation within the layer, causing the bending and pile moment to intensify at the interface between non-liquefiable and liquefiable layers.

The analyses in this chapter show that the roles that inertial structure force and kinematic soil displacement play on the bending moment of the pile differs in different setups. In single the pile with embedded pile cap setup, inertial structure force and kinematic soil displacement of the same direction causes opposite pile head moment. While for the single pile without pile cap setup, inertial structure force and kinematic soil displacement of the same direction generates pile head moment of the same direction. These differences in the roles of inertial and kinematic interactions are caused by the difference in pile head rotational constraint.

For the single pile with embedded pile cap setup, kinematic effects have a dominating influence on the pile moment, the coupling of inertial and kinematic interactions is strongly influenced by the magnitudes of both the structure inertial force and the soil kinematic deformation. The coupling of inertial and kinematic interactions is mostly affected by the magnitude of the structure inertial force in the pile group setup. For this setup, simply assuming the inertial structure force and kinematic soil deformation to be in sync or out of phase could lead to over-conservative or over-optimistic estimates of the dynamic pile moment demand. However, for the single pile without pile setup, inertial effects dominantly influence the pile moment, it seems reasonable to assume that the inertial and kinematic interactions work in sync to cause the dynamic pile moment demand.

References

- Abdoun T, Dobry R, O'Rourke TD, Goh SH. Pile response to lateral spreads: centrifuge modeling. *J Geotech Geoenvironmen Eng.* 2003;129(10):869–78.
- Andrianopoulos KI, Papadimitriou AG, Bouckovalas GD. Bounding surface plasticity model for the seismic liquefaction analysis of geotechnical structures. *Soil Dyn Earthq Eng.* 2010;30(10):895–911.
- Berrill J, Yasuda S. Liquefaction and piled foundations: some issues. *J Earthq Eng.* 2002;6(S1):1–41.
- Box GEP, Jenkins GM. Time series analysis: forecasting and control. Holden-day series in time series analysis. Holden-Day, San Francisco; 1970.
- Chaloulos YK, Bouckovalas GD, Karamitros DK. Pile response in submerged lateral spreads: common pitfalls of numerical and physical modeling techniques. *Soil Dyn Earthq Eng.* 2013;55:275–87.
- Clough GW, Duncan JM. Finite element analyses of retaining wall behaviour. *J Soil Mech Found Div.* 1971;97(12):1657–73.
- Elgamal A, Yang Z, Parra E. Computational modeling of cyclic mobility and post-liquefaction site response. *Soil Dyn Earthq Eng.* 2002;22(4):259–71.
- Gazetas G, Dobry R. Horizontal response of piles in layered soils. *J Geotech Eng.* 1984;110(1):20–40.
- González L, Abdoun T, Dobry R. Effect of soil permeability on centrifuge modeling of pile response to lateral spreading. *J Geotechn Geoenviron Eng.* 2009;135(1):62–73.
- Hushmand BR, Scott F, Crouse CB. Centrifuge liquefaction tests in a laminar box. *Geotechnique.* 1988;38(2):253–62.
- Kutter BL. Dynamic centrifuge modeling of geotechnical structures. *Transp Res Rec.* 1992;1336:24–30.
- Madabhushi G, Knappett J, Haigh S. Design of pile foundations in liquefiable soils. London: Imperial College Press; 2010.

- Yang J, Sze HY. Cyclic strength of sand under sustained shear stress. *J Geotech Geoenviron Eng.* 2011;137:1275–85.
- Zienkiewicz OC, Chang CT, Bettess P. Drained, undrained, consolidating and dynamic behaviour assumptions in soils. *Geotechnique.* 1980;30(4):385–95.
- Zienkiewicz OC, Chan AHC, Pastor M, Schrefler BA, Shiomi T. *Computational geomechanics with special reference to earthquake engineering.* Chichester: John Wiley & Sons; 1999.

Chapter 4

Dragload and Downdrag Settlement of Single Piles due to Post-liquefaction Reconsolidation

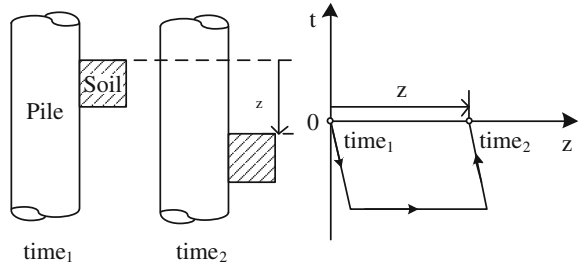
4.1 Calculation Method for Dragload and Downdrag Settlement

4.1.1 *Fundamental Error in Traditional Neutral Plane Solution*

A fundamental error with the traditional neutral plane solution is that the neutral plane solution assumes that the pile settlement and soil settlement are equal at the depth of the neutral plane. However, it is the relative velocity, not the relative displacement that must be zero at the neutral plane depth. Consider the elastic perfectly-plastic material response shown in Fig. 4.1. The neutral plane is defined as the position along the pile where shaft friction transitions from upward to downward, and is therefore zero. The load transfer curve in Fig. 4.1 illustrates two different points on where shaft friction is equal to zero, but they are associated with different amounts of displacement. This clearly establishes that relative displacement between pile and soil is not necessarily equal to zero at the depth where shaft friction is zero.

The kinematic condition describing relative movement between soil and pile at the neutral plane depth can be easily defined by traditional one-dimensional rate independent plasticity theory. The yield function is defined as $f = |Friction| - f_s$, and the Kuhn-Tucker complementary conditions require that $\dot{z}_p \text{sign}(Friction) \cdot f = 0$, where \dot{z}_p is the plastic displacement rate (e.g., Simo and Hughes 1998). In the elastic region where $f < 0$, the Kuhn-Tucker conditions dictate that $\dot{z}_p = 0$, whereas in the plastic region where $f = 0$, the Kuhn-Tucker conditions dictate that $\dot{z}_p \neq 0$. Extending these plasticity concepts to the neutral plane solution, the neutral plane is defined as the depth where shaft friction is zero, which corresponds to the elastic region where $f < 0$. Therefore $\dot{z}_p = 0$ at the neutral plane based on the Kuhn-Tucker complementary conditions. One-dimensional rate independent plasticity theory dictates that it is the relative plastic displacement **rate** between the soil and pile, \dot{z}_p ,

Fig. 4.1 Force-displacement behaviour between soil and pile considering elasto-plasticity



and not the relative displacement, z_p , that must be zero at the neutral plane depth. Note that the condition when $\dot{z}_p = 0$ and $f = 0$ also satisfies the Kuhn-Tucker complementary conditions. Therefore, $\dot{z}_p = 0$ does not necessarily indicate a condition of zero friction (e.g., consider the end of consolidation condition where soil and pile are not settling, but shaft friction is nevertheless mobilized along the pile). However, when friction is equal to zero, \dot{z}_p must be zero as well.

Considering that the relative velocity must be zero at the neutral plane depth, pile settlement can be computed as the integral of soil settlement velocity, V_{soil} , at the neutral plane depth over time:

$$S_{pile}(z_{np}(t)) = \int_0^t V_{soil}(z_{np}(t), t) dt \tag{4.1}$$

where $z_{np}(t)$ is the depth of the neutral plane at time t , and $V_{soil}(z, t) = \frac{\partial S_{soil}(z, t)}{\partial t}$, $S_{soil}(z, t)$ is the soil settlement at depth z and time t . For the special case where $z_{np}(t)$ is constant, the soil settlement would be equal to the pile settlement at the neutral plane depth. However, if $z_{np}(t)$ is not constant, the pile settlement will, in general, be different than the soil settlement at the neutral plane depth, and will depend on the evolution of the neutral plane depth over time. For typical consolidation problems, the neutral plane depth will change with time because the effective stresses at the soil-pile interface will change as consolidation evolves. The traditional NPS utilizes the end-of-consolidation neutral plane depth and does not account for the evolution of neutral plane depth over time, and computes an erroneous settlement as a result.

4.1.2 Beam on Nonlinear Winkler Foundation Solution

A schematic of a BNWF approach that removes many of the assumptions in the traditional NPS is shown in Fig. 4.2. The solution utilizes the TzLiq1 material model implemented in OpenSees (McKenna and Fenves 2001) along the length of the pile to model shaft friction, and beam column elements for the structural properties of the pile. End bearing in the BNWF analysis can be modelled in two

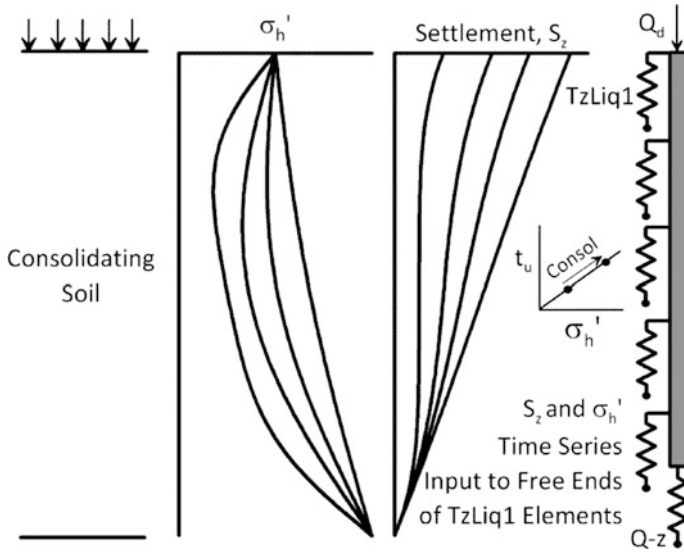


Fig. 4.2 Schematic of BNWF method using TzLiq1 material

different ways: (i) a Q-z element (e.g., QzSimple1 in OpenSees) can be used at the pile tip to capture variation in end bearing load with pile tip settlement, or (ii) an upward force may be applied at the pile tip to represent a constant end bearing resistance. A load may also be applied to the pile head. The TzLiq1 and QzSimple1 material models adopt a nonlinear plasticity formulation such that the backbone load transfer behaviour closely matches published relations [Reese and O’Neill (1988) or Mosher (1984) for t-z behaviour; Reese and O’Neill (1988) or Vijayvergiya (1977) for Q-z behaviour]. A complete description of the material model equations is beyond the scope of this study, but can be found in Boulanger et al. (2003), and in the OpenSees documentation. The TzLiq1 material was implemented in OpenSees with the specific intention of modelling piles in liquefiable soils (hence its name), but it is equally well suited for modelling downdrag problems resulting from more traditional consolidation mechanisms. The BNWF solution inherently includes shifting of the neutral plane depth due to discretization of time, the link between t-z properties and consolidation stress, and enforcement of force equilibrium in each increment.

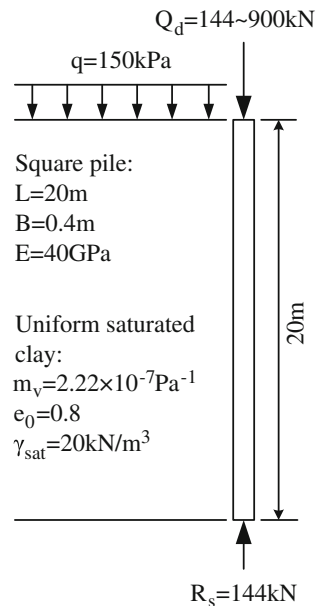
The key feature that makes the TzLiq1 materials amenable to consolidation analysis is the relation between f_s (also called t_{ult} or t_u in the literature) and effective stress in the soil. The TzLiq1 material assumes that f_s varies linearly with σ' , and is zero when σ' is zero. This is an important improvement upon previous analysis approaches that utilized constant f_s , regardless of consolidation condition. The analysis proceeds by computing values of f_s at each node along the pile based on the initial effective stress condition and soil-pile interface friction angle. Subsequently, time- and depth-dependent values of σ' and soil settlement, S_{soil} , are input to the

free-ends of the t-z elements, and the f_s values are updated to be compatible with σ' at each increment.

A simple example problem consisting of a 20 m long reinforced concrete pile embedded in a layer of clay (Fig. 4.3) is selected to demonstrate the BNWF downdrag solution, and for comparison with the traditional NPS. The uniform clay layer has a saturated unit weight of 20 kN/m^3 , initial void ratio of 0.8, and coefficient of compressibility (m_v) of $2.22 \times 10^{-4} \text{ kPa}^{-1}$. A 150 kPa surcharge is applied at the surface of the clay layer, resulting in a uniform vertical strain of 3.3 %, and an ultimate surface settlement of 0.67 m.

The square pile with 0.4 m side length (B) is modelled using elastic beam column elements with Young’s modulus of 40 GPa (consistent with typical reinforced concrete). The pile was discretized into 100 elements (101 nodes) evenly distributed along its length. The soil-pile interface friction angle δ is set as 28° and the at-rest earth pressure coefficient K_0 was set as 0.5. The ultimate soil-pile interface friction is calculated as $f_s = \sigma'_v K_0 \tan \delta$. The load transfer behaviour followed Reese and O’Neill’s (1988) relation for clay, and the value of z_{50} (i.e., the displacement at which half of the ultimate shaft friction is mobilized) was set to 0.0002 m. The resulting load transfer curve is fairly stiff, and is consistent with empirical observations that ultimate shaft friction is mobilized at small relative displacements on the order of millimetres. At the tip of the pile, a constant upward load of 144 kN was imposed to simulate full development of the undrained tip resistance during downdrag. A constant upward load was selected instead of a Q-z element at the pile tip to facilitate a direct comparison with the traditional neutral plane solution. The geotechnical capacity of the pile can be calculated through the

Fig. 4.3 Basic pile and soil setup for the example analyses



sum of fully mobilized upward shaft friction and tip resistance, which comes up to 995 kN. The solution was computed for various values of pile head load within the geotechnical capacity prior to consolidation, ranging from 144 to 900 kN. The example pile has a rather low end bearing resistance. For design, piles are often founded in more competent strata to provide higher end bearing resistance. In such cases, the neutral plane may be near the pile tip, which would reduce or eliminate downdrag settlement.

The example problem was solved using three different types of drainage conditions: drainage through both the top and bottom of the clay layer (double drainage, DD), single drainage through the top (SDtop), and single drainage through the bottom (SDbottom). The consolidation solution followed the Fourier series expansion of Terzaghi’s one dimensional consolidation theory:

$$u(z, t) = \frac{4p}{\pi} \sum_{n=0}^{\infty} \frac{1}{2n+1} \sin \frac{(2n+1)\pi z}{2H} \exp \left(-(2n+1)^2 \left(\frac{\pi^2}{4} \right) T_v \right) \tag{4.2}$$

where $u(z, t)$ is the excess pore pressure at depth z and time t , H is drainage path length, and T_v is the time factor defined as $T_v = \frac{c_v}{H^2} t$. Isochrones of the consolidation ratio, U_z , computed from Eq. 4.2 are shown in Fig. 4.4, and are also available in many soil mechanics text books (e.g., Holtz et al. 2011). Time- and depth-dependent values of vertical effective stress, $\sigma'_v(z, t)$ for the free end of the t-z elements were computed as $\sigma'_v(z, t) = \sigma'_{vf}(z) - u(z, t)$, where $\sigma'_{vf}(z)$ is the final vertical effective stress after consolidation at depth z . Utilizing Terzaghi’s 1-D consolidation theory inherently neglects excess pore pressures caused by pile installation, and changes to soil permeability and compressibility during consolidation.

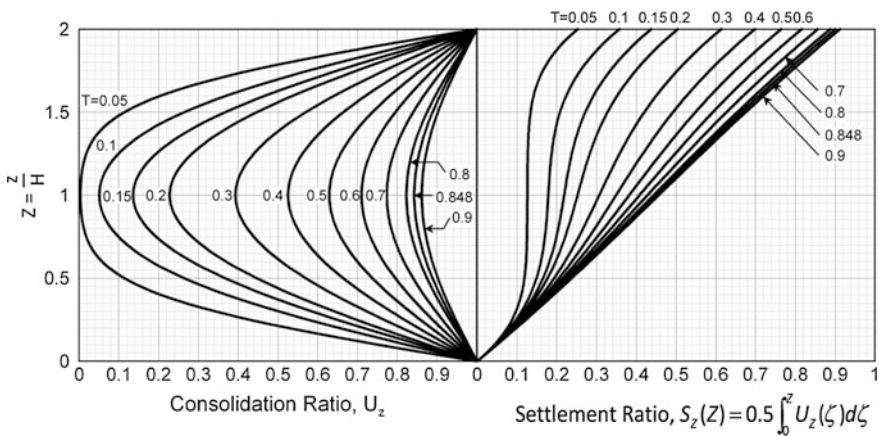


Fig. 4.4 Pore pressure and settlement isochrones from Terzaghi’s one dimensional consolidation theory

The soil settlement $S_{soil}(z, t)$ in the clay layer was acquired by integrating the vertical strain in the soil profile as the clay consolidates. Isochrones of the dimensionless settlement ratio computed by integrating U_z with depth are also shown in Fig. 4.4 based on the assumptions that double drainage boundary conditions apply, and settlement is zero at the bottom of the consolidating layer. Soil settlement profiles at a desired time can be computed by multiplying the appropriate settlement ratio by the ultimate surface settlement. Settlement ratio isochrones for single drainage conditions are not presented herein for brevity, but can easily be obtained using the methods described earlier.

The computed time- and depth-dependent values of $\sigma'_v(z, t)$ and $S_{soil}(z, t)$ were imposed on the free ends of the TzLiq1 elements, and solutions of pile settlement were computed using OpenSees. The UpdateMaterialStage command was utilized prior to the first load increment to initialize the TzLiq1 materials so that the initial capacities were tied to the initial effective stress values. Subsequently, the capacities were updated as the effective stresses increased during consolidation. Penalty constraints were used to enforce the imposed displacement boundary conditions, and convergence was based on the norm of the displacement residuals (i.e., NormDispIncr in OpenSees) with the tolerance set to 10^{-8} . A Newton-Raphson algorithm was used to iterate on an equilibrium displacement field for each loading increment. Solutions were computed using 800 increments to reach an average degree of consolidation beginning at 0 % and ending at 99.9 %, and an automatic substepping algorithm was utilized to reduce the step size when convergence did not occur in 25 Newton-Raphson iterations.

Figures 4.5, 4.6 and 4.7 show the soil settlement, effective stress, soil-pile friction, and axial pile load distributions at four different average degrees of consolidation (25, 50, 75 and 99.9 %) for a pile head load of $Q_d = 445$ kN. The depth of the neutral plane is clearly evident at the abrupt transition from negative to positive friction, and also at the depth of the maximum axial load. The profiles in Figs. 4.5,

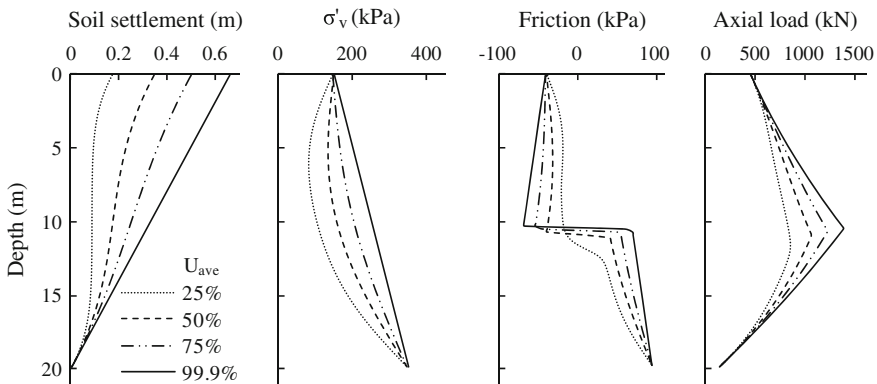


Fig. 4.5 Soil and pile responses at different average degrees of consolidation in a double drainage soil profile. $Q_d = 445$ kN

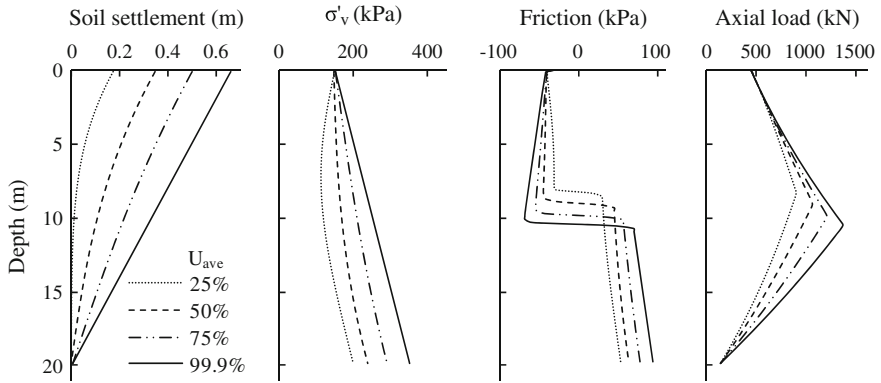


Fig. 4.6 Soil and pile responses at different average degrees of consolidation in a single drainage through the top soil profile. $Q_d = 445$ kN

4.6 and 4.7 are identical at the end of primary consolidation, but differences in the profiles arise at intermediate degrees of consolidation.

In the double drainage case, effective stress initially builds up at both the top and bottom of the clay layer, causing soil strain and increase in soil-pile friction to be more prominent at the top and bottom. The increase in friction at the top serves to partially offset the increase in friction at the bottom, and the depth of the neutral plane remains nearly constant at slightly deeper than 10 m as consolidation evolves. On the other hand, for the case with single drainage through the top the friction increases more quickly at the top of the pile, which shifts the neutral plane upward. As consolidation progresses, friction increases with depth along the pile and the neutral plane shifts downward to its final equilibrium depth at the end of consolidation. Conversely, when single drainage occurs through the bottom the friction

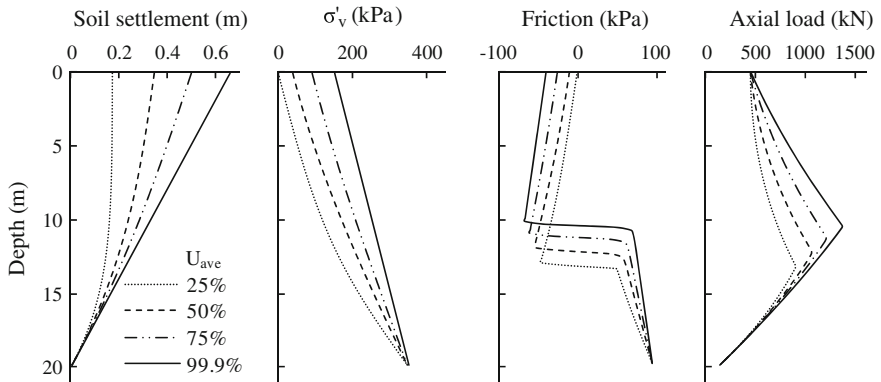


Fig. 4.7 Soil and pile responses at different average degrees of consolidation in a single drainage through the bottom soil profile. $Q_d = 445$ kN

increases first at the bottom of the pile, which shifts the neutral plane downward, and it progresses upward to its final equilibrium position at the end of consolidation.

The depth to the neutral plane, and pile settlement at the neutral plane depth are plotted versus average degree of consolidation in Fig. 4.8. The pile was essentially rigid (elastic compression was only a fraction of a millimetre at the end of consolidation), so Fig. 4.8 can be interpreted as pile head settlement. For the double-drained case, the pile settlement increases approximately linearly with average degree of consolidation, reaching a final value of 0.306 m. For the SDtop case, the initial incremental soil strains occur first near the surface such that soil settlement is nearly zero below the neutral plane depth, which causes a very slow initial pile settlement rate. However, with time, the neutral plane shifts upward as the downdrag stresses increase near the pile head, soil strains shift downward as consolidation progresses, and the pile settlement rate increases quickly. The pile settlement at the end of consolidation is 0.350 m, which is 14 % larger than the double-drained case. For the SDbottom case, the pile initially settles quickly because incremental soil strains are largest deep in the profile, below the neutral plane depth. However with time the incremental soil strains move upward, resulting in a reduction in pile settlement rate. The final pile settlement reaches 0.262 m, which is 14 % less than the double-drained case. The traditional NPS claims that the pile settlement is equal to the soil settlement at the depth of the neutral plane at the end of consolidation, which is 0.310 m for the example problem. This value is close to the double-drained case, but differs from the SDtop and SDbottom cases by $\pm 14\%$, which is a non-negligible amount.

Fig. 4.8 Neutral plane depth and pile settlement histories. $Q_d = 445$ kN. **a** Neutral plane depth versus average degree of consolidation. **b** Pile settlement versus average degree of consolidation compared with conventional neutral plane solution

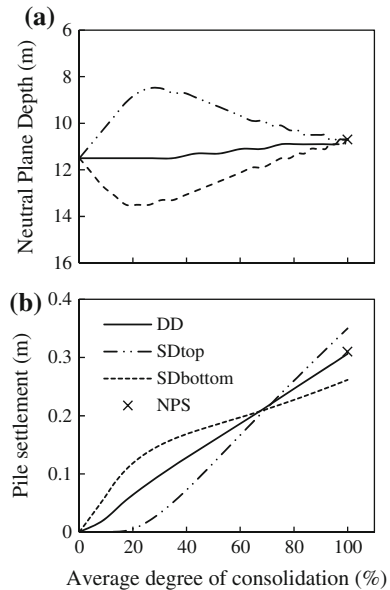
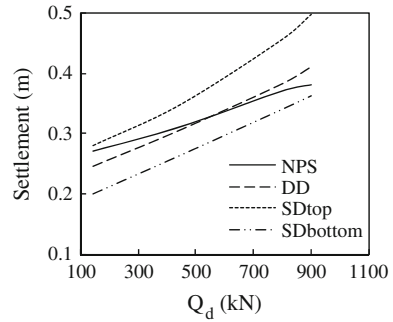


Fig. 4.9 Pile settlements versus pile head load in the neutral plane solution compared with BNWF results under different drainage conditions



Having investigated the effect of drainage conditions on the settlement of piles in consolidating soil, we now turn our attention to the influence of pile head loading. Using the same procedures mentioned above, the settlement of single piles subjected to varying head loads within their geotechnical capacity were calculated through both the BNWF method and traditional NPS under the three drainage conditions (Fig. 4.9). For all four solutions, the pile settlement increased as the pile head load increased because the head load shifted the neutral plane upward in the soil profile. The traditional NPS solution does not match any of the BNWF cases, though it corresponds more closely with the double drainage case than with the single-drainage cases.

4.1.3 Modified Neutral Plane Solution

Although the BNWF method correctly captures the evolution of neutral plane depth over time, and its influence on pile settlement, performing such a BNWF analysis is currently beyond the capabilities of software commonly used in geotechnical design. Therefore we now turn our attention to formulating a simple modification to the neutral plane solution that is amenable to spreadsheet calculation. The steps of the modified neutral plane solution are summarized in the flow chart in Fig. 4.10. The first step involves discretizing time into convenient intervals for solving the consolidation problem. Times should be selected to correspond to reasonably consistent average degrees of consolidation (e.g., times corresponding to $U_{ave} = 0, 25, 50, 75,$ and 100% might be selected if five time steps are desired). Second, profiles of excess pore pressure and vertical strain are computed at each time using consolidation theory, and the settlement profile $S_{soil}(z_{np}(t_i), t_i)$ is computed by integrating the vertical strain profile from the bottom up (e.g., see Fig. 4.4). Third, the depth of the neutral plane is solved at each time interval in the traditional manner originally suggested by Fellenius (1972) in which forces are summed from the top down and bottom up, and the neutral plane depth lies at the intersection of the two lines. However, the shaft friction values must be based on the current effective stress at a particular depth based on the consolidation solution from step 2.

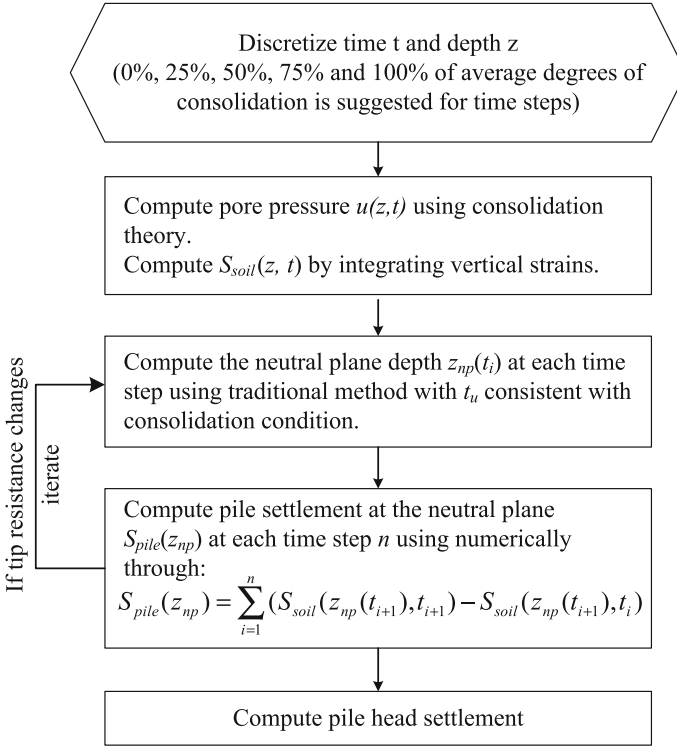


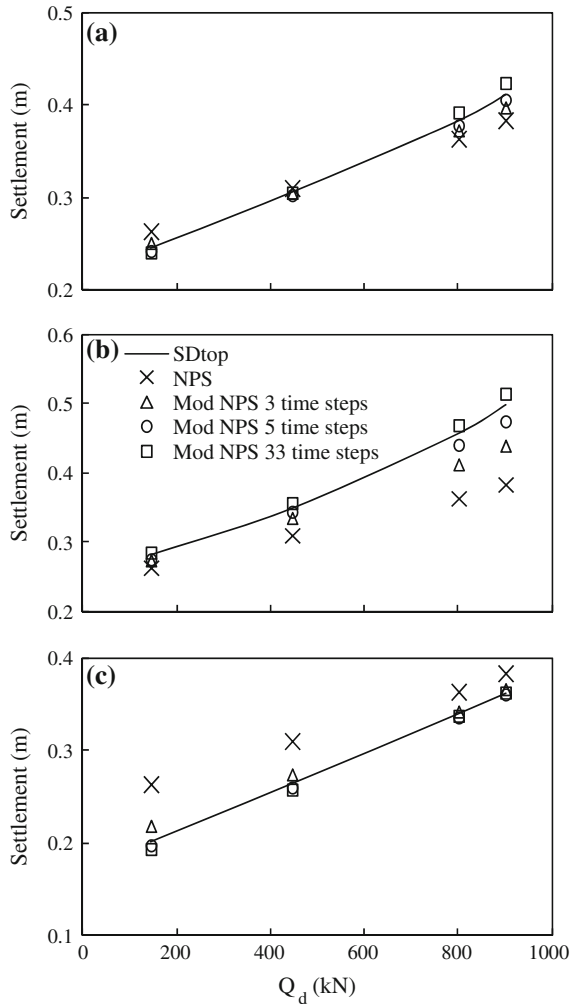
Fig. 4.10 Flow chart of the proposed modified neutral plane method

The variation in shaft friction during consolidation is precisely why the neutral plane shifts with time, and is why the traditional NPS incorrectly predicts pile settlement. Fourth, the pile settlement at the neutral plane depth is computed by integrating soil settlement velocity at the neutral plane depth over time. Numerical discretization of time transforms the integral of velocity into a difference in incremental displacements. Hence, the pile settlement for a particular time step, n , can be computed using the forward Euler integration method in Eq. 4.3:

$$S_{pile}(z_{np}) = \sum_{i=1}^n [S_{soil}(z_{np}(t_{i+1}), t_{i+1}) - S_{soil}(z_{np}(t_{i+1}), t_i)] \quad (4.3)$$

For cases where elastic deformation of the pile is anticipated to be significant, axial strains must be integrated over the pile length to compute the contribution of pile shortening to head settlement. Furthermore, if a load-transfer curve (i.e., a Q-z relationship) is utilized rather than a constant specified tip resistance, iteration is required to obtain a tip resistance that is compatible with the current pile tip settlement.

Fig. 4.11 Comparison between settlements calculated by the BNWF method and the modified neutral plane method using different number of intervals (including the conventional neutral plane solution)



The example problem presented in Figs. 4.5, 4.6 and 4.7 is also analysed using the modified NPS using various numbers of time steps (3, 5, and 33). The time steps are chosen to be at constant intervals of average degree of consolidation. Figure 4.11 compares the BNWF method and the modified neutral plane method. The modified NPS accuracy increases as the number of time steps increases. The small differences between the modified NPS with 33 time steps and the BNWF solution are likely attributed to differences in time discretization (800 time steps compared with 33) and elasto-plasticity of the t-z materials in the BNWF solution compared with the assumption of rigid plasticity in the modified NPS. Using a modest number of 5 time steps provides reasonable solutions for all three cases, and is reasonably amenable to spreadsheet calculation.

4.1.4 Calculation Method for Post-liquefaction Reconsolidation Process

In order to extend the BNWF and modified NPS solutions for the downdrag of piles to cases of post-liquefaction reconsolidation, special consideration would have to be given to the post-liquefaction reconsolidation process. Considering the inadequacies in the modelling of liquefaction induced settlement of sand using currently developed constitutive models, simplified empirical approaches are adopted in this chapter.

For reconsolidating sand, the coefficients of compressibility and permeability changes during the process. For the coefficient of compressibility, the equation suggested by Seed et al. (1975) is used:

$$\frac{m_v}{m_{v0}} = \frac{\exp(y)}{1 + y + y^2} \quad (4.4)$$

where m_{v0} is the coefficient of compressibility at zero excess pore pressure, y is related to the excess pore pressure ratio and relative density, as $y = 5(1.5 - D_R)r_u^b$, $b = 3(4^{-D_R})$. The greater the excess pore pressure ratio is, the larger the coefficient is, as shown in Fig. 4.12.

As for the change of permeability, Shahir et al. (2012) suggested based on centrifuge test observations that during the excess pore pressure dissipation phase:

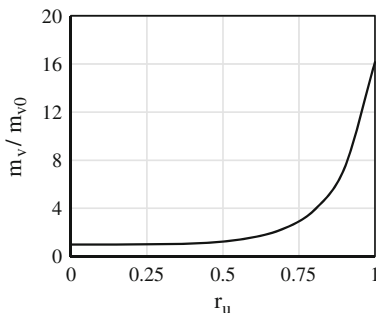
$$\frac{k_d}{k_i} = 1 + (\alpha - 1) \times r_u^\beta \quad (4.5)$$

where k_i is the coefficient of permeability when the excess pore pressure is zero, α and β are two parameters.

Upon introducing the changes in permeability and compressibility, the 1D consolidation theory can only be solved numerically:

$$\frac{u(i, t + 1) - u(i, t)}{\Delta t} = C_v \frac{u(i + 1, t) - 2u(i, t) + u(i - 1, t)}{\Delta z^2} \quad (4.6)$$

Fig. 4.12 Relationship between the coefficient of compressibility and the excess pore pressure ratio (After Seed et al. 1975)



where i and t are the discretized spatial and time indices, as shown in Fig. 4.13. In the solution, drained, undrained and interface boundary conditions are given as:

$$u_{drain} = 0 \tag{4.7}$$

$$u(n - 1, t) = u(n + 1, t) \tag{4.8}$$

$$\frac{k_1}{\Delta z_1} (u(m, t) - u(m - 1, t)) = \frac{k_2}{\Delta z_2} (u(m + 1, t) - u(m, t)) \tag{4.9}$$

4.2 Method Validation

4.2.1 Simulation of Single Pile in Consolidating Soil

To validate the BNWF approach and modified NPS, a model pile from a centrifuge test by Lam et al. (2009) is analysed. The centrifuge test was conducted at the Geotechnical Centrifuge Facilities at the Hong Kong University of Science and Technology to investigate axial load effects on piles in consolidating ground. The test program involved multiple pile foundations, but only one single pile test (test no. 1 in their paper) is analysed here. The centrifugal acceleration was 60 g and results are presented in prototype dimensions.

An instrumented tubular aluminium pile with an outer diameter (D) of 1.2 m and wall thickness (t_{wall}) of 9 cm was installed in an 18 m thick layer of clay (Speswhite China clay) consolidated to a vertical effective stress of 80 kPa before pile installation and spin up (Fig. 4.14). The clay was sandwiched between layers of dense Leighton Buzzard sand layer that provided a double-drained consolidation condition. The pile tip was 1.2 m above the bottom of the clay layer. The top sand layer provided a surcharge of 45 kPa, resulting in a measured 10 kN drag load on the pile from the sand. No load was applied to the pile head. The saturated unit weight,

Fig. 4.13 Discretization for the numerical solution of the 1D consolidation problem

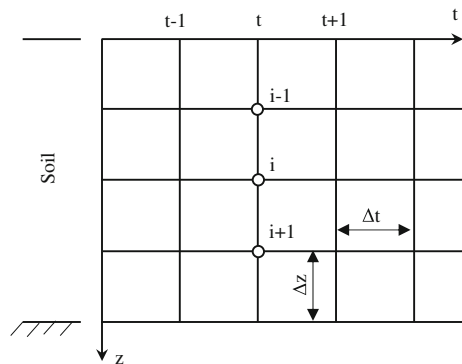
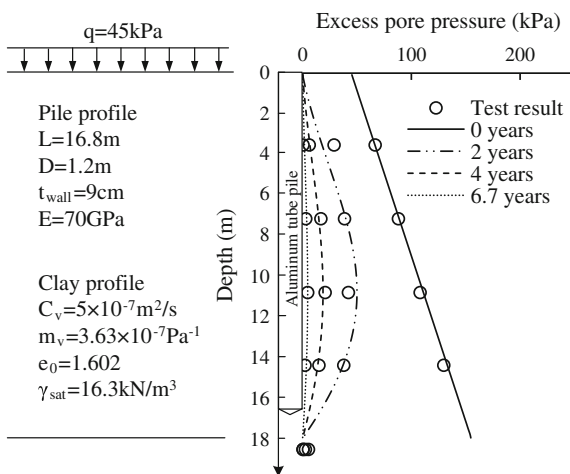


Fig. 4.14 Excess pore pressure isochrones from Terzaghi's one dimensional consolidation theory compared with test data (Test data from Lam et al. 2009)



at-rest earth pressure coefficient, and initial void ratio of the clay were specified to be 16.3 kN/m^3 , 0.58 , and 1.602 respectively. The coefficient of consolidation c_v was back calculated to be $5 \times 10^{-7}\text{ m}^2/\text{s}$ from the distributions of excess pore pressure measured in the test using Terzaghi's one dimensional consolidation theory. Isochrones of predicted and measured excess pore pressure plotted in Fig. 4.14 show good agreement. The coefficient of compressibility $m_v = 3.63 \times 10^{-7}\text{ Pa}^{-1}$ was back calculated based on the measured soil surface settlement of 654 mm .

In the BNWF simulations, the backbone of Reese and O'Neill's (1988) load transfer curve was used for the t-z elements. The soil-pile interface friction angle was estimated from the distribution of dragload after consolidation to be 24° . The value of z_{50} (displacement at which 50 % of ultimate resistance is mobilized) was set to be 0.0005 m , such that 99 % of the shaft friction was mobilized at around $4\text{--}5\text{ mm}$.

A Q-z element was attached to the tip of the pile to model end bearing resistance. End bearing is a bit complicated for this problem because (i) it is unclear whether undrained or drained end bearing resistance would apply for the slow loading conditions induced during downdrag, and (ii) end bearing resistance would be anticipated to increase over time as the clay near the tip of the pile consolidates. Regarding (i), the test data can be used to provide some guidance since drained tip resistance is typically significantly larger than undrained tip resistance. Lam et al. (2009) stated that prior to spin up, the soil was preloaded to 80 kPa using a hydraulic press, resulting in an estimated undrained shear strength s_u of 17.6 kPa prior to swelling of the clay, giving a strength ratio $\frac{s_u}{\sigma'_v} = 0.22$. Invoking concepts of normalization of undrained shear strength with consolidation stress and overconsolidation ratio (e.g., Ladd 1991), the undrained shear strength at the tip of the pile was estimated as $s_u = 0.22 \cdot \sigma'_v \cdot OCR^{0.8}$. The undrained shear strength prior to spin-up was estimated to be 9 kPa , and the final undrained shear strength at the end of reconsolidation was estimated to be 35 kPa based on the effective stress profiles in Fig. 4.14. Computing tip resistance as $Q_t = 10S_{uA}$ the initial and final tip

resistance came to 100 and 400 kN, respectively. At the end of consolidation, when the pile had settled significantly and clearly mobilized the ultimate tip resistance, the axial load at the tip of the pile was quite close to 400 kN based on extrapolation from the deepest strain gauge measurement (Fig. 4.15). Although a bearing factor of 9 is commonly used for undrained tip resistance, many researchers suggest that it is too low and suggest a higher value ranging from about 9 to 12 (e.g., Salgado 2008), so the fact that a bearing factor of 10 agreed well with the data is not surprising. On the other hand, the drained bearing capacity would be significantly larger than the measurements [e.g., over 1300 kN is estimated using Meyerhof’s (1976) bearing factors for a friction angle of only 20°]. Hence, we conclude that undrained tip resistance was mobilized during downdrag.

A Q-z element was attached to the pile tip, and the capacity of the element was increased from 100 to 400 kN in proportion to degree of consolidation at the pile tip elevation during consolidation. The z_{50} value was set to 0.012 m such that the ultimate load is mobilized at approximately 8 % of the pile diameter, which is consistent with the range presented by Reese and O’Neill (1988).

Figure 4.15 shows the soil and pile responses at different average degrees of consolidation from the BNWF solution along with the final axial load distribution measured during the test. The final axial load distribution matches the centrifuge test data reasonably well. The final pile head settlement was estimated to be 0.194 m (Fig. 4.16), which corresponds well with the measured settlement of 0.206 m (-6 % error).

In addition to the BNWF solution, the settlement was computed using the modified NPS with time discretization at $U_{ave} = 0, 25, 50, 75$ and 100 %. Iteration was used to match the properties of the same Q-z relation used in the BNWF solution. The final pile settlement using the modified NPS method was 0.208 m, which is also very close to the measured settlement (+1 % error). On the other hand, the traditional NPS method predicts the pile settlement to be 0.277 m (+34 % error),

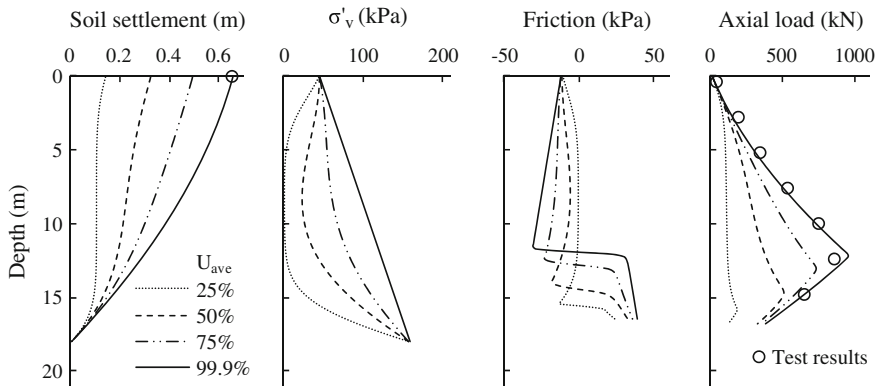
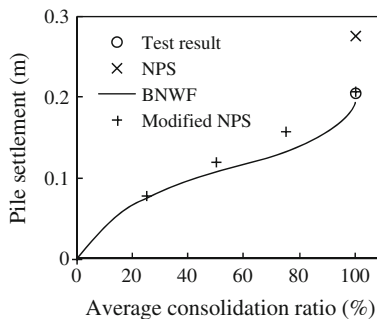


Fig. 4.15 Soil and pile responses at different average degrees of consolidation compared with centrifuge test data (Test data from Lam et al. 2009)

Fig. 4.16 Pile settlement results from test data and different calculation methods (Test data from Lam et al. 2009)



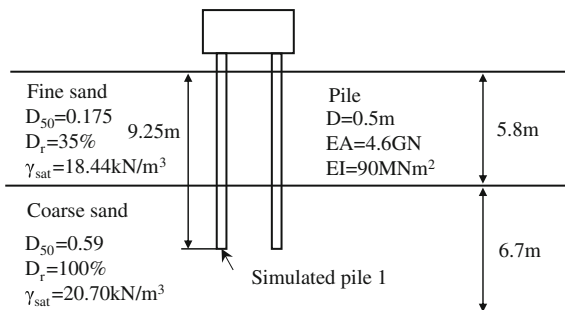
which is significantly larger than the measured value and the values computed from the BNWF method and modified NPS method. The over-prediction of the traditional NPS method is expected because the neutral plane begins near the tip of the pile and transitions upward as consolidation progresses. Using the final neutral plane position in the traditional NPS method therefore over-estimates pile settlement.

4.2.2 Simulation of Single Pile in Post-liquefaction Reconsolidating Soil

In order to validate the effectiveness of the proposed BNWF method in calculating the dragload and downdrag settlement of piles in post-liquefaction reconsolidating ground, the post-seismic measurements from the centrifuge shaking table test (MS06) conducted by Stringer and Madabhushi (2013) are simulated (Fig. 4.17).

The basic setup of the test is shown in Fig. 5.18, which is carried out under 46 g centrifugal acceleration, the prototype scales will be used in the following descriptions of the test. The piles in the test is 9.25 m long, with a diameter of 0.5 m (EA = 4.6 GN, EI = 90 MNm²). The pile spacing is 5.8 times that of the pile diameter. Only the strain of pile number 1 was measured during the test.

Fig. 4.17 Setup of Stringer and Madabhushi's (2013) centrifuge test



The ground consisted of two layers of Leighton Buzzard sand, the top layer of 5.8 m having 35 % relative density, while the bottom 6.7 m had a relative density of 100 %. Due to the high density and large particle size of the bottom sand layer, its consolidation speed is much quicker than the top layer, and causes the pile settlement to be very limited.

In the simulations, the initial permeability coefficients of the top and bottom layers are assumed to be 3×10^{-4} and 6×10^{-4} m/s², respectively. The compressibility coefficient is set to be 6.7×10^{-7} and 1.0×10^{-8} Pa⁻¹, respectively. Figure 4.18 plots the excess pore pressure distribution at five different instances, showing that the proposed method to be adequate in calculating the post-liquefaction reconsolidation process. The computed ground surface subsidence is 0.18 m, since the ground settlement was not reported for this test, the simulation result is not directly comparable with test data. However the ground settlement for tests MS07 and MS09, having similar ground conditions as MS06, were measured to be 0.14–0.18 m, which is close to the simulation results for MS06.

To apply the BNWF method for the simulation of this test, the at rest earth pressure coefficient is assumed to be 0.5 as Stringer and Madabhushi (2013) suggested, and the friction angle between the pile and the soil is 17°, the ultimate pile tip resistance is set at 8500 kPa based on the Chinese technical code for building pile foundations (Ministry of Housing and Urban-Rural Development of China, 2008). The pile head axial load can be back-calculated from the test data as 275 kN. Figure 4.19 shows that the simulated pile axial force matches that measured at the end of reconsolidation. During the reconsolidation process, the neutral plane moves

Fig. 4.18 Excess pore pressure during reconsolidation in MS06 (Test data from Stringer and Madabhushi’s 2013)

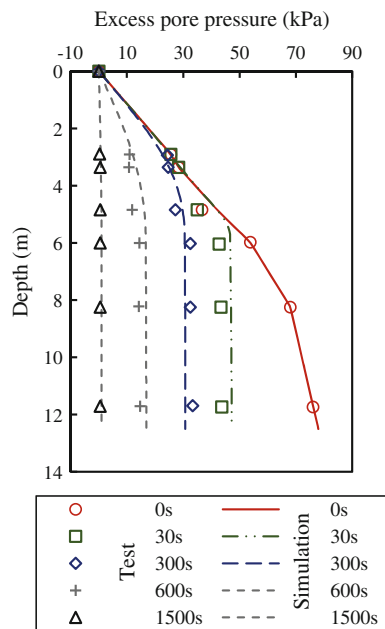
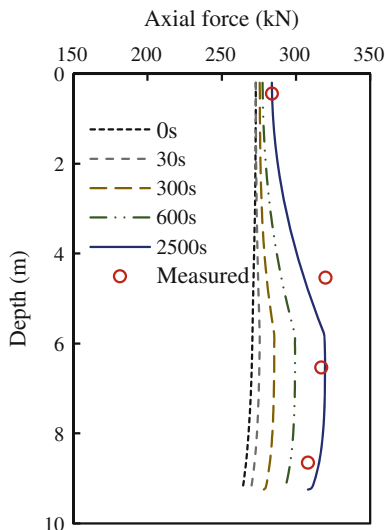


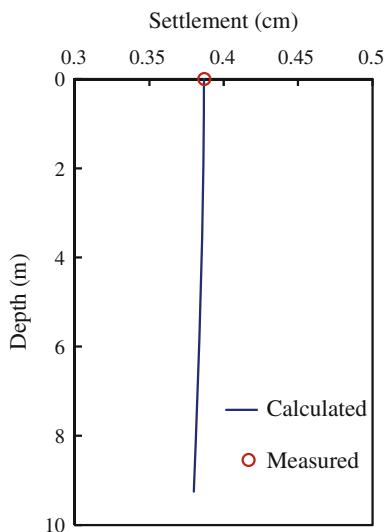
Fig. 4.19 Axial force of the pile in MS06 (Test data from Stringer and Madabhushi's 2013)



upwards, but remains within the bottom dense layer, with its final position close to the interface between the two layers. Neither the friction nor the tip resistance in the dense layer is fully mobilized.

Although the soil surface experiences 0.18 m settlement, the settlement is concentrated within the top fine sand layer. Since the neutral plane is always in the bottom dense layer, the pile settlement is extremely small, being only 0.38 cm, which is the same as the measured result in the centrifuge test, as shown in Fig. 4.20.

Fig. 4.20 Settlement of the pile in MS06 (Test data from Stringer and Madabhushi's 2013)



The simulations of the two centrifuge tests, one in consolidating clay, and the other in post-liquefaction reconsolidating sand, shows that the proposed methods to be capable of calculating the dragload and downdrag settlement of piles, and exhibited its advantage compared with the traditional NPS.

4.3 Dragload and Downdrag Settlement During Reconsolidation

Utilizing the proposed BNWF method and technique for calculating the post-liquefaction reconsolidation method, the pile axial force and settlement due to reconsolidation induced dragload and downdrag of single piles in typical liquefiable ground setups is analysed. Figure 4.21 shows the schematic diagrams of the two typical setups investigated, the influence of soil drainage conditions and compressibility on pile load and settlement is studied. In both setups, the pile tip sits in a non-liquefied soil layer, the pore pressure of which is assumed to be constant. For setup A, two layers of liquefiable sand layers, each 4 m thick, lie above the non-liquefied bearing layer. For setup B, the top 4 m of soil is considered non-liquefiable with constant pore pressure, while the middle 4 m layer is liquefiable sand, the reconsolidation speed of the middle layer depends on the drainage speed at the top of the layer. At the initial state, the liquefiable layers in both setups are assumed to be fully liquefied, and the reconsolidation process is calculated using the simplified method proposed in this chapter. Both of the setups are assumed to only allow single drainage through the top.

In both setups, the pile head axial load is 100 kN, the piles are 10 m square piles with a side length of 0.4 m, and an elastic modulus of 40 GPa. The saturated unit

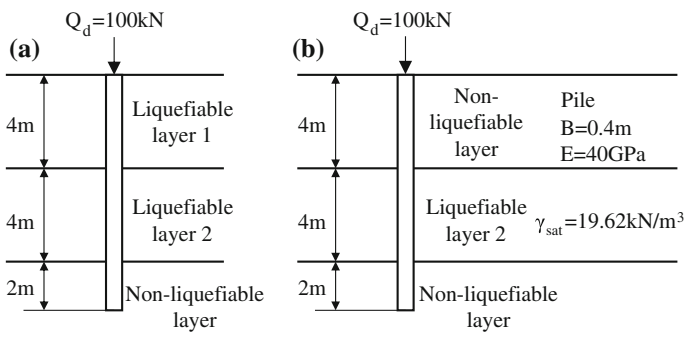


Fig. 4.21 Two setups for the analysis of the dragload and downdrag of piles in reconsolidating ground **a** setup A **b** setup B

weight of the soil in every layer is the same, at 19.62 kN/m^3 , with the at rest earth pressure coefficient being 0.5. The friction angle between the soil and the piles is 30° , and the ultimate pile tip resistance is 50 kN.

4.3.1 Liquefiable Ground Without Non-liquefiable Crust

For setup A with the top layer of the ground liquefiable, the effects of permeability and compressibility on downdrag is analysed. The soil conditions of the cases studied are listed in Table 4.1, among which case 1A is the “benchmark” case.

First, the effect of permeability on the response of piles during post-liquefaction reconsolidation is analysed. In cases 1A–6A, the compressibility of the two layers of liquefiable soil is the same, while the ratio of the permeability coefficient of the top layer over that of the second layer ranges from 1:1 to 16:1. Figure 4.22 and 4.23 plot the ground settlement, soil effective stress, pile friction, and pile axial force distribution at various degrees of consolidation.

By comparing the results from Fig. 4.22 and 4.23, the final ground settlement, effective stress, pile friction and pile axial force are identical, irrelevant of the reconsolidation process. However, during the reconsolidation process, the two setups exhibit distinctly different behaviour. When the permeability of the top soil layer is significantly larger than the second layer, the effective stress in the top layer is regained first, with settlement also developing faster than in the second layer,

Table 4.1 Soil permeability and compression coefficients in cases for setup A

Cases	k_{10} (mm/s)	m_{v10} (Pa ⁻¹)	k_{20} (mm/s)	m_{v20} (Pa ⁻¹)	
1A	1.0	1.0×10^{-7}	1.0	1.0×10^{-7}	
2A	2.0	1.0×10^{-7}	1.0	1.0×10^{-7}	
3A	4.0				
4A	8.0				
5A	16.0				
6A	∞				
7A	1.0				2.5×10^{-8}
8A		5.0×10^{-8}			
9A		2.0×10^{-7}			
10A		4.0×10^{-7}			
11A		1.0×10^{-7}	4.0×10^{-7}		

Note k_{10} and m_{v10} are the permeability and compressibility coefficients of the top layer, k_{20} and m_{v20} are those of the middle layer

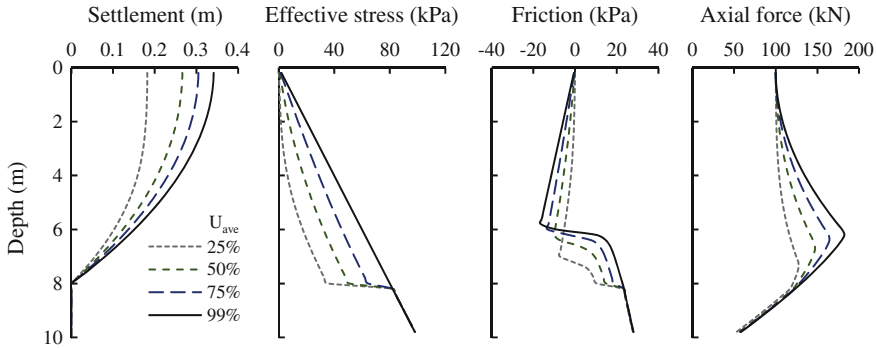


Fig. 4.22 Soil and pile response at various degrees of consolidation in case 1A

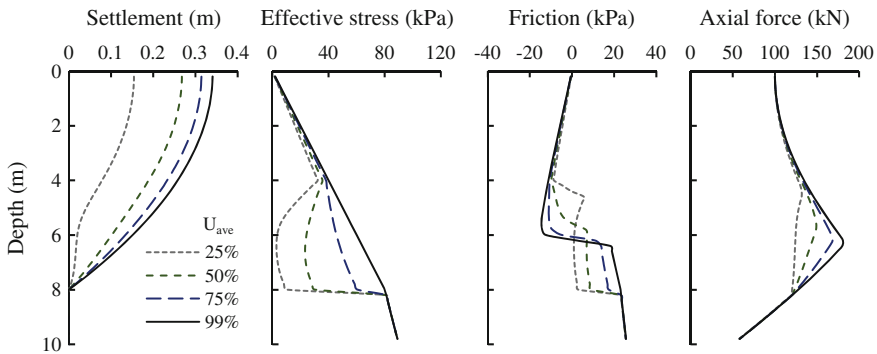


Fig. 4.23 Soil and pile response at various degrees of consolidation in case 5A

which causes the initial neutral plane position to be high, and moves downwards during reconsolidation. However, for case 1A where the permeability of the two layers are the same, the neutral plane starts at a much lower position, and rises during reconsolidation. Although these differences during the reconsolidation process do not affect the final pile axial force, the pile settlement will definitely be affected.

Figure 4.24 shows the effect of the top layer’s permeability on the final soil and pile settlement. No matter how the permeability changes, the settlement of the soil at the surface and layer interface remains unchanged. The pile settlement, however, increases as the permeability of the top layer increases, from 0.059 m when the permeability coefficient of the two layers are 1:1 to 0.224 m when they are ∞ :1. This change in pile settlement is due to the fact that larger permeability at the top would cause the effective stress to be recovered at the surface first, applying significant negative friction on the top portion of the pile, thus raising the initial neutral plane position, and consequently increases the settlement of the pile.

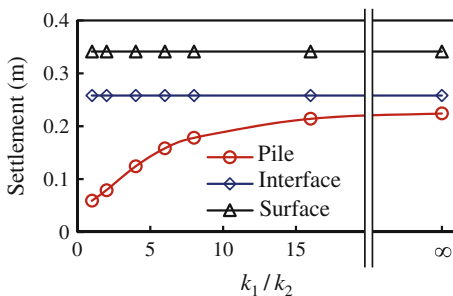


Fig. 4.24 Influence of the permeability of the top soil level in case A on soil surface and interface settlement, and on pile settlement

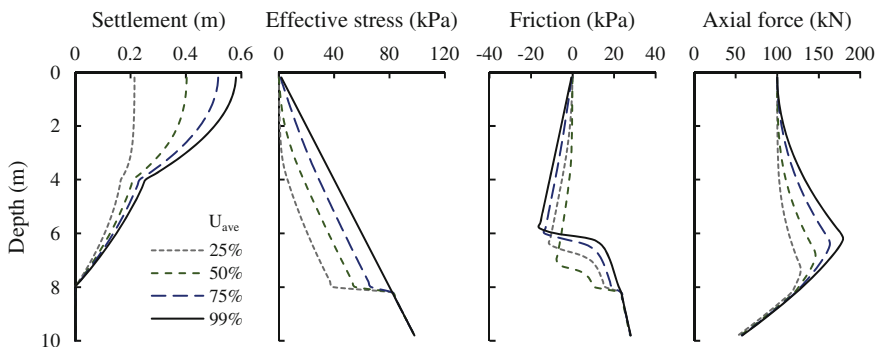
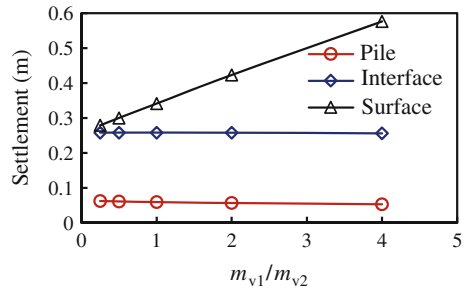


Fig. 4.25 Soil and pile response at various degrees of consolidation in case 10A

Cases 7A–11A are used to investigate the effect of top layer soil compressibility on downdrag in liquefiable ground. Figure 4.25 shows the soil response, pile friction, and pile axial load in case 10A. Compared with those of case 1A in Fig. 4.22, although the ground settlement increases significantly, the friction and axial force of the pile showed unnoticeable difference, and the neutral plane remained in the second liquefiable layer. Figure 4.26 reflects the effect of top layer compressibility on the settlement of the ground and pile. From case 11A to 10A, the ground surface settlement increases from 0.28 to 0.58 m, while the pile settlement remains almost constant at 0.059 m. This is due to the fact that the neutral plane is constantly in the second layer in these cases, and the change in the settlement of the top layer has no influence on the settlement within the second layer (Fig. 4.26). However, if the compressibility of the second layer is changed, causing settlement at the neutral plane position to change, the pile settlement would obviously change as well.

Fig. 4.26 Influence of the compressibility of the top soil level in case A on soil surface and interface settlement, and on pile settlement



4.3.2 Liquefiable Ground with a Non-liquefiable Crust

For setup B with a non-liquefiable crust layer, the main variable is the drainage speed at the top of the liquefiable level, which is controlled by the hydraulic gradient. The three cases analysed are listed in Table 4.2, note that the hydraulic gradient at the interface is assumed to be less than the critical value.

Figure 4.27 shows the ground response, pile friction, and pile axial load at different degrees of consolidation during reconsolidation. Reconsolidation only happens in the second layer, since it is the only layer that liquefies. The position of the neutral plane barely changes during the process, and the final pile axial force is the same as that in case 1A. Figure 4.28 further indicates that for setup B with a non-liquefiable crust, the settlement of the pile is barely affected by the drainage hydraulic gradient at the top of the liquefied layer. Since the increase of drainage hydraulic gradient only reduces the reconsolidation time, but does not actually alter the process. Unless rate effects of soil are considered, the change in the drainage speed at the top of the liquefiable layer will not affect the final dragload and downdrag settlement of the pile.

Table 4.2 Hydraulic gradient at the top of the liquefiable layer and soil properties in cases for setup B

Cases	i_{top}/i_{cr}	k_{20} (mm/s)	m_{v20} (Pa ⁻¹)
1B	1.0	1.0	1.0×10^{-7}
2B	0.1		
3B	0.01		

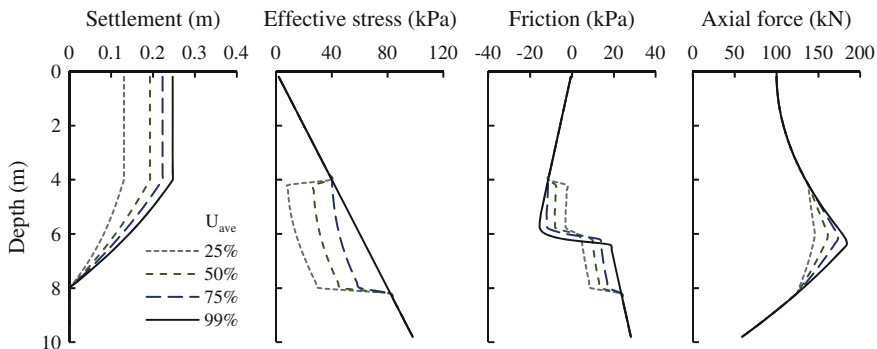


Fig. 4.27 Soil and pile response at various degrees of consolidation in case 1B

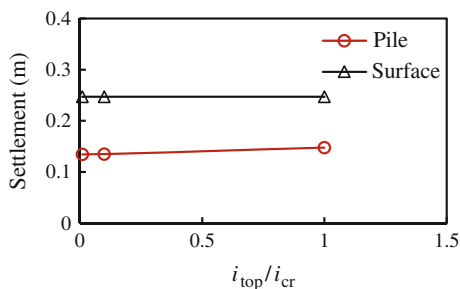


Fig. 4.28 Influence of the hydraulic gradient at the top of the liquefiable layer in setup B on soil surface and pile settlement

4.4 Summary

Pile settlement is typically assumed equal to soil settlement at the depth of the neutral plane, but this is a false inference; rather, the pile velocity is equal to the soil velocity at the neutral plane depth. This fact is supported by fundamental equations from one-dimensional rate independent plasticity theory. Pile displacement must be computed as the integral of soil settlement velocity at the neutral plane depth over time. If the neutral plane depth changes during consolidation or reconsolidation (it typically does because interface friction depends on consolidation and reconsolidation conditions), the traditional neutral plane solution produces an inaccurate estimate of pile settlement. If the neutral plane depth is constant during consolidation and reconsolidation, the traditional neutral plane solution is accurate.

An innovative new beam on nonlinear Winkler foundation approach is presented in which the shaft friction capacity evolves as effective stresses increase during consolidation and post-liquefaction reconsolidation. The new BNWF method clearly demonstrates the fundamental mechanisms involved in time-varying load

transfer between pile and consolidating soil, and shows that settlements from the traditional neutral plane solution are generally inaccurate. A modified neutral plane solution that is amenable to spreadsheet calculation is formulated to account for evolution of the neutral plane depth over time, and provides reasonable agreement with the BNWF solutions.

For the case of liquefaction, a simplified numerical method for calculating the post-liquefaction reconsolidation process of sand is proposed, which takes into consideration the changes of soil permeability and compressibility during reconsolidation.

The methods are validated carefully against two centrifuge tests, one on piles in consolidating clay and another on piles in post-liquefaction reconsolidating sand. The simulation results of both tests are in good agreement with the reported test data. Exhibiting the methods' advantage over the traditional neutral plane solution, especially in calculating the downdrag settlement of piles.

Analyses on piles in post-liquefaction reconsolidating ground using the proposed methods show that the ground setup could significantly influence the settlement and effective stress in the ground, and also the downdrag settlement of piles, especially if the neutral plane position or the ground settlement at the neutral plane is changed through altering the permeability or compressibility of the soil. Although the evolution of the neutral plane depth affects downdrag settlement, it has no influence on the maximum dragload mobilized in the pile, which occurs at the end of primary consolidation.

References

- Boulanger RW, Kutter BL, Brandenberg SJ, Singh P, Chang D. Pile foundations in liquefied and laterally spreading ground during earthquakes: centrifuge experiments and analyses. Report No. UCD/CGM-03/01. California: Center for Geotechnical Modeling, Department of Civil Engineering, University of California, Davis; 2003.
- Fellenius BH. Downdrag on long piles in clay due to negative skin friction. *Can Geotech J.* 1972; 9(4):323–37.
- Holtz RD, Kovacs WD, Sheahan TC. An introduction to geotechnical engineering. 2nd ed. Upper Saddle River, NJ: Prentice Hall; 2011.
- Ladd CC. Stability evaluation during staged construction. *J Geotech Geoenviron Eng.* 1991;117 (4):540–615.
- Lam SY, Ng CWW, Leung CF, Chan SH. Centrifuge and numerical modeling of axial load effects on piles in consolidating ground. *Can Geotech J.* 2009;46:10–24.
- Mayerhof GG. Bearing capacity and settlement of pile foundations. *J Geotech Geoenviron Eng.* 1976;102(3):197–228.
- McKenna F, Fenves GL. OpenSees manual. PEER Center; 2001. <http://OpenSees.berkeley.edu>
- Mosher RL. Load transfer criteria for numerical analysis of axial loaded piles in sand. Mississippi: US Army engineering waterways experimental station, Automatic data processing center, 1984.
- Ministry of Housing and Urban-Rural Development of China. JGJ94-2008 Technical code for building pile foundations. Beijing: 2008. (In Chinese).

- Reese LC, O'Neill MW. Drilled shafts: construction procedures and design methods. Report No. FHWA-HI-88-042. Virginia: U.S. Department of Transportation, Federal Highway Administration, Office of Implementation; 1988.
- Salgado R. The engineering of foundations. New York: McGraw Hill; 2008.
- Seed HB, Philippe PM, Lysmer J. The generation and dissipation of pore water pressures during soil liquefaction. Report: EERC-75-26; 1975.
- Shahir H, Pak A, Taiebat M, Jeremic B. Evaluation of variation of permeability in liquefiable soil under earthquake loading. *Comput Geotech*. 2012;40:74–88.
- Simo JC, Hughes TJR. *Computational Inelasticity*. Berlin Heidelberg: Springer; 1998.
- Stringer ME, Madabhushi S. Re-mobilization of pile shaft friction after an earthquake. *Can Geotech J*. 2013;50(9):979–88.
- Vijayvergiya VN. Load-movement characteristics of piles. In: *Proceedings, Ports 77 Conference*. California: American Society of Civil Engineers; 1977.

Chapter 5

Conclusions and Future Work

5.1 Conclusions

The analysis of the seismic response of piles in liquefiable ground is an important yet challenging topic in the field of geotechnical earthquake engineering. This dissertation tries to make an effort to improve the understanding of seismic pile behaviour in liquefiable ground by developing high fidelity numerical methods and analysing some of the aspects of the lateral and vertical pile response.

A three dimensional unified plasticity model for large post-liquefaction shear deformation of sand is formulated based on the mechanism of post-liquefaction deformation and the bounding surface plasticity framework. The model is unique in that it provides a unified description of sand of different conditions from pre- to post-liquefaction under monotonic and cyclic loading. The model is implemented in the OpenSees finite element platform using the cutting plane algorithm for stress integration, and applied various techniques to improve its numerical stability and performance, and is made openly accessible to the technical community. The model is validated against drained/undrained triaxial and torsional laboratory experiments, and also centrifuge shaking table experiments.

Applying the constitutive model, a continuum 3D finite element method for simulation of piles in liquefiable ground is proposed. Special attention is dedicated towards the modelling of piles and soil-pile interface to accurately reflect the behaviour of piles. A staged modelling procedure is adopted to appropriately generate the initial stress field in the soil and piles and achieve hydrostatic pore pressure prior to seismic loading. Three centrifuge shaking table tests on single piles both with and without pile cap and superstructure in level and inclined liquefiable ground are conducted and simulated in validation of the proposed method, showing excellent agreement between the numerical simulation results and test results, and providing confidence in the numerical analysis of the seismic response of piles in liquefiable ground.

Using the 3D finite element simulation method, some major factors influencing the seismic response of single piles in liquefiable ground is investigated. The existence of the pile cap is found to restrain the rotation of the pile head, changing the bending mode of the pile. Inclined ground causes significant pile residual moment through lateral spreading, and even a modestly inclined ground is sufficient to generate a residual moment that controls the pile moment demand due to the dilatancy of the sand. The existence of a non-liquefiable crust restricts the pile rotation within the layer, causing the bending and pile moment to intensify at the interface between non-liquefiable and liquefiable layers.

The roles that lateral inertial and kinematic interactions play on the pile moment is found to differ in different soil-pile-structure systems. Inertial structure force and kinematic soil displacement of the same direction could cause pile head moments of the same or opposite directions depending on the rotational constraint at the pile head. Kinematic interaction has a dominating influence on the pile moment for pile foundations with pile head rotation constrained by the existence of a pile cap, while inertial interaction is strongly influential for free-head piles. The coupling of inertial and kinematic interactions depends on the soil-pile-structure system setup and the magnitudes of the inertial structure force and the kinematic soil displacement. Many current pseudo-static methods for calculating the seismic pile demand through summing a percentage of the kinematic demand with another percentage of the inertial demand could produce very inaccurate results under certain conditions.

For the post-earthquake vertical demand of single piles in liquefiable ground, the downdrag problem is studied. The fundamental error in the traditional neutral plane solution for calculating the downdrag settlement of piles promoted the development of a BNWF method and a modified NPS for piles in consolidating and reconsolidating ground, which would typically experience changes in the neutral plane position. The proposed methods are evaluated through detailed simulation of two centrifuge tests, one on a single pile in consolidating clay, and the other on piles in post-liquefaction reconsolidating sand. Analyses on piles in post-liquefaction reconsolidating ground using the proposed methods show that the ground setup could significantly influence the downdrag settlement of piles. Although the evolution of the neutral plane depth affects downdrag settlement, it has no influence on the maximum dragload mobilized in the pile, which occurs at the end of primary consolidation.

5.2 Future Work

Although several analysis methods are developed, and extensive analysis on the seismic response of single piles in liquefiable ground are carried out in this study, this dissertation has only taken a small step in improving the understanding of the dynamic pile behaviours, and much future work is still to be done.

The work in this dissertation only focused on the behaviour of single piles, however, pile groups are much more widely used in practice, while piled-rafts are

also widely used for high-rise structures. The factors of influence, inertial and kinematic interaction coupling, and the distribution of load and group effects in pile groups and piled-raft foundations during seismic liquefaction events require further investigation. For pile groups and piled raft foundations, the arrangement of piles, the stiffness of the pile cap and raft could all have significant influence on the seismic pile demand.

In the current study, the lateral and vertical responses are studied separately due to the deficiency of the constitutive model in simulating liquefaction induced settlement. It would be highly ideal if the numerical simulation method could be further developed to allow for the lateral and vertical analyses to be conducted together, which would require further understanding of the constitutive behaviour of saturated sand.

During earthquakes, the seismic motion is never only horizontal. The vertical motion could also have a strong impact on the response of the piles, especially in terms of axial load and settlement. Model tests and numerical simulations should be conducted to look into the behaviour of piles in liquefiable ground under a combination of horizontal and vertical motions.